FIELD EMITTERS AND SUPERCAPACITORS BASED ON CARBON NANOTUBE FILMS

By

Siyu Wei

Dissertation

Submitted to the Faculty of the

Graduate School of Vanderbilt University

in partial fulfillment of the requirements

for the degree of

DOCTOR OF PHILOSOPHY

in

Interdisciplinary Materials Science

December, 2009

Nashville, Tennessee

Approved:

Weng Poo Kang

Jim Davidson

Deyu Li

Alvin Strauss

Norman Tolk

To my wife Lixiang, my parents Mrs. Hua Cong and Mr. Yaguang Wei.

ACKNOWLEDGEMENTS

There are no best words I can come up with to express my sincere gratitude to my advisor and mentor, Prof. Weng-Poo Kang who has been guiding and supporting me both academically and spiritually throughout all these years of my stay at Vanderbilt. I can not imagine if any success in my scholastic life would be made possible without his continuous encouragement and help. I have the same feelings for Prof. Jimmy Davidson, whose leadership and charisma inspired me far beyond my academic life. Thanks to the family atmosphere created by him, not only I always felt like home here at the Diamond Group, but I also learned how to become a team player, an essential trait I will benefit from for the rest of my life.

I can not say enough Thank You to Profs. Deyu Li, Alvin Strauss, and Norman Tolk, for taking their precious time to serve on my committee, and their constructive suggestions to my dissertation. I'd also like to thank Prof. Bridget Rogers of Chemical Engineering at Vanderbilt for her help in collecting and interpreting XPS data of my research findings.

A special thanks goes to Dr. Kelvin Wong and Mr. Mick Howell, who have helped me with everything in the lab from day one.

Finally, my appreciation goes to my colleagues Dr. Bo Choi, Nikkon Ghosh, Puteri Hamari, Celestina LeQuan, Supil Raina, and Kaleng Soh for the best years of our lives spent together as a family. I love you all forever.

TABLE OF CONTENTS

DEDICATIONS………………………………..…………………………………...ii

ACKNOWLEDGEMENTS……………………………………..………..……....iii

TABLE OF CONTENTS……………………………………………………... .iv

LIST OF TABLES………………………………………………………………....vi

LIST OF FIGURES………………………………………………………....….vii

CHAPTER I: INTRODUCTION………………………………...……..…..…..1

STRUCTURE AND SYNTHESIS OF CARBON NANOTUBES……………………1
PROPERTIES OF CARBON NANOTUBES……………………………..……..…4
MOTIVATIONS…………………………………………………………..……..…7
OBJECTIVES……………………………………………………………..………..8
ORGANIZATION OF DISSERTATION……………………………………………9

CHAPTER II: LITERATURE REVIEW……………………………………………11

VACUUM FIELD EMISSION……………………………………………………....11
SUPERCAPACITORS………………………………………………………….....14
CNT SYNTHESIS BY CVD AND PECVD…………………………………………21

CHAPTER III: PROPOSED RESEARCH AND APPROACHES..………………...24

CNT FIELD EMITTERS BY THERMAL CVD WITH PALLADIUM AS CATALYST……………………………………………………………24
CNT FIELD EMITTERS BY THERMAL CVD WITH NICKEL AS CATALYST…………..27
CNT FIELD EMITTERS BY THERMAL CVD WITH COBALT AS CATALYST…………………………………………………………...…...29
CNT-BASED SUPERCAPACITORS FABRICATED BY MPECVD………………31
SUPERCAPACITOR ELECTRODES BASED ON CNT THIN FILM AND MANGANESE DIOXIDE……………………………………………………....33
PREPARATION OF MANGANESE DIOXIDE…………………………………….34

CHAPTER IV: RESULTS AND DISCUSSION…………………………………..…36

CNT FIELD EMITTERS BY THERMAL CVD WITH PALLADIUM AS CATALYST…………………………………………………………………..36

CNT FIELD EMITTERS BY THERMAL CVD AT ATMOSPHERIC PRESSURE WITH NICKEL AS CATALYST……………………………………………………47
CNT FIELD EMITTERS BY THERMAL CVD AT ATMOSPHERIC PRESSURE WITH COBALT AS CATALYST……………………………………………….…..56
SUMMARY OF CATALYTIC PERFORMANCE OF PALLADIUM, NICKEL AND COBALT FOR THERMAL CVDS…………………………………………………67
CNT-BASED SUPERCAPACITORS FABRICATED BY MPECVD………………69
SUPERCAPACITOR ELECTRODES BASED ON MANGANESE DIOXIDE COATED CNT THIN FILM ..……………………………………………………80

CHAPTER V: CONCLUSIONS……………………………………………………93

CHAPTER VI: FUTURE WORK...…………………………………………………96

PUBLICATIONS……………………………………………………………………..98

REFERENCES…………………………………………………………………100

LIST OF TABLES

Table 3.1. Test procedures for Pd particle size distribution and CNT growth…………..26
Table 3.2. Test procedures of Ni particle and CNT growth experiments………………..29
Table 3.3. Experimental procedures for Co particle treatment and CNT growth………..31
Table 4.1. Pd particle size distribution………………………………………………..40
Table 4.2. Experimental results of the effects of Pd catalyst thickness and NH_3 pretreatment time on the density and diameter of as grown CNTs and turn-on field and field enhancement factor (β) of the CNT cathodes………………………………………46
Table 4.3. Ni particle density and size distribution corresponding to Ni film thickness and ammonia flow rate……………………………………………………………………52
Table 4.4. Summary of CNTs critical processes and field emission parameters………...54
Table 4.5. Summary of CNTs process parameters and field emission characteristics…..66
Table 4.6. Catalyst particle size and density of 3, 4, and 5 nm Ni films after 1 min pretreatment…………………………………………………………………………...75
Table 4.7. Diameter, density, height, and total surface area of CNT arrays……………..76
Table 4.8. XPS binding energies of manganese oxides at room temperature [143]……..92

LIST OF FIGURES

Fig. 1.1. A symbolic schematic showing a SWCNT is formed by rolling up a graphene sheet……………………………………………………………………………………1
Fig. 1.2. Schematic of (a) arc discharge, (b) laser ablation, and (c) chemical vapor deposition of carbon nanotubes…………………………………………………………...5
Fig. 1.3. (a) OA = na1+ma2 is a chiral vector defined by unit vectors a1 and a2 and a pair of integers (n, m). θ is the angle between the zigzag axis and the chiral vector. For the chiral vector shown in the graph, (n, m) = (4, 2). (b) Possible combinations of integer pairs (n, m) for CNTs, including zigzag (along zigzag axis), arm chair (along armchair axis) and chiral (between the two axes). The solid dots denote metallic CNTs and the encircled dots correspond to semiconducting nanotubes. (c) Models of SWCNTs. From top to bottom: armchair, zigzag, and chiral nanotubes……………………………………6
Fig. 1.4. Ragone plot showing energy density vs. power density for various energy-storage devices (Source: wikipedia.org)………………………………………………..7
Fig. 2.1. A typical I-E curve and Fowler-Nordheim (F-N) plot for a field emission cathode (S. Wei et al, unpublished data)… ……………………………………………...13
Fig. 2.2. Schematic of a supercapacitor and the potential drop at the electrode-electrolyte interfaces…………………………………………………………………………………16
Fig. 2.3. Operation mechanism of an electrochemical supercapacitor…………………..18
Fig. 2.4. Temperature dependence of specific capacitance for activated carbon electrode in trigeminal tricationic quat electrolyte………………………………………………18
Fig. 2.5. Electrochemically prepared PPy/CNT composite [95]………………………...20
Fig. 3.1. Thermal CVD system setup……………………………………………………25
Fig. 3.2. Schematic of field emission test on CNT diode structure……………………...26
Fig. 3.3. Schematic of MWPECVD system……………………………………………...33
Fig. 4.1. Samples 1a through 1c are treated in pure Ar while samples 2a through 2c processed in Ar/H_2 (4:1), the SEM images strongly indicate the optimizing effect of H_2 on the shape and uniformity of Pd particles. Samples 3a through 3c and 4a through 4c are pretreated in NH_3 for 1 minute and 10 minutes, respectively, the SEM images demonstrate that NH_3 increases the density of Pd particles while decreasing their average size. Letters a, b, and c denote the initial Pd film thickness as 10nm, 20nm, and 30nm, respectively…………………………………………………………………………39
Fig. 4.2. Samples 5a-5c and 6a-6c are not exposed to NH_3 and have very few CNTs grown, higher CH_4 to Ar/H_2 ratio for 6a-6c does not help produce more CNTs, as compared to 5a-5c. Introducing NH_3 during CNT growth significantly increases the density of CNTs (7a-7c). NH_3 treatment prior to growth further increases CNT density (1 minute and 10 minutes pretreatment for 8a-8c and 9a-9c, respectively)………………...41
Fig. 4.3. Low (a) and high (b) magnification TEM images of Pd-catalyzed CNT. Some catalyst particles are trapped in the CNT body. The multi-walled structure can not be seen due to the amorphous carbon coating on the CNT surface………………………………42
Fig. 4.4. Raman spectra of as-grown CNTs on samples 9a-9c, note the different initial Pd film thicknesses. I/(D)/I(G) varies between 1.25 and 1.48. Possible peaks at Raman shift

below 50cm^{-1} are not recorded. Peaks at ~1330 and ~1590cm^{-1} are attributed to D-line and G-line, respectively. No apparent second-order peaks are observed………………..43
Fig. 4.5. I-E characteristics of as-grown CNTs: Letters a, b, and c denote the Pd film thickness of 10, 20, and 30nm, respectively. 7a-c for samples processed without NH_3 pretreatment but with NH_3 incorporation during synthesis. 8a-c for samples processed with 1 min NH_3 pretreatment and with NH_3 incorporation during synthesis. 9a-c for samples processed with 10 min NH_3 pretreatment and with NH_3 incorporation during synthesis……………………………………………………………………………45
Fig. 4.6. Corresponding F-N plots of Fig. 4.5…………………………………………...46
Fig. 4.7. Effects of initial catalyst film thickness and ammonia flow rate on the Ni particle size and density distribution. Four sets (1-4)of samples have undergone the tests. a, b, and c in each set denotes the Ni film thickness of 6, 9, and 11 nm, respectively. Samples 1a-1c were annealed in Ar/H_2 (4:1, 75sccm) for 30min, 2a-2c were annealed in Ar/H_2 (4:1, 75sccm) + NH_3 / N_2 (1:4, 24sccm) for 30min. 3a-3c and 4a-4c were tested under similar conditions as of 2a-2c, except that the NH_3 / N_2 flow rates were 32 and 43, respectively……………………………………………………………………………51
Fig 4.8. Effects of catalyst film thickness and ammonia flow rate on the density, size, and morphology of as-grown CNTs. Samples 5a-5c were not exposed to ammonia and no significant CNT growth was observed because of the catalyst particle passivation caused by amorphous carbon coating. Ni particles size on samples 5a-8a was less than 20nm in diameter, which were easily poisoned and contaminated by impurities, as a result, CNT growth was not noticeable. Samples 6b, 6c, 7b, and 7c were tested under the critical ammonia to hydrocarbon flow rate ratio, therefore the as–grown CNTs were randomly oriented. At above the threshold NH_3/C_2H_2 ratio, arrays of vertically aligned CNTs were produced (samples 8b and 8c)…………………………………………………………53
Fig. 4.9. High magnification SEM pictures of as-grown CNTs on samples 8b and 8c indicates the different degree of alignment between the two. Higher density of CNTs leads to a better alignment (8b) as the strong van der Waals interactions allow only one degree of freedom for CNT growth……………………………………………………...54
Fig. 4.10. Both randomly oriented and vertically aligned CNTs have virtually the same Raman spectra. The strong signal at about 1590 cm^{-1} is attributed to the G-band of tangential mode of the graphitic structure while the peak around 1330 cm^{-1} is the D-band corresponding to the defects or limited dimensions of CNT crystal structure. The D-band signal intensity is stronger than that of the G-band indicating the CNTs synthesized by CVD at atmospheric pressure have some considerable lattice defects…………………..55
Fig. 4.11. Fabrication and field emission test of CNT cathodes. Ti was sputtered using a shadow mask as the cathode extension……………………………………………………..55
Fig. 4.12. I-E characteristics of as-grown CNT cathodes. Vertically aligned CNTs (8b and 8c) have lower turn-on fields (3.2 and 3.5 V/um, respectively) than the randomly oriented CNTs (5-7 V/um)……………………………………………………………………...56
Fig. 4.13. Effects of initial catalyst film thickness and ammonia flow rate on the Co particle size and density distribution. Three sets (1-3) of samples have undergone the tests. The label a, b, and c in each set denotes the Co film thickness of 19, 28, and 31 nm, respectively. Samples 1a-1c were annealed in Ar/H_2 (4:1, 75sccm) for 30min, 2a-2c were annealed in Ar/H_2 (4:1, 75sccm) + NH_3 / N_2 (1:4, 16sccm) for 30min. 3a-3c were tested under similar conditions as of 2a-2c, except that the NH_3/N_2 flow rate was 24 sccm…..61

Fig. 4.14. Effects of catalyst film thickness and ammonia flow rate on the density, size, and morphology of as-grown CNTs. Samples 4a-4c were not exposed to ammonia and no CNT growth was observed. Samples 5a-5c and 6a-6c were processed with ammonia and the growth of CNTs was successful on these samples. The density of as-grown nanotubes increases with ammonia flow rate……………………………………………………62
Fig. 4.15. High magnification SEM pictures of vertically aligned CNTs on samples 5c, 6a-6c indicating the different degree of tube alignment. Higher density of CNTs leads to a better alignment as the strong van der Waals interactions allow only one degree of freedom for CNT growth……………………………………………………………..63
Fig. 4.16. TEM images confirm the tubular (left) multi-walled (right) structure of as-grown CNTs………………………………………………………………………..63
Fig. 4.17. Typical Raman spectra of the as grown CNTs. Both randomly oriented and vertically aligned CNTs have virtually the same Raman spectra. The strong signal at about 1590 cm^{-1} is attributed to the G-band of tangential mode of the graphitic structure while the peak around 1330 cm^{-1} is the D-band corresponding to the defects or limited dimensions of CNT crystal structure. The D-band signal intensity is stronger than that of the G-band indicating the CNTs synthesized by CVD at atmospheric pressure have some considerable lattice defects. A weak second order peak corresponding to 2D is observed at 2660 cm^{-1}…………………………………………………………………………...64
Fig. 4.18. Schematics of CNTs cathode fabrication and field emission test. Ti was sputtered using a shadow mask as the cathode extension prior to Co deposition………..65
Fig. 4.19. Field Emission (I-E) characteristics of as-grown CNT cathodes. Vertically aligned CNTs (6b and 6c) show low turn-on fields (about 1.2-1.8V/um) and high current yield……………………………………………………………………………………66
Fig. 4.20. Base and tip growth modes of CNTs [131]…………………………………...69
Fig. 4.21. SEM images of Ni particle size and density. Three-, four-, and five-nanometer nickel films separate into well defined discrete catalyst particles by hydrogen plasma, while two-nanometer catalyst film appears to have a carpet-like, semi-continuous morphology.………………………………………………………………………………...74
Fig. 4.22. SEM summary of CNT growth. Rows 1 through 4 from top to bottom correspond to the nickel catalyst film thickness of 2, 3, 4, and 5 nm, respectively, while columns one to four from left to right correspond to hydrogen plasma pretreatment time of 1, 3, 5, and 7 minutes……………………………………………………………………75
Fig. 4.23. The average number of nanotubes in 1um span is estimated at 24-25 for sample 4nm_3min……………………………………………………………………………......76
Fig. 4.24. The hollow tube structure of as-grown CNTs is readily seen even in low magnification TEM image (a). Some catalyst particles are trapped at the ends of nanotubes, suggesting tip growth mode. The nanotube shown in high magnification TEM picture (b) has about 10 walls and the inter-wall spacing is ~ 0.34 nm…………………77
Fig. 4.25. Raman spectrum of as-grown CNT thin films. The strongest peak at 1327 cm^{-1} is obviously assigned to the D-band indicating the presence of disorder or defects in the nanotube structures. The second strongest band at 1587 cm^{-1} corresponds to G-band graphite mode. The other bands located at 2654 and 2915 cm^{-1} are due to the second-order combinations of 2D and D + G, respectively……………………………………...77
Fig. 4.26. (A) Cyclic voltammograms of as-grown CNT electrodes for four sets of hydrogen plasma pretreatment times on various catalyst thicknesses prior to CNT

synthesis. For the same pretreatment time, 3 nm samples consistently demonstrate the highest capacitance and 5 nm samples the lowest. Capacitance value is higher on sample with higher surface area of CNTs, and the estimated surface area per square micron substrate is marked to each corresponding curve. (B) Same data with current converted to capacitance per unit area (mF/cm^2)……………..………………………………………78
Fig. 4.27. Capacitance-voltammograms of as-grown CNT electrodes for 3 sets of catalyst thicknesses subjected to different pretreatment times. The three minute pretreatment samples have the highest capacitance for all the catalyst thicknesses investigated……79
Fig. 4.28. Cyclic voltammograms of CNT electrode based on 3 nm Ni film with three minutes of pretreatment. Nearly rectangular shaped I-V curve is maintained while the scan rate is varied from 10 to 1000mV/s………………………………………………...80
Fig. 4.29. SEM pictures of (A) as grown CNT thin film, (B) 5, (C) 15, and (D) 30 droplets of MnO_2 suspension on CNT film after drying at room temperature……………………………….…………………………………………...87
Fig. 4.30. Low (A) and high magnification (B) TEM images showing MnO_2 particles attached to CNTs...87
Fig. 4.31. Cyclic voltammograms of MnO_2/CNT composite samples compared with as-grown CNT film at 100mV/s (A); corresponding specific capacitance curves (B); voltammograms of 30-droplet sample at different scan rates (C)……………………………………………….…………………………………88
Fig. 4.32. Cyclic voltammograms of CNT-free MnO_2 samples compared with as-grown CNT. Scan rate is 100mV/s………………………………………………………...89
Fig. 4.33. Schematic of supercapacitor based on CNT/MnO2 composite electrode……90
Fig. 4.34. Galvano-static charging and discharging behavior of (A) as-grown CNT film at 30uA, (B) 5-droplet sample at 30uA, (C) 15-droplet sample at 30uA, (D) 15-droplet sample at 120uA, (E) 30-droplet sample at 120uA, and (F) 30-droplet sample at 1920uA, respectively...91
Fig. 4.35. XPS surveys of (A) as-grown CNT thin film, and (B) 5-droplet sample; (C) shows the details of Mn2p peaks corresponding to (B); (D) is the survey of the 5-droplet sample after 100 cyclic voltammetry scans at 100mV/s in 0.1M/L KCl aqueous solution..92

CHAPTER I

INTRODUCTION

This chapter provides background information about structure, synthesis, and properties of carbon nanotubes (CNTs), their potential applications in vacuum field emission (VFE) and energy storage, which are the major subjects of this study. Secondly, the objectives of this work will be set. Lastly, the organization of the dissertation will be outlined.

Structure and Synthesis of Carbon Nanotubes

Carbon nanotubes (CNTs) have been researched extensively world-wide since their discovery in 1991 [1]. The first reported CNTs were multi-walled CNTs (MWCNTs), while synthesis of single-walled CNTs (SWCNTs) was reported two years later [2, 3]. Fig. 1.1 shows that a SWCNT can be formed by rolling up a graphene sheet [4]. Like-wise, a MWCNT can be symbolically considered to be assembled with a number of coaxial SWCNTs of different diameters, although these are not the real ways CNTs are synthesized.

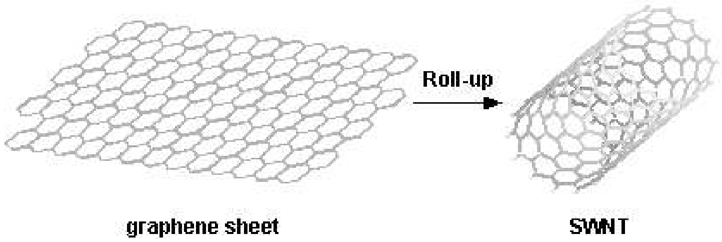

Fig. 1.1. A symbolic schematic showing a SWCNT is formed by rolling up a graphene sheet.

Similar to graphite, bonding in CNTs is sp^2, although the curved atomic plane in CNT structure causes the quantum confinement and subsequently, the σ-π rehybridization. As a result, three σ bonds are slightly out of plane, and π orbital is more delocalized than that in graphite [5]. Therefore, CNTs are mechanically stronger, chemically and biologically more active, and have higher electrical and thermal conductivities than graphite. Unlike graphite, CNTs may have pentagons and heptagons in their structure.

CNTs are mostly synthesized by arc discharge, laser ablation and chemical vapor deposition (CVD), including plasma enhanced CVD (PECVD). Arc discharge and laser ablation are sometimes referred to as high temperature methods of CNT synthesis [6] because the reaction temperatures are usually close to the melting point of graphite. With arc discharge generated by helium plasma between two graphite electrodes with opposite polarities (Fig.1. 2 (a)), the anode is gradually evaporated and CNTs are deposited on the cathode. Arc discharge is a good method for producing both SWCNTs and MWCNTs. While the CNTs discovered by Iijima were produced with this method, Ebbesen and Ajayan [7] were the first to achieve the yield of high quality MWCNTs in grams. To grow SWCNTs with arc discharge, a catalyst is needed. The catalyst is usually a transition metal in the form of powder. A mixture of catalyst and graphite powder is filled into a hollow graphite anode so both elements will be evaporated during the arc discharge process. By adjusting the processing parameters, SWCNTs can be produced. The first success of obtaining SWCNTs at gram level was reported in 1996 by R. Smalley et al [8] using laser ablation method (Fig. 1.2 (b)). The process utilized laser pulses to evaporate a graphite rod containing nickel and cobalt as catalysts. A flow of inert gas was maintained during the entire process to avoid oxidation and carry the grown CNTs downstream so they could be collected on a cold finger. The as-grown SWNTs were rather uniform in diameter and self-assembled by van der Waals interactions into rope-like bundles of tens to hundreds um long. Synthesis of MWCNTs by laser ablation was achieved in 1995 [9].

While arc discharge and laser ablation are very useful techniques to produce CNTs, their application in selective growth on patterned substrates is limited due to the equipment configurations and high reaction temperatures. This need is fulfilled by chemical vapor deposition (CVD). In literature, the term CVD without any prefix usually refers to thermal CVD. In thermal CVD, a conventional heat source such as a furnace, infrared lamp, inductive or resistive heater is used. Fig. 1.2 (c) shows a typical setup for thermal CVD. Usually a catalyst material is heated to 500~1000°C in an inert or reductive gas flow through a tube reactor followed by the introduction of a hydrocarbon gas for a period of time. CNTs grown on the catalyst surface of the patterned substrate are collected after the system is cooled to room temperature. Thermal CVD syntheses of MWCNTs [10-15] and SWCNTs [16-20] were first reported in the mid- and late 1990s, respectively, and the literature on this subject has expanded tremendously.

If plasma is used as heat source, the process is referred to as plasma enhanced CVD (PECVD). There are many variations of PECVD processes, including DC plasma [21-31], microwave plasma [32-40], plasma assisted hot filament [41-46], radio frequency capacitive and inductive [47-52], and electron cyclotron resonance CVD [53-62], etc. In this work, furnace thermal CVD and microwave PECVD are the synthesis methods utilized to grow MWCNTs. These two processes will be further elaborated in the succeeding chapters.

Properties of Carbon Nanotubes

Diameter of MWCNTs can be as small as a few nanometers, while the smallest SWCNTs have the diameter slightly over 1nm. In addition, structure of CNTs is highly symmetric. Such geometrical characteristics attribute to some extraordinary electronic, magnetic, and lattice properties of CNTs.

Fig. 1.3 [63] depicts the formation of three kinds of SWCNTs, namely, armchair, zigzag, and chiral, depending on the directions they are rolled up in. Armchair and zigzag SWCNTs have mirror symmetry of atomic structure therefore are ‘achiral’ nanotubes. According to Fig. 1.3 (b), one third of SWCNTs are metallic and the rest are semiconducting. The band gap of a semiconducting CNT can be estimated by $E_g = 2d_{cc}\gamma/D$ [5], where $d_{cc} = 0.142$ nm is the carbon-carbon bond length, D is the tube diameter, $\gamma = 2.5 \sim 3.2$ eV according to various sources [64-72]. For a semiconducting SWCNT with diameter of 1nm, the band gap is estimated at 0.7~0.9 eV. Intertube coupling must be considered for SWCNT bundles and MWCNTs. The intertube coupling creates a small band gap for certain metallic SWCNTs [73] while reduces it for semiconducting SWCNTs [74] in a SWCNT bundle. All semiconducting tubes in a MWCNT tend to be semi-metallic because the band gap is reduced by their large diameters in addition to the electron-hole pairing for multi-wall coupling.

CNTs have the highest Young’s modulus and tensile strength among all materials known. Young’s modulus and tensile strength of MWCNTs are approximately 6 and 300 times that of steel, respectively. Such extraordinary mechanical properties of CNTs are attributed to the predominant σ bonding in nanotubes. The extremely small size of CNTs leads to very high surface area to volume ratio of CNT films and these films are very promising for energy storage, particularly electrochemical capacitors (supercapacitors). The nanometer size radius of curvature and high aspect ratio, unique one-dimensional electron tunneling properties along with strong chemical and thermal stability make CNTs ideal cathode material for vacuum electron field emission.

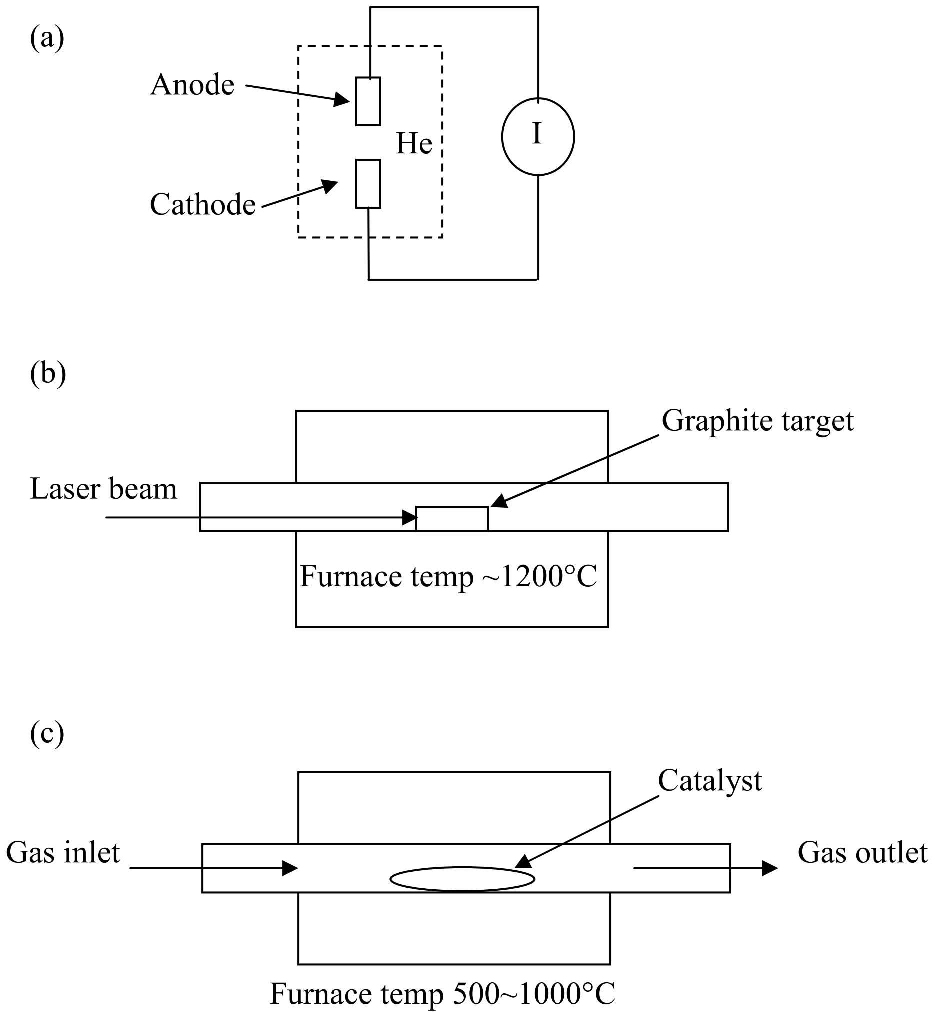

Fig. 1.2. Schematic of (a) arc discharge, (b) laser ablation, and (c) chemical vapor deposition of carbon nanotubes.

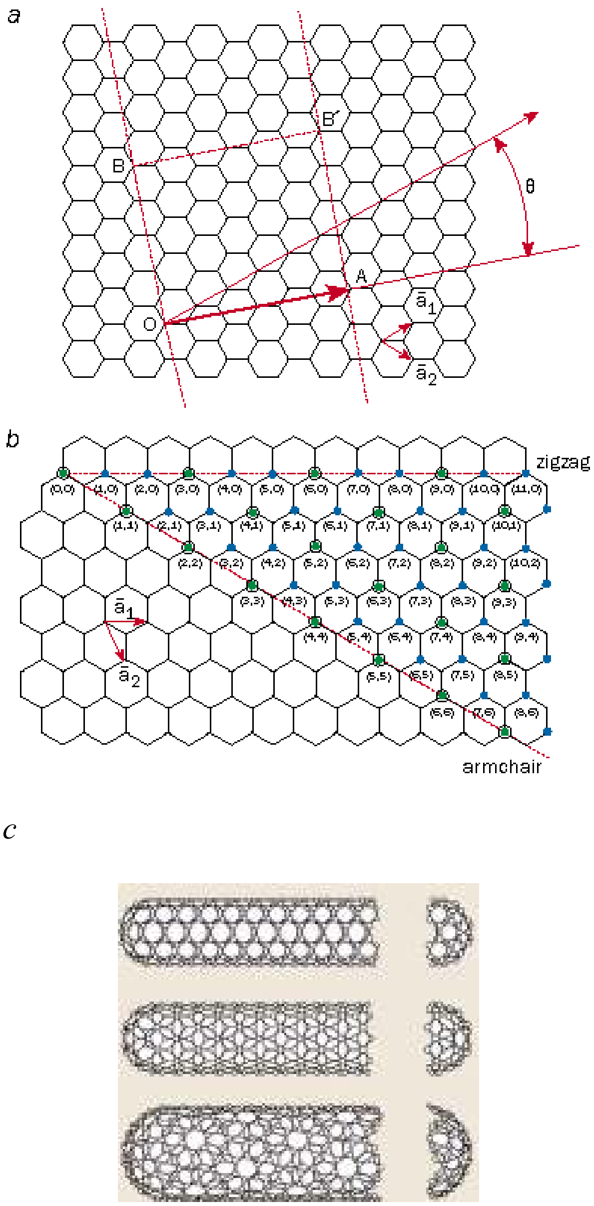

Fig. 1.3. (a) OA = na1+ma2 is a chiral vector defined by unit vectors a1 and a2 and a pair of integers (n, m). θ is the angle between the zigzag axis and the chiral vector. For the chiral vector shown in the graph, (n, m) = (4, 2). (b) Possible combinations of integer pairs (n, m) for CNTs, including zigzag (along zigzag axis), arm chair (along armchair axis) and chiral (between the two axes). The solid dots denote metallic CNTs and the encircled dots correspond to semiconducting nanotubes. (c) Models of SWCNTs. From top to bottom: armchair, zigzag, and chiral nanotubes.

Motivations

This study is motivated by two potential applications of CNTs: vacuum field emission and supercapacitance.

Field emission devices have certain advantages over their solid state counterparts. Electrons travel at the speed of light in vacuum, which is ~3000 times faster than that in silicon. The energy dissipation is also much less in vacuum than in any semiconductor. Therefore, vacuum devices can operate at higher frequencies and higher power. In addition, they are more temperature and radiation tolerant. There are many potential applications of field emission, including flat panel displays, microwave amplifiers, sensors, actuators, electron microscopes, mass spectrometers, X-ray generators, high energy accelerators, and electron beam lithography [75].

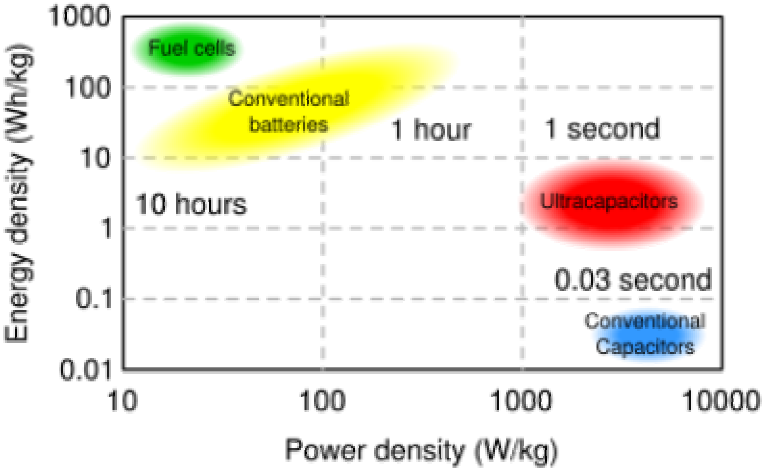

Fig. 1.4. Ragone plot showing energy density vs. power density for various energy-storage devices (Source: wikipedia.org).

Supercapacitors or ultracapacitors have much higher energy density than conventional capacitors and their power density is far superior to that of batteries including fuel cells (Fig. 1.4). They are of particular interest in automotive applications for hybrid vehicles and as supplementary storage for battery electric vehicles.

The extremely small radius of nanotube tip and high aspect ratio, along with high mechanical strength and superior thermal conductivity, make CNTs very attractive electron field emitters. The relatively high work function of ~5 eV can be overcome by the large field enhancement factors of CNTs. Therefore, electrons can be released from CNTs at low macroscopic electric field. CNT field emitters can be synthesized on patterned substrates with CVD process. Unlike silicon and metallic microtips, CNT emitters do not require costly and time-consuming microfabrication/micromaching processes and have much higher field enhancement factors.

CNTs are excellent electrode material for energy storage devices especially supercapacitors because they have very large surface area to volume ratio. In addition, they are well polarizable, chemically stable in different solutions (acids, alkalines, and salts), thermally stable, and environmentally friendly. Also, CNT electrodes can be fabricated at lower cost than other materials.

Objectives

This study is focused on CNT synthesis by thermal CVD and MPECVD, fabrication and characterization of CNT vacuum field emitters and CNT supercapacitor electrodes. The major goals include, for the first time, systematic studies of Pd as a new catalyst for CNT growth; synthesis of vertically aligned CNT arrays at atmospheric pressure; and development of a novel technique to fabricate CNT/transition metal oxide composite for supercapacitor applications. This work encompasses the following tasks:

(i) CVD synthesis of CNTs at atmospheric pressure with Pd as catalyst.

(ii) CVD synthesis of vertically aligned CNT arrays at atmospheric pressure with Co and Ni as catalysts.

(iii) Characterization of CNT field emitters fabricated with CVD using Pd, Ni, and Co as catalysts. Investigation of the effect of proceess parameters on properties of CNT field emitters.

(iv) MPECVD synthesis of thin film electrodes based on well aligned CNT arrays for supercapacitor applications.

(v) Investigation of the correlation synthesis parameters and supercapacitor behavior of as-grown CNT electrodes.

(vi) Investigation of the effect of transition metal oxide incorporation on capacitor properties of CNT electrodes.

Organization of Dissertation

This paper contains six chapters.

Chapter I introduces background information about structure, synthesis, and properties of carbon nanotubes (CNTs), their potential applications in vacuum field emission (VFE) and energy storage. The motivations and objectives of this work are also outlined.

Chapter II reviews the principles of vacuum field emission and energy storage, discusses the properties of CNTs, and explores the advantages of CNT-based field emitters and supercapacitor electrodes.

Chapter III outlines the experimental procedure in details.

Chapter IV presents and discusses experimental results.

Chapter V summarizes the main findings.

Chapter VI proposes the future work.

CHAPTER II

LITERATURE REVIEW

In this chapter, theoretical fundamentals of vacuum field emission and supercapacitance are presented. Following that, growth mechanisms of CNTs by CVD and MPECVD are discussed.

Vacuum Field Emission

Field emission is a phenomenon that electrons pass through a potential barrier from a solid surface into vacuum under a high applied electric field. It is a quantum tunneling process.

Field emission was first reported by R. W. Wood in 1897 during his experimental study on discharge tube. In 1922, Lilienfeld observed this effect in a X-ray tube with pointed cathode under high vacuum. Classical physics failed to explain the phenomenon that field emission was independent of temperature in the range well below onset of thermionic emission. It was Fowler and Nordheim who laid the foundation of field emission theory in 1928 using wave-mechanical formulation [76]. They derived the field emission equation to estimate the emission current density in regards to applied electric field, which is often referred to as Fowler-Nordheim equation:

$$j = 6.2\times10^{6}\frac{\left(\mu/\phi\right)^{\frac{1}{2}}}{\mu+\phi}\bullet F^{2}\exp\left[-6.8\times10^{7}\frac{\phi^{\frac{3}{2}}}{F}\right]amp/cm^{2} \qquad (1)$$

where μ is the Fermi level, φ is called work function, which is the solid state equivalent of ionization potential that corresponds to the energy difference between μ and a field free vacuum near the surface. F is the applied electric field in V/cm.

Standard Forler-Nordheim (F-N) equation is based on a series of assumptions as follows.

(i) The metal has a free electron band structure;

(ii) The electrons obey Fermi-Dirac statistics;

(iii) Temperature is 0 °K;

(iv) Metal surface is flat and smooth;

(v) The work function is uniform everywhere on the emitting surface and is not affected by the external electric field;

(vi) The external electric field is uniform;

(vii) The interactions between emitted electrons and metal surface are representable by a classical image potential;

(viii) Barrier penetration coefficients can be estimated with Jeffreys-Wentzel-Kramers-Brillouin (JWKB) approximation.

By neglecting the electron-metal surface interactions, the F-N equation can be rewritten as [77]:

$$J = \frac{i}{A} = \frac{k_1}{\phi} F^2 \exp\left[-\frac{k_2}{F} \phi^{\frac{3}{2}} \right], \text{ with}$$

$$k_1 = \frac{e^3}{8\pi h_P} = 1.541 \times 10^{-6} AeVV^{-2}, \text{ and}$$

$$k_2 = \frac{4\sqrt{2m_e}}{3e\hbar_P} = 6.831 \times 10^9 eV^{-\frac{3}{2}} Vm^{-1},$$

where e and m_e are the elementary charge and mass of electron, $h_P = 2\pi\,\hbar_P$ is Planck's constant.

The above equations were based on the assumptions mentioned. If one or more of the assumptions have to be relaxed, a generalized F-N equation should be used:

$$J = \frac{i}{A} = \frac{\lambda_1 k_1}{\phi} F^2 \exp\left[-\frac{\lambda_2 k_2}{F}\phi^{\frac{3}{2}}\right],$$

where λ_1 and λ_2 are generalized correction factors that may depend on ϕ, F, or other parameters.

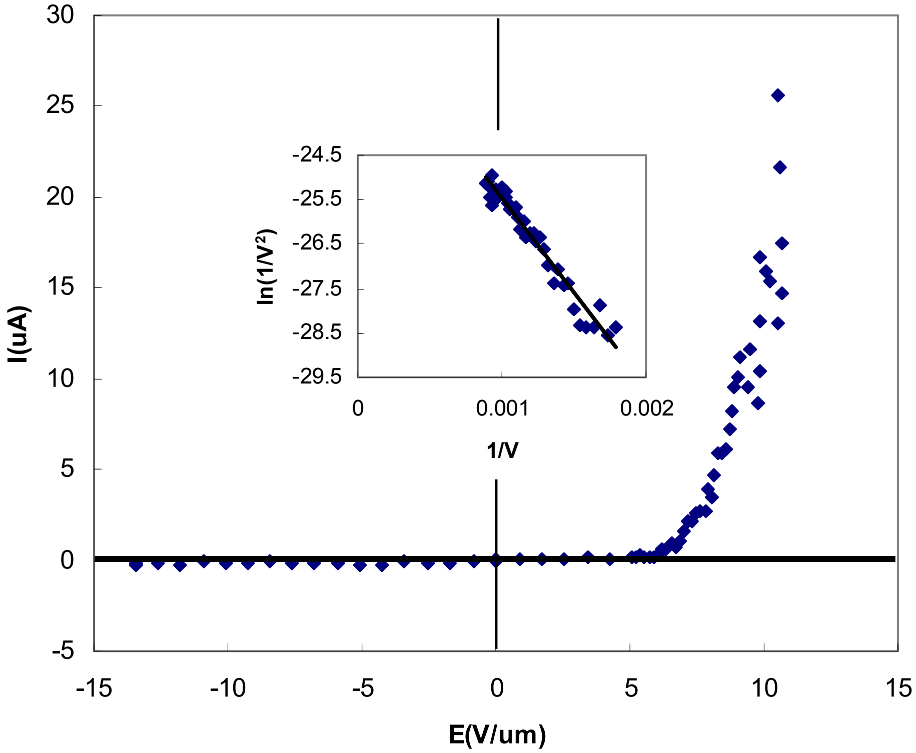

Fig. 2.1. A typical I-E curve and Fowler-Nordheim (F-N) plot (inset) for a field emission cathode (S. Wei et al, unpublished data).

Figure 2.1 shows a typical I-E curve and Fowler-Nordheim (F-N) plot for a field emission cathode. With the increased electric field, the emission current raises exponentially. This is a significant advantage of field emission over thermionic emission because the emission current has a nearly linear relationship with temperature for the latter.

Supercapacitors

Supercapacitors, sometimes referred to as ultracapacitors or electrochemical capacitors, store electric charges at the electrode-electrolyte interface. Structure of a typical supercapacitor consisting of two porous electrodes is shown in Figure 2.2 and Figure 2.3 [78]. While charging, the positive cations are attracted to the negative electrode, and the negative anions are moving towards the positive electrode.

The first patented supercapacitor was reported in 1957 [79] while the first commercial supercapacitors appeared in 1969 [80]. Supercapacitors store energy inside the electrochemical double layer (also referred to as Helmholtz layer) at electrode-electrolyte interface. Both negative and positive ions in the electrolyte accumulate at the electrode surface to compensate for the electronic charge. The double layer thickness is usually determined by the electrolyte concentration and the ion size. In concentrated electrolytes, it varies between 5 and 10 angstroms [81]. The double layer capacitance for an electrode with smooth surface and concentrated electrolyte is typically in the range of 10 ~ 20 uF/cm^2 and can be estimated by the following equation:

$$C / A = \varepsilon_0^* \varepsilon_r / d$$

based on the assumption that ε_r equals 10 for water in the double layer [82]. A and d are the surface area and thickness of the double layer, respectively. According to the equation, the capacitance is proportional to the electrode surface area. Therefore, a higher capacitance can be obtained by making electrodes from porous materials with very large effective surface.

Fig. 2.2 shows the basic structure of a single cell double layer supercapacitor [81]. The two electrodes are separated by a porous separator and filled with electrolyte. The potential drop across the cell is depicted in the figure too.

If a single electrode made of carbon has 1000 m^2/g of surface area and a double layer capacitance of 10 uF/cm^2, then the specific capacitance would be 100 F/g. A supercapacitor with two identical electrodes made of the same material should have a specific capacitance of 25 F/g ($1/C=1/C_1 + 1/C_2$). Therefore, it should always be clarified if the measured capacitance is from a single electrode or a two-electrode capacitor.

The maximum of energy stored in a supercapacitor is calculated by:

$$W = 1/2CU_0^2$$

If the cell voltage U_0 is 1V (typical for aqueous electrolyte), the specific energy stored would be 12.5 kJ/kg. While an organic electrolyte is used, the cell voltage will be increased to 2.3V and the specific energy will be 66.1 kJ/kg. Although organic electrolytes can achieve higher cell voltage, the specific resistance is 20~50 times higher than that of aqueous electrolytes. The increased resistance of electrolyte affects the equivalent distributed resistance of the porous layer thus reduces the maximum obtainable power which is determined by the following:

$$P = U^2 / 4R$$

where R is the total effective series resistance (ESR).

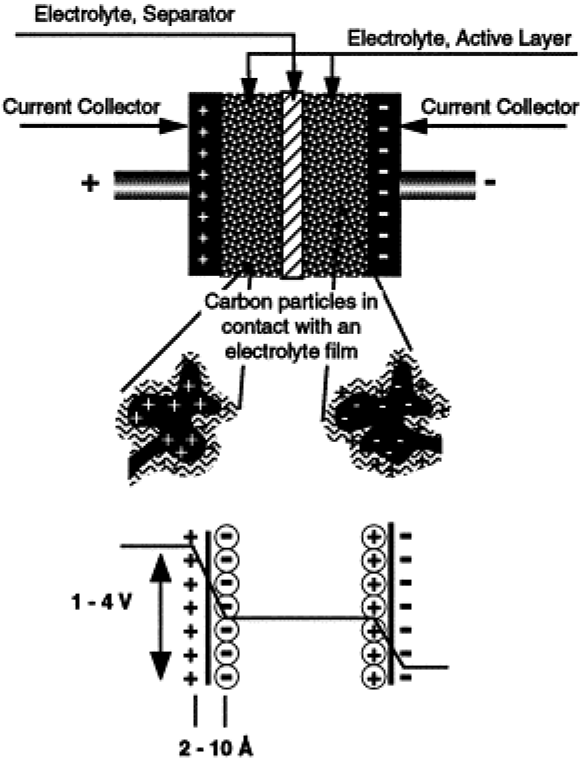

Fig. 2.2. Schematic of a supercapacitor and the potential drop at the electrode-electrolyte interfaces.

Carbon is a very popular material for supercapacitor applications mainly due to its relatively low cost and versatility in geometric forms. It is well known that the ideal supercapacitor electrode material should possess large surface area and pores of the size that can accommodate ions [83-84]. One group of materials that fits the requirements is activated carbons. In fact, activated carbons are the most popular supercapacitor electrode material at present. Depending on the nature of carbon precursor and activation process, the size of pores in activated carbons can be controlled. An appropriate combination of temperature, duration of activation process and activating agent may help produce the optimum density of mesopores. The best way to produce activated carbons with the right size of pores is the template process, although it is a more costly method [85-86].

Another approach to improve the capacitance is to add heteroatoms such as nitrogen and oxygen, into carbon network [87-89]. These heteroatoms have a doping effect on carbon materials and give rise to pseudocapacitive faradaic reactions therefore increase the overall capacitance.

The electrolytes used for supercapacitors can be roughly classified into two major groups: aqueous and nonaqueous, while the latter includes organic electrolytes and ionic liquids. In most cases, the operating voltage of a capacitor in aqueous solutions is below 1V. Organic solutions and ionic liquids can be operated at higher voltages. For example, capacitors in acetonitrile-dissolved tetraethyl ammonium tetrafluoroborate may work under a voltage up to 2.3V. Ionic liquids are made from organic cations and anions which are thermally stable with very low vapor pressure and high viscosity [90]. The operating voltage in ionic liquids can reach 3-3.5V. Despite the higher operating voltage range, the capacitance in ionic liquids is limited by the lower electric conductivity and high viscosity of such liquids that worsens the wetting of carbon electrodes. An effective way to improve the wetting in ionic liquids is to slightly increase the temperature. Figure 2.4 demonstrates a nearly linear relationship between temperature and specific capacitance of an activated carbon electrode in a trigeminal tricationic ionic liquid [78]. The conductivity at elevated temperature is also improved, which is another contribution to the enhanced capacitance. However, the need of increased temperature significantly limits the applications of ionic liquids. Most current ionic liquids are acetonitrile based and present serious hazard to the environment. Acetonitrile-free ionic liquids, albeit available, are very costly and the long term reliability of such liquids is not clear.

Therefore, most electrolytes for commercial applications today are either aqueous or $TEABF_4$ (tetraethyl ammonium tetrafluoroborate) based organic solutions.

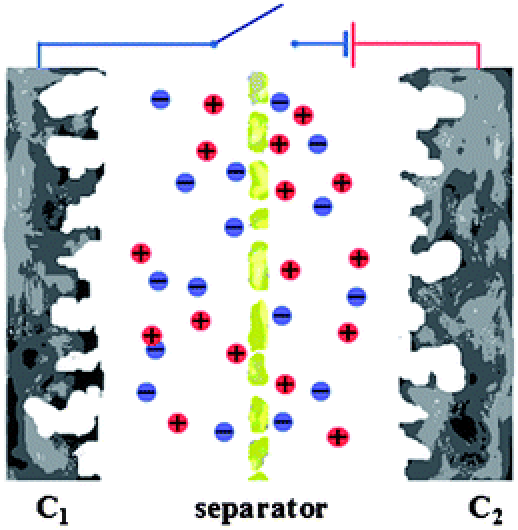

Fig. 2.3. Operation mechanism of an electrochemical supercapacitor.

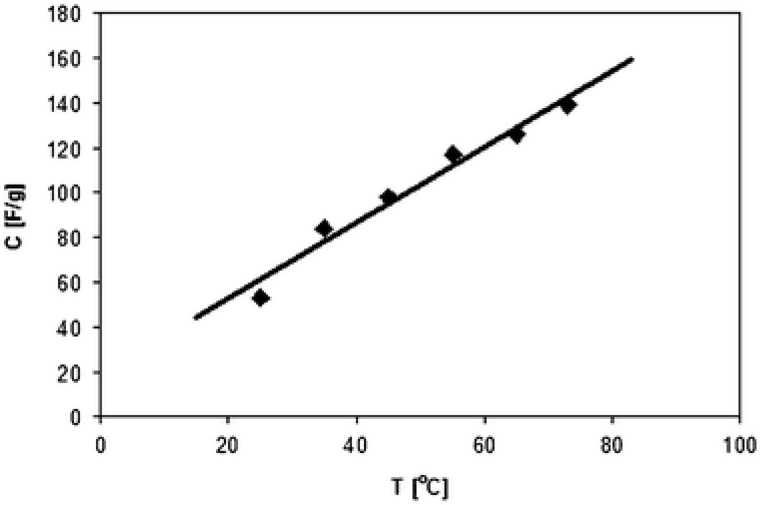

Fig. 2.4. Temperature dependence of specific capacitance for activated carbon electrode in trigeminal tricationic quat electrolyte.

For carbon materials, the capacitance, or the charge storing capacity is generally increased with higher surface area. It is generally agreed that micropores of size less than 2 nanometers play a critical role in the formation of electrochemical double layers. But in a bulk electrode, mesopores of size 2-50 nanometers are also necessary for fast charging and discharging. In some cases, higher specific surface area does not necessarily guarantee higher capacitance. This is due to the sizes and structure of the pores. Depending on the size of electrolyte ions, some small micropores may construct obstacles and make the ion propagation difficult [91-92]. Poor interconnectivity between pores may also prohibit the ions from moving through bulk carbon electrodes. The specific capacitance of activated carbons is usually about twice as high in aqueous solutions than organic electrolytes thanks to the smaller size of ions and higher dielectric constant of aqueous solutions.

Compared to activated carbons, carbon nanotubes are more electronically conductive and far stronger mechanically. These properties make CNTs ideal supporting networks for active materials. The vacancies between individual nanotubes can be considered a huge and open network of interconnecting mesopores. This type of structure makes the diffusion of electrolyte through the entire carbon network much easier, therefore the active material deposited on CNTs can be readily accessible by ions. These characteristics are critical to reduce the ESR (effective series resistance) thus increase the power density. In addition, the high resilience of CNTs helps the electrodes adapt easily to shape and volume changes caused by charging and discharging, consequently improves the cycling life. Because of these advantages, carbon nanotubes mixed with active materials of high pseudocapacitance are very promising composite materials for developing high performance capacitor electrodes.

There are two major groups of pseudocapacitive materials: electrically conducting polymers (ECPs) [93] and transition metal oxides (TMOs) [94].

To prepare CNT-ECP composites, carbon nanotubes are usually polymerized with aniline, pyrrole, or other monomers. Figure 2.5 shows CNTs uniformly coated with ECP by electrochemical deposition [95]. Both single-walled [96] and multi-walled CNTs [95, 97] can be deposited with uniform layer of polypyrrole. During this electrochemical deposition process, CNTs are functionalized and the oxygen-containing surface groups attached to CNT surfaces serve as anionic dopants for the polypyrrole films [98]. Such films demonstrate much higher flexibility and better adhesion to the CNT electrodes than their counterparts produced using aqueous electrolytes.

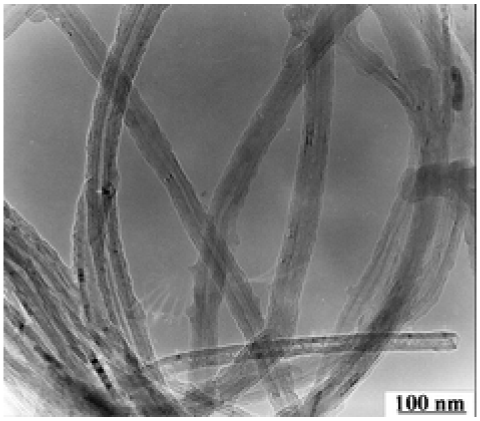

Fig. 2.5. Electrochemically prepared PPy/CNT composite [95].

ECPs, however, are mechanically weak and not very stable chemically. They can easily deform during charging and discharging, and are prone to mechanical degradation which may lead to poor capacitor performance.

As stated before, TMOs are also good pseudocapacitors as they generate fast faradaic reactions. Among these materials, ruthenium dioxide (RuO_2) demonstrates the best known specific capacitance and excellent cycle life. For example, very high specific capacitance of about 770 F/g [99] can be obtained from amorphous hydrous RuO_2 prepared via sol-gel technique. The application of RuO_2 in supercapacitors is limited, however, due to the extremely high cost of such material. To search for alternative TMO materials, IrO_2, NiO_x, PdO, MnO_2, and other oxides were explored. Among them, MnO_2 has drawn particular interest mainly because of the specific capacitance comparable to RuO_2 and its low cost. Mn constitutes 0.1% of earth crust therefore is readily available and MnO_2 can be obtained for very low price.

Because of the low electronic conductivity, MnO_2 can not be used as supercapacitor electrode in bulk form. It must be dispersed onto a conductive supporting material. Carbon nanotube is an ideal supporting material because of its outstanding electrical conductivity and its porous structure providing high surface area which is critical for supercapacitor performance.

CNT Synthesis by CVD and PECVD

The apparatus for thermal CVD is usually a quartz tube heated in a tube furnace therefore is a hot wall system [100-101]. Early CVD processes utilized pumping systems to maintain a pressure in the range of a few torrs to tens of torrs inside the tube. This work is focused on CVD processes at atmospheric pressure so no pumps are needed and the synthesis is much simplified. The carbon feedstock, usually CO, CH_4, C_2H_2, C_2H_4, etc, is metered through a flowmeter or mass flow controller. A typical growth cycle starts with tube purging by flowing hydrogen, or inert gas, like Ar or nitrogen. These gases are often referred to as carrier gases or shielding gases because they usually flow through tube furnace from room temperature all the way up to the reaction temperature to protect the substrates and catalysts from being oxidized. When the temperature is stabilized at the desired level for CNT growth, carbon feedstock is introduced. In some cases, carrier gases are switched off at the time carbon feedstock is turned on, but in other cases, they are kept flowing to further protect the catalysts and dilute the hydrocarbon. When the growth period is finished, carbon feedstock is switched off and the system is cooled down to room temperature (or below 200°C) in shielding gases. The temperature for CNT growth with CVD is usually below the pyrolysis temperature of the carbon feedstock to prevent excessive generation of amorphous carbon. During CVD process, dissociation of carbon feedstock, or so-called precursor, mainly happens at the gas-catalyst interface. The dissociation of precursor in the gaseous environment is almost negligible [102-103]. Therefore, thermal CVD growth of CNTs can only occur at 500°C or higher temperature because lower temperature is not enough to activate the catalytic process.

PECVD, on the other hand, can produce CNTs or carbon nano fibers (CNFs) at much lower temperature. Successful growth of CNTs / CNFs was reported at 120°C [52, 104]. However, it must be pointed out that the low temperatures recorded may not be the actual wafer temperatures. In situ temperature monitoring is often difficult and the temperatures are usually measured from below the heater stage with thermocouples. The wafer exposed to plasma heating and ion bombardment can be at a temperature significantly higher than that of the stage [105]. Therefore, PECVD is essentially a cold-wall system. Another major difference between CVD and PECVD is the underlying chemistry. Methane is a commonly used carbon feedstock for both CVD and PECVD synthesis of CNTs. It is confirmed that during thermal CVD process at a temperature of 900°C or below, methane is stable in the gaseous environment and does not dissociate into any other hydrocarbons [102-103]. While during PECVD process, methane breaks into various radicals and hydrocarbons such as ethane, acetylene, ethylene, etc., due to the plasma [102-103]. These different forms of hydrocarbon and radicals need lower activation energy to dissociate therefore can produce CNTs at lower temperature.

CHAPTER III

PROPOSED RESEARCH AND APPROACHES

This chapter deals with the experimental details of catalyst preparation, CNT synthesis, fabrication and characterization of CNT field emitters and supercapacitors.

CNT Field Emitters by Thermal CVD with Palladium as Catalyst

The details of the experimental procedure, pretreatment and synthesis parameters, for all the samples described in these sets of experiments, are summarized in Table 3.1.

The substrates used are n-type <100> Si (resistivity 0.002-0.005Ohm-cm) wafers coated with a thin layer of Ti (~10nm thick) as a diffusion barrier for Pd to prevent the formation of palladium silicide. The pressure in the sputtering system is about ~10^{-6} torr. These wafers were then sputter-coated with a Pd layer, thickness of which is 10, 20, and 30nm, respectively, for each wafer. The thickness values were estimated based on the sputtering time and applied power and were taken from archived data.

The thermal CVD reactor is a 2-inch-diameter horizontal quartz tube furnace (Fig. 3.1). For each experiment, the samples were inserted facing-up into the reactor at room temperature, then heated to 750°C at 15°C/min in either Ar/H_2 (4:1) or pure Ar. For the study of H_2 effect on the catalyst particles, three samples (1a-1c) with 10nm, 20nm, and 30nm Pd film, respectively, were heated to 750°C in the reactor, dwelt for 10min, then furnace-cooled to the room temperature. Pure Ar gas was flowing through the tube at 75 sccm during the entire heating-dwelling-cooling cycle. Another set of samples (set 2) was treated under the same conditions except that, instead of pure Ar, a mixture of Ar/H_2 (4:1) was introduced. After the experiments, these two sets of samples were examined with SEM to determine the difference in Pd particle size, density, and morphologies. To understand the effect of NH_3 on the Pd particle size distribution, another two sets of identical samples (sets 3 and 4) were heated to 750°C at 15°C/min in Ar/H_2 (4:1) with the same flow rate of 75 sccm, then NH_3 was introduced at 40 sccm into the reactor, after 1min and 10min dwellings for sets 3 and 4, respectively, NH_3 was shut off and the samples were furnace-cooled to room temperature in Ar/H_2 (4:1). The effect of NH_3 was obtained by comparing the SEM images taken from the samples of sets 2, 3, and 4. To investigate the effect of processing parameters on the as-grown CNT diameter and density, five sets of identical samples (sets 5 through 9) were prepared and tested.

A Hitachi field emission scanning electron microscope (SEM) was used to characterize the catalyst particle size/density and the CNTs morphologies. Raman spectra of the as-grown CNTs were obtained using JOBIN YVON micro-Raman LabRam system. The field emission tests were performed in a parallel plate diode configuration at room temperature in vacuum of ~10^{-6} Torr, as illustrated in Fig. 3.2. The gap between the Si anode and the CNT cathode was set at 80 um by a mica spacer, the emitting area was about 0.8 mm^2. The field emission current was measured as a function of the anode voltage.

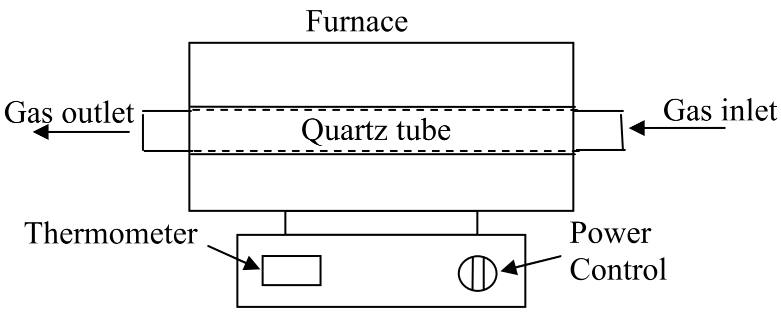

Fig. 3.1. Thermal CVD system setup.

Table 3.1. Test procedures for Pd particle size distribution and CNT growth

Set #	Heating at 15°C/min to 750°C, gases (sccm)	Dwelling duration, gases (sccm)	Growth duration, gases (sccm)	Cooling duration, gases (sccm)
Palladium particle experiments				
1a-1c	Ar(75)	10 min, Ar(75)	Skipped	Furnace cooled from 750°C to room temperature in $Ar/H_2(75)$
2a-2c	$Ar/H_2(75)$	10 min, Ar/H_2 (75)		
3a-3c		1min, $Ar/H_2(75)$+ 97ppm$NH_3(40)$		
4a-4c		10min, $Ar/H_2(75)$+ 97ppm$NH_3(40)$		
CNT growth experiments				
5a-5c	$Ar/H_2(75)$	10 min, Ar/H_2 (75)	10min, $Ar/H_2(75)+CH_4(40)$	Furnace cooled from 750°C to room temperature in $Ar/H_2(75)$
6a-6c			10min, $Ar/H_2(75)+CH_4(125)$	
7a-7c			10min, $Ar/H_2(75)+CH_4(125)$+ 97ppm$NH_3(120)$	
8a-8c		1min, $Ar/H_2(75)$+ 97ppm$NH_3(40)$		
9a-9c		10min, $Ar/H_2(75)$+ 97ppm$NH_3(40)$		

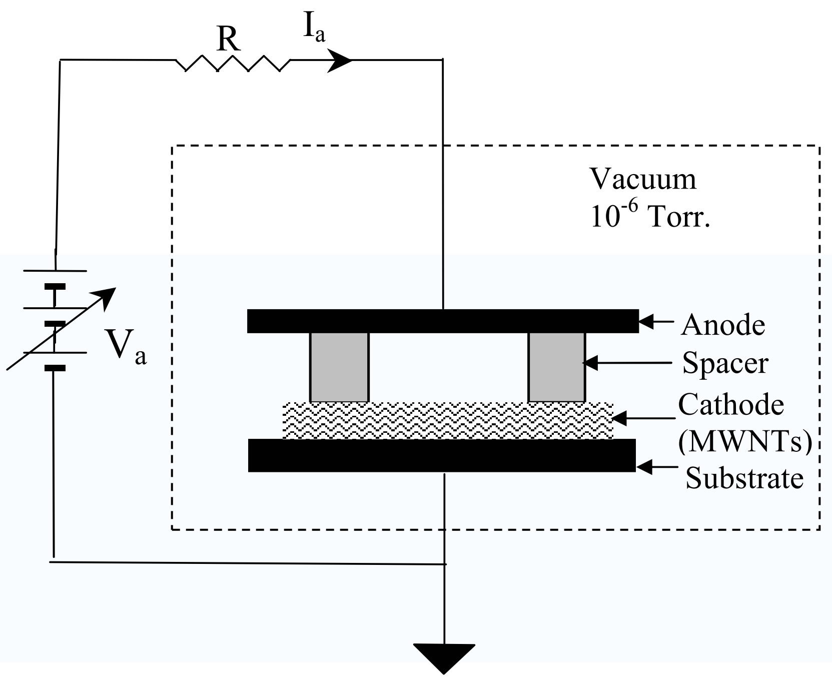

Fig. 3.2. Schematic of field emission test on CNT diode structure.

CNT Field Emitters by Thermal CVD with Nickel as Catalyst

The substrates used here are p-type Si wafers with 150nm-thick SiO_2 on the Si top surface. The substrates were sputter-coated with Ni catalyst in 10^{-6} torr vacuum. The thickness of the sputtered Ni layers was measured by optical ellipsometry. A total of 24 samples were prepared. These samples were then allocated into 8 sets, each set contains 3 samples, marked as a, b, and c, corresponding to 6, 9, and 11nm thick Ni film on SiO_2 surface, respectively.

A total of eight experiments were conducted (Table 3.2), four of them designed to study the effects of Ni film thickness and ammonia reagent gas on the size and density of Ni particles. They are referred to as Ni particle experiments. The other four experiments were intended to investigate the relationship between the synthesis parameters and the morphology of as-grown CNTs. These are named CNT growth experiments throughout this section. For each experiment, three samples (a-c) from one set were loaded facing-up on a quartz boat and inserted into the tube furnace at room temperature, then heated to 750°C at 15°C/min in a mixture of Ar / H_2 (4:1). The flow rate of Ar/ H_2 was maintained at 75 sccm. This gas mixture was used to prevent the Ni catalyst from being oxidized. After the temperature stabilized at 750°C, diluted ammonia (19.4% NH_3 and balance of N_2) was introduced into the furnace for Ni particle experiments. The flow rate of NH_3 / N_2 was 0 (no ammonia introduced), 24, 32, and 43 sccm, respectively, for sets 1, 2, 3, and 4. After 30 minutes annealing in (Ar/ H_2)+ (NH_3 / N_2) environment, NH_3 / N_2 was shut off and the samples were furnace-cooled to room temperature in 75 sccm of Ar/ H_2. For CNT growth experiments, when the temperature was stabilized at 750°C, acetylene (C_2H_2) at flow rate of 12 sccm was introduced, as the carbon source, along with NH_3 / N_2. While the acetylene flow rate was the same, the flow rate of NH_3 / N_2 was 0 (no ammonia introduced), 24, 32, and 43 sccm, respectively, for sets 5, 6, 7, and 8. After 30 minutes CNT growth in the (Ar/ H_2) + (NH_3 / N_2) + C_2H_2 environment, NH_3 / N_2 and C_2H_2 were shut off and the samples were furnace-cooled at 75 sccm of Ar/ H_2. The detailed procedures of the above-mentioned eight experiments are summarized in Table 3.2.

A Hitachi 4200 field emission scanning electron microscope (SEM) was used to characterize the catalyst particle size/density for sample sets 1-4 and the CNTs morphologies on sample sets 5-8. Raman spectra of the as-grown CNTs were obtained using JOBIN YVON micro-Raman LabRam system for analysis of the CNT structures. The field emission tests were performed in a parallel plate diode configuration at room temperature in vacuum of $\sim 10^{-6}$ Torr. The gap between the Si anode and the CNT cathode was set at 110 um by a mica spacer, the emitting area was about 2 mm^2. The field emission current was measured as a function of the anode voltage.

Table 3.2. Test procedures of Ni particle and CNT growth experiments.

Set number	Heated to 750°C at 15°C/min, gases (sccm)	Annealing, gases(sccm)	CNT growth, gases (sccm)	Cooling, gases (sccm)
Ni particle experiments				
1	Ar/H_2 (75)	30 min, Ar/H_2 (75)	Skipped	Furnace cooled from 750°C to room temperature in Ar/H_2 (75)
2		30 min, Ar/H_2 (75)+ NH_3/N_2 (24)		
3		30 min, Ar/H_2 (75)+ NH_3/N_2 (32)		
4		30 min, Ar/H_2 (75)+ NH_3/N_2 (43)		
CNT growth experiments				
5	Ar/H_2 (75)	Skipped	30min, Ar/H_2 (75)+C_2H_2(12)	Furnace cooled from 750°C to room temperature in Ar/H_2 (75)
6			30min, Ar/H_2 (75)+ NH_3/N_2 (24)+C_2H_2(12)	
7			30min, Ar/H_2 (75)+ NH_3/N_2 (32)+C_2H_2(12)	
8			30min, Ar/H_2 (75)+ NH_3/N_2 (43)+C_2H_2(12)	

CNT Field Emitters by Thermal CVD with Cobalt as Catalyst

The substrates chosen for this work are p-type Si wafers with 1500Å uniform thermal oxide on top surface. The Co catalyst is deposited on the SiO_2 surface in vacuum (~5x10^{-6} torr) using DC magnetron sputtering. The test matrix consists of 18 samples (Table 3.3), divided into six groups, 3 samples each, and denoted with the combination of a digit and a letter. For example, 1a through 1c represent all three samples in Group 1, while samples in Group 6 are marked 6a through 6c. Letters a, b, and c correspond to 19, 28, and 31nm thick Co film, respectively.

The first three experiments are designed to examine the effect of Co film thickness and ammonia flow rate on the size and density of Co particles and are designated “Co particle experiments” in Table 3.3. A different three sets of experiments are designated to study interrelation between the catalyst precursors, process parameters and as-grown CNTs. These are referred to as “CNT growth experiments”. For each experiment, a group of three samples (a-c) is placed on a quartz plate and loaded into the tube furnace at room temperature, then heated to 750°C at 15°C/min in a mixture of Ar/H_2 (4:1), which serves as the shielding gas to keep the catalyst from being oxidized. The flow rate of Ar/H_2 is maintained at 75 sccm throughout each experimental cycle. When the temperature is stabilized at 750°C, diluted ammonia (19.4% NH_3, balance of N_2 designated NH_3/N_2) is introduced into the tube for the Co particle experiments. The flow rates of NH_3/N_2 are 0 (no ammonia introduced), 16, and 24 sccm, respectively, for experiments 1, 2, and 3. After 30 minutes annealing in (Ar/H_2)+ (NH_3/N_2) environment, NH_3/N_2 is shut off and the samples are furnace-cooled to room temperature in 75 sccm of Ar/H_2. For CNT growth experiments, when the temperature is stabilized at 750°C, acetylene (C_2H_2) at a fixed flow rate of 12 sccm is introduced, after 10 seconds of NH_3/N_2 pretreatment. With the acetylene flow rate kept constant, the flow rate of NH_3/N_2 was varied from 0 (no ammonia introduced), 16, to 24 sccm, respectively, for experiments 4, 5, and 6. After 30 minutes of CNT growth in the $(Ar/H_2) + (NH_3/N_2) +$ C_2H_2 environment, NH_3/N_2 and C_2H_2 are turned off and the samples furnace-cooled under 75 sccm of Ar/H_2. The detail experimental steps for the complete test matrix are summarized in Table 3.3.

A Hitachi 4200 field emission scanning electron microscope (SEM) was used to characterize the catalyst particle size/density for sample groups 1-3 and the CNTs morphologies on sample groups 4-6. The microstructures of as-grown CNTs were further examined with a Philips CM-20 transmission electron microscope (TEM). Raman spectra of the as-grown CNTs are obtained from a JOBIN YVON micro-Raman LabRam system for analysis of the CNT properties. The field emission tests are performed at room temperature in vacuum of ~10^{-6} Torr. The gap between the Si anode and the CNT cathode is maintained at 110 um by mica spacers, the effective emitting area is estimated to be 2 mm^2. The field emission current was measured as a function of the anode to cathode electric field (voltage).

Table 3.3. Experimental procedures for Co particle treatment and CNT growth.

Set Number	**Heated to 750°C at 15°C/min** Gases (sccm)	**Annealing** Gases (sccm)	**CNT Growth** Gases (sccm)	**Cooling** Gases (sccm)
Co particle experiments				
1	Ar/H_2 (75)	30 min, Ar/H_2 (75)	Skipped	Furnace cooled from 750°C to room temperature in Ar/H_2 (75)
2		30 min, Ar/H_2 (75) + NH_3/N_2 (16)		
3		30 min, Ar/H_2 (75) + NH_3/N_2 (24)		
CNT growth experiments				
4	Ar/H_2 (75)	Skipped	30min, Ar/H_2 (75) + C_2H_2(12)	Furnace cooled from 750°C to room temperature in Ar/H_2 (75)
5		10 seconds, Ar/H_2 (75) + NH_3/N_2 (16)	30min, Ar/H_2 (75) + NH_3/N_2 (16)+C_2H_2(12)	
6		10 seconds, Ar/H_2 (75) + NH_3/N_2 (24)	30min, Ar/H_2 (75) + NH_3/N_2 (24)+C_2H_2(12)	

CNT-Based Supercapacitors Fabricated by MPECVD

The reactor for CNT synthesis is a microwave vacuum system. The substrates are 1.5 cm by 1.5 cm, cut from n^{++} <100> Si wafer (resistivity 0.002-0.005Ohm-cm). Thin layer (~4 nm) of Ti is deposited, followed by a thin layer of Ni, using a DC magnetron sputtering system. The thin Ti layer serves as a buffer preventing the possible reaction between Si and Ni to form nickel silicate and to improve the CNT film adhesion to the silicon substrate. The thickness of Ni catalyst varies between 2~5 nm and is used as a controlling parameter of catalyst size and density for CNTs synthesis.

After loading a sample into the MPECVD system (Fig. 3.3), the reactor chamber is evacuated to ~ 0.02 torr. Hydrogen is then introduced at 120 sccm, for 5 minutes, to purge the chamber. After purging, the hydrogen pressure in the chamber is raised and maintained at ~ 20 torr. The substrate is then heated from room temperature to 650 °C at ~ 50 °C/min. Once the temperature is stabilized at 650 °C, the microwave hydrogen plasma is initiated and maintained at 400 W for 1 to 7 minutes, before CH_4 is introduced. The pause of 1 to 7 minutes serves as another process controlling parameter for CNTs growth along with the catalyst film thickness, and will be refered to as (hydrogen) plasma pretreatment time, or simply pretreatment time. After the pause, methane is introduced at ~15 sccm for 1 minute to synthesize CNTs and shut off thereafter, followed by plasma turn-off and cooling down to room temperature in hydrogen flow environment.

The as-grown CNT thin films are examined with scanning electron microscope (SEM), transmission electron microscope (TEM), Raman spectroscopy. The supercapacitor behavior of the CNT samples was characterized by cyclic voltammetry. The voltammetric measurements are performed at room temperature in the standard three-electrode configuration, with Pt wire as the counter electrode and Ag/AgCl as the reference electrode. A 0.1M KCl aqueous solution is used as the electrolyte.

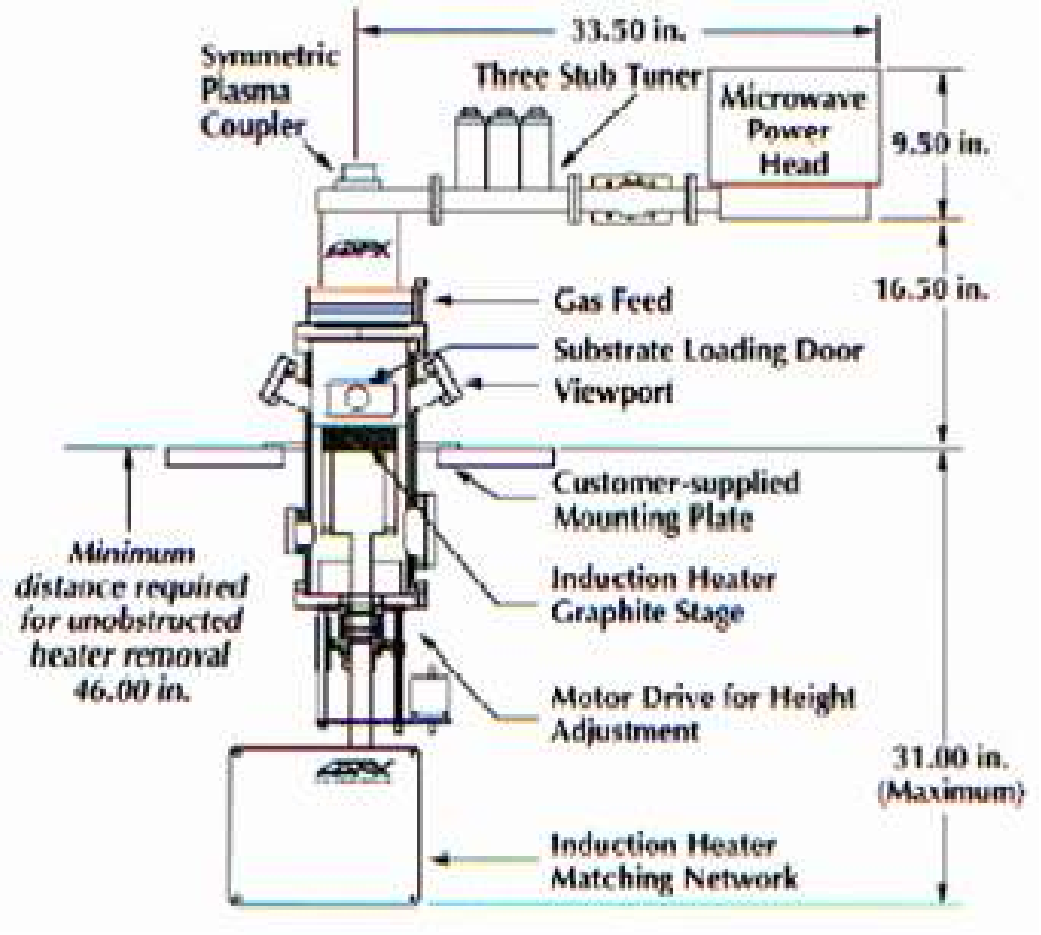

Fig. 3.3. Schematic of MWPECVD system.

Supercapacitor Electrodes Based on CNT Thin Film and Manganese Dioxide

Silicon wafers with n-type doping (resistivity 0.002-0.005Ohm-cm) are cleaned in diluted hydrofluoric acid to remove the native oxide. The wafers are then rinsed in de-ionized water and dried. A thin buffer layer of Ti film (~5nm) is deposited on these wafers using a DC magnetron sputter system, followed by a thin Ni film as catalyst. These wafers are loaded into a microwave plasma-enhanced chemical vapor deposition (MPCVD) system to grow CNT thin film. Hydrogen-diluted methane is used as carbon source. After the synthesis of CNT, these wafers are cut into square pieces of equal size, about 1cm by 1cm and these cut pieces will serve as test samples for their supercapacitor behavior later on.

Preparation of Manganese Dioxide

An over-saturated potassium permanganate aqueous solution is prepared in a beaker by mixing $KMnO_4$ crystal (purity ~99.5%) with de-ionized water. Absolute alcohol (>99.95%) is then drop-wise, slowly added into the beaker, the beaker is being hand shaken during the process to ensure uniform mixing. By adding extra quantity of alcohol, the solution eventually becomes colorless and some MnO_2 precipitate of dark brown color is readily observed at the bottom of the beaker. The solution along with MnO_2 precipitate is filtered through filter paper so that MnO_2 can be collected. After drying out at room temperature, the MnO_2 is obtained in the form of powder. A small quantity of such powder is picked up and placed into a capped vial prefilled with acetone. The vial is then placed into an ultrasonic cleaner for a few minutes to help dissolve the precipitate in acetone. As the result, a yellow-colored MnO_2/acetone suspension is produced. This suspension is then added onto the prepared $1cm^2$ samples drop-wise. By varying the number of droplets applied to each sample, MnO_2/CNT mass ratio can be controlled. To ensure that the concentration of MnO_2 is the same for all samples, the suspension is made saturated. After the droplets dry out, the samples are observed on scanning electron microscope (SEM), X-ray photoelectron spectroscopy is utilized to determine the valence of manganese in the composite material, and electrochemical measurements are taken to estimate the capacitor performance. The MnO_2/CNT composite is also removed from a few samples and observed on transmission electron microscope (TEM).

CHAPTER IV

RESULTS AND DISCUSSION

This chapter presents and discusses the experimental results obtained so far.

CNT Field Emitters by Thermal CVD with Palladium as Catalyst

Figure 4.1 shows the effect of Pd film thickness as a function of gas pretreatment, prior to CNT growth. The SEM images show the Pd particles taken from all four sets of samples after the experiments. For each set, the Pd film thickness effect can be readily seen. The thicker the initial layer of Pd catalyst, the bigger the average size of Pd particles, but the density of particles decreases with the increased film thickness. This is similar to the results reported for other catalysts [106-108]. By comparing the images of sets 1 and 2, it can be clearly seen that H_2 has a significant effect on the shape of Pd particles. On the samples annealed in pure Ar, many catalyst particles have irregular shape characterized by angles and straight edges/facets. The addition of H_2 during the annealing process helps form more regular, round Pd particles as shown in Figure 4.1, which are suitable for nanotube growth. Analysis of the SEM images for sample sets 2, 3, and 4 reveal the effect of NH_3 pretreatment. Specifically, ammonia tends to break larger catalyst particles into smaller ones, thereby increases the density of Pd particles. Table 4.1 summarizes the Pd catalyst particle counts of sets 2 through 4. In general, the total number of Pd particles per unit area, defined as the particle density, increases with the time period of NH_3 pretreatment, while the particle size distribution becomes more diverse, i.e. the nonuniformity of Pd particle size increases with NH_3 pretreatment time.

CNT synthesis experiment with Pd catalyst was performed per the procedure described in previous chapter. Five sets of samples, three samples per set, were labeled 5a-5c, 6a-6c, 7a-7c, 8a-8c, and 9a-9c, respectively, where a, b, and c correspond to the initial Pd thin film thickness of 10, 20, and 30nm, accordingly. For samples 5a-5c and 6a-6c, no ammonia was involved during the entire CVD process. The difference between the two sets was the methane flow rate during CNT growth phase, 40 sccm for 5a-5c, and 125 sccm for 6a-6c. Samples 7a-7c were not pretreated in ammonia, 8a-8c were pretreated in ammonia for 1 minute and 9a-9c were pretreated in ammonia for 10 minutes. While the pretreatment recipes were different among the three sets, they were processed in the same way during the succeeding CNT growth period. As shown in Figure 4.2, there are almost no CNTs grown on samples 5a-5c and 6a-6c, which have not been exposed to NH_3. Samples 6a-6c were subject to a higher CH_4-to-Ar/H_2-ratio while have even less CNTs grown than samples 5a-5c. This indicates that higher partial pressure of CH_4 leads to the formation of more amorphous carbon which covers the catalyst particles therefore the CNT growth is hindered. Samples 7a-7c were exposed to CH_4 along with NH_3 at the same time, the effect of NH_3 at this stage is to protect the Pd catalyst by etching the amorphous carbon coating. As the result, CNTs were able to grow on the catalyst sites not covered by amorphous carbon. This protecting effect of NH_3 can be best understood by comparing samples 6b and 7c, which have virtually the same size and density of Pd particles, the only difference is that sample 7c was exposed to NH_3, while all other experimental conditions remained the same, the protected 7c was able to grow CNTs but nothing was grown on 6b. Samples 8a-8c were exposed to the same gaseous environment as 7a-7c during the growth, prior to that, however, they were treated in NH_3 for 1 minute, this pretreatment helped generate higher density of nucleation sites for CNTs by preventing the formation of amorphous carbon even before CNT growth. In other words, this pre-cleaning process allowed more nucleation sites to survive for CNT growth and resulted in higher CNT density on samples 8a-8c. The last three samples, 9a-9c, were subject to a longer pretreatment in NH_3, which made the pre-cleaning more complete, so the density of as-grown CNTs is the highest among all groups. This two-stage mechanism of NH_3 treatment is the same as reported elsewhere [108-112].

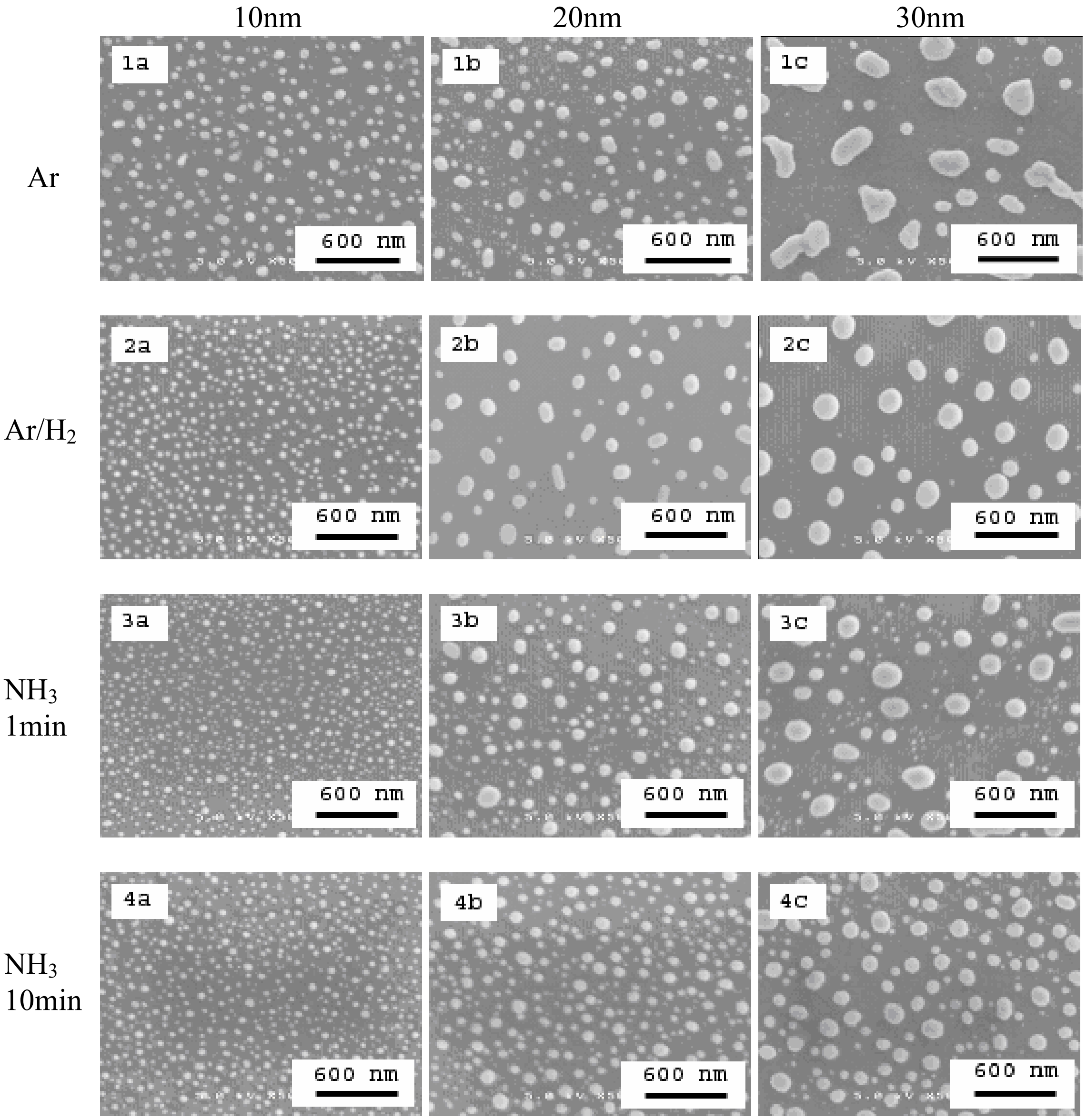

Fig. 4.1. Samples 1a through 1c are treated in pure Ar while samples 2a through 2c processed in Ar/H_2 (4:1), the SEM images strongly indicate the optimizing effect of H_2 on the shape and uniformity of Pd particles. Samples 3a through 3c and 4a through 4c are pretreated in NH_3 for 1 minute and 10 minutes, respectively, the SEM images demonstrate that NH_3 increases the density of Pd particles while decreasing their average size. Letters a, b, and c denote the initial Pd film thickness as 10nm, 20nm, and 30nm, respectively.

Table 4.1. Pd particle size distribution.

Diameter range of Pd particle , nm	Density of Pd particles* (number of particles per square micrometer in each diameter range) corresponding to NH_3 pretreatment time and Pd film thickness								
	0 minute			1 minute			10 minutes		
	10nm	20nm	30nm	10nm	20nm	30nm	10nm	20nm	30nm
< 20				37	19	18	104	28	19
21~40	20	3	3	86	12	10	56	29	15
41~60	106	3		102	17	12	94	40	8
61~80	8	3		28	10	2	4	19	8
81~100		4		1	4	1		7	6
101~120		4	2		6	3			5
121~140		3	1		3	2			2
141~160		3							
161~180			2			2			
181~200			2			4			2
Pd particle density (um^{-2})	134	23	10	254	71	54	258	123	65
Average particle size (nm)	48	91	116	40	49	56	30	42	51

* Densities of particles less than 1 per square micron are not listed in the table.

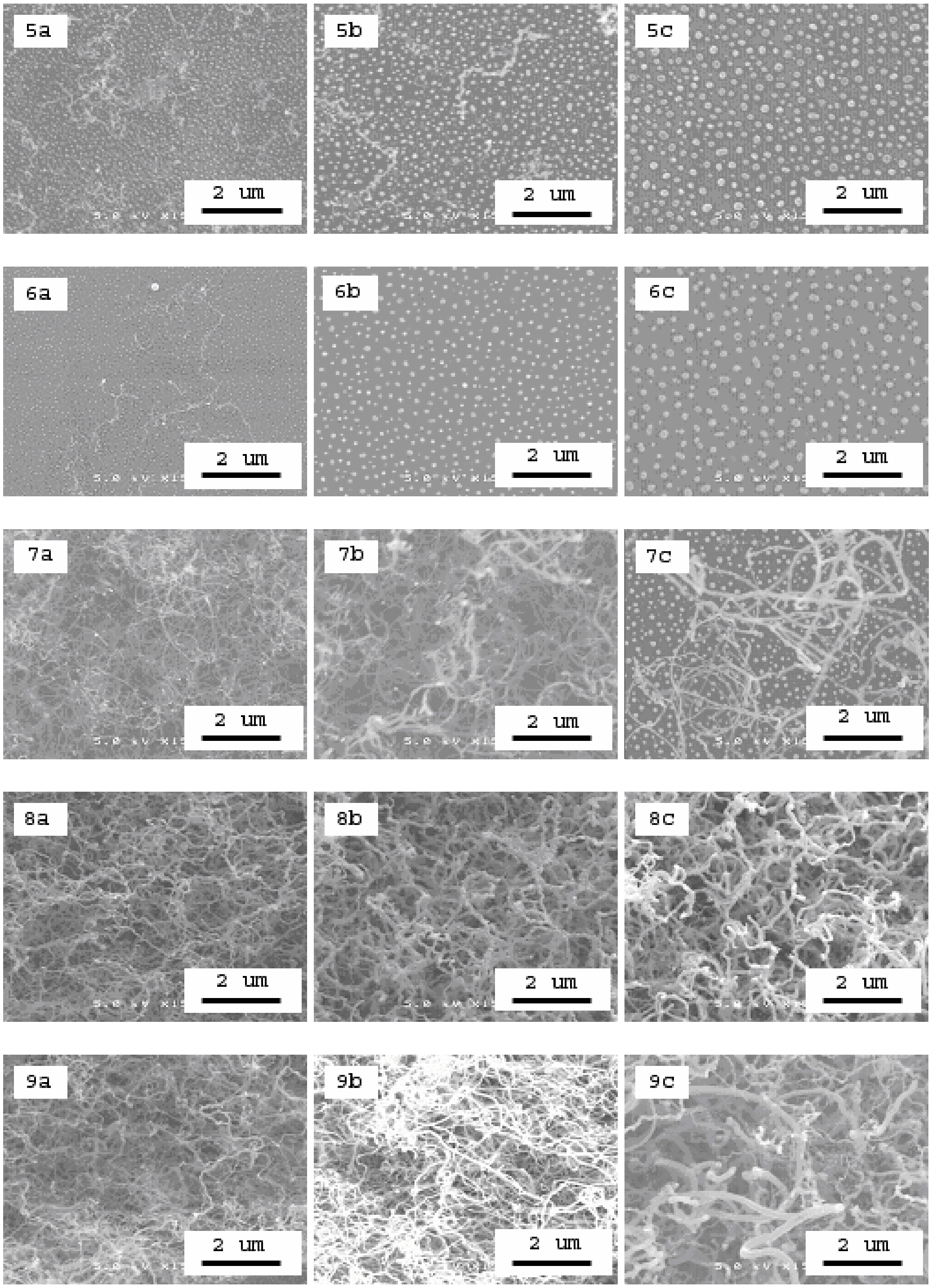

Fig. 4.2. Samples 5a-5c and 6a-6c are not exposed to NH_3 and have very few CNTs grown, higher CH_4 to Ar/H_2 ratio for 6a-6c does not help produce more CNTs, as compared to 5a-5c. Introducing NH_3 during CNT growth significantly increases the density of CNTs (7a-7c). NH_3 treatment prior to growth further increases CNT density (1 minute and 10 minutes pretreatment for 8a-8c and 9a-9c, respectively).

The SEM images in Figure 4.2 also demonstrate the correspondence between the size of Pd particles and the diameter of as-grown CNTs, i.e. the CNT diameter is approximately equal to the size of the Pd particle underneath, same as for other catalysts [106-108]. The density of CNTs, however, is not necessarily the same as of the catalyst particles since some or all of the nucleation sites may be covered by amorphous carbon. The as-grown CNTs have been imaged with transmission electron microscope (TEM). Figure 4.3 shows one of these CNTs. Both high- and low- magnification images demonstrate some Pd catalyst particles encapsulated in the nanotube. The individual graphene shells can not be seen in the pictures because the nanotube imaged had some amorphous carbon coated on it, which was verified by the electron diffraction pattern (not shown here). In fact, all the CNTs obtained for this work and observed by TEM had the amorphous carbon coating, which indicates that the CNTs produced by this method are multi-walled and of inadequate purity.

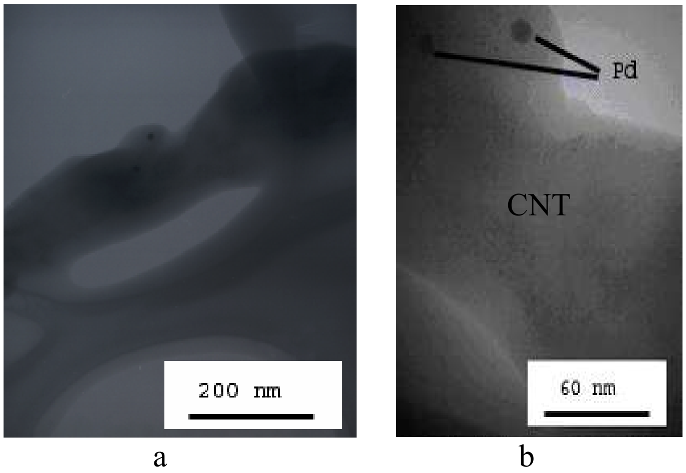

Fig. 4.3. Low (a) and high (b) magnification TEM images of Pd-catalyzed CNT. Some catalyst particles are trapped in the CNT body. The multi-walled structure can not be seen due to the amorphous carbon coating on the CNT surface.

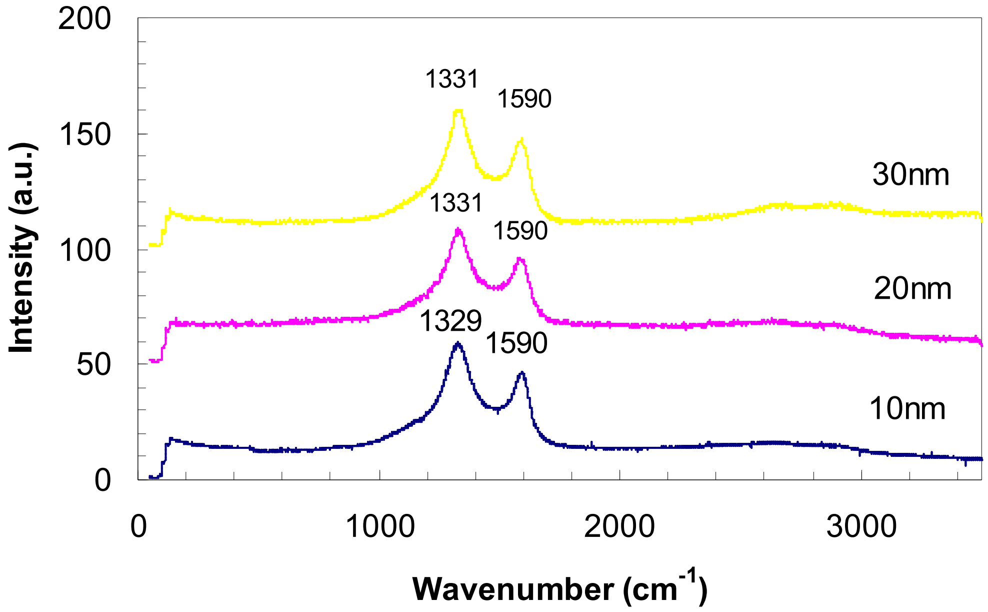

Fig. 4.4. Raman spectra of as-grown CNTs on samples 9a-9c, note the different initial Pd film thicknesses. I/(D)/I(G) varies between 1.25 and 1.48. Possible peaks at Raman shift below 50cm^{-1} are not recorded. Peaks at ~1330 and ~1590cm^{-1} are attributed to D-line and G-line, respectively. No apparent second-order peaks are observed.

The Raman spectra of the Pd-catalyzed CNTs are shown in Figure 4.4. Virtually the same spectra were obtained from all sets of samples. The strong signal at about 1590 cm^{-1} is attributed to the G-band of tangential mode of graphene sheet while the peak at 1330 cm^{-1} is the D-band corresponding to the defects or limited dimensions of CNT crystal structure [113]. The D-band signal intensity is stronger than that of the G-band indicating the CNTs synthesized with Pd have significant lattice defects. In addition, the absence of any apparent second-order peaks indicates the low crystallinity of the CNT structure [113]. The radial breathing mode (RBM) peaks were not observed because no single-walled nanotubes were produced by this CVD method with Pd as the catalyst. The smallest MWCNT obtained was about 20nm in diameter per the SEM images. The Raman system used in this work operates in the backscattering geometry, a notch filter was installed to get rid of the scattering light, so all peaks with the Raman shift below

$50cm^{-1}$ were completely cut off. According to Bandow [114] et al., the RBM frequency can be calculated as $\omega_r = 223.75(cm^{-1}nm) / d\ (nm)$, where d is the diameter of the outmost graphene shell of the CNT. Therefore the RBM mode can not be seen if all the CNTs have the diameter more than 4~5nm. The intensity ratio of D-band to G-band varies between 1.25 to 1.5 among different samples, the difference is negligible, which indicates that all the CNTs grown in this work have similar defects.

The field emission behavior of the cathodes based on the as-grown CNTs is demonstrated in Fig. 4.5. From the emission current vs. the applied electrical field relationship, the turn-on field can be estimated, which in this work is defined as the applied field yielding an emission current density of $10\mu A/cm^2$. From the widely used Fowler-Nordheim equation [76], the emission current can be expressed as follows,

$$I = k_1 A \frac{F^2}{\Phi t^2(y)} \exp\left(-k_2 \frac{\Phi^{3/2} v(y)}{F}\right),$$

where $k_1 = 1.54 \times 10^{-6}$ $AeVV^{-2}$ and $k_2 = 6.83 \times 10^7$ $eV^{-3/2}Vcm^{-1}$, A is the emission area, $F=\beta E$ is the local electric field, $E=V/d$ is the applied anode voltage divided by the distance between the anode and the cathode, Φ is the work function, $t^2(y)$ and $v(y)$ are the electric field dependent elliptical functions where y is the image charge lowering contribution to Φ. $t^2(y)$ and $v(y)$ are usually taken as unity to simplify the calculations. Therefore, the slopes of the F-N plots (Fig. 4.6) can be written as $S=-k_2 d\ \Phi^{3/2}/\beta$, or, the field enhancement factor $\beta = -k_2 d\ \Phi^{3/2}/ S$. By setting Φ=5eV, β for each diode sample was estimated and summarized along with other parameters in Table 4.2. The samples (7a-7c) not pretreated in ammonia have a much higher turn-on field at about 6.5V/um, which we believe is due to the higher amount of amorphous carbon coating on the CNT surfaces. The data shows that among samples grown with long pretreatment time (10min, 9a-9c), the field emission performance is very similar (turn –on field ~2.5V/um, β~6200 to 7800) which are better than samples grown with shorter pretreatment time (1min, 8a-8c; with turn-on field ~4V/um and β~1500 to 3600) and samples without ammonia pretreatment (7a-7c; with turn-on field ~6.5V/um and β~800 to 2900). The better performance of the CNTs with longer pretreatment time and similarity in the emission characteristics is attributed to the better mixing of smaller nanotubes and diameter distributions within samples 9a-9c, where they have a dominant β in the field emission. The low turn-on field about 2.5V/um and high field enhancement factor around 6000~7000 are comparable to the results reported elsewhere [115-120].

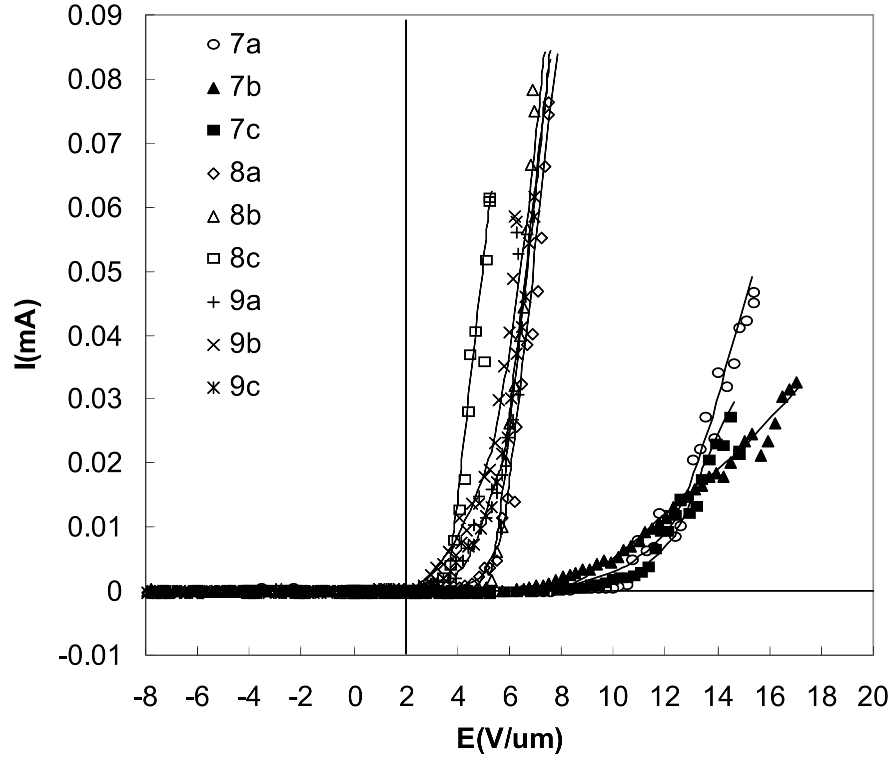

Fig. 4.5. I-E characteristics of as-grown CNTs: Letters a, b, and c denote the Pd film thickness of 10, 20, and 30nm, respectively. 7a-c for samples processed without NH_3 pretreatment but with NH_3 incorporation during synthesis. 8a-c for samples processed with 1 min NH_3 pretreatment and with NH_3 incorporation during synthesis. 9a-c for samples processed with 10 min NH_3 pretreatment and with NH_3 incorporation during synthesis.

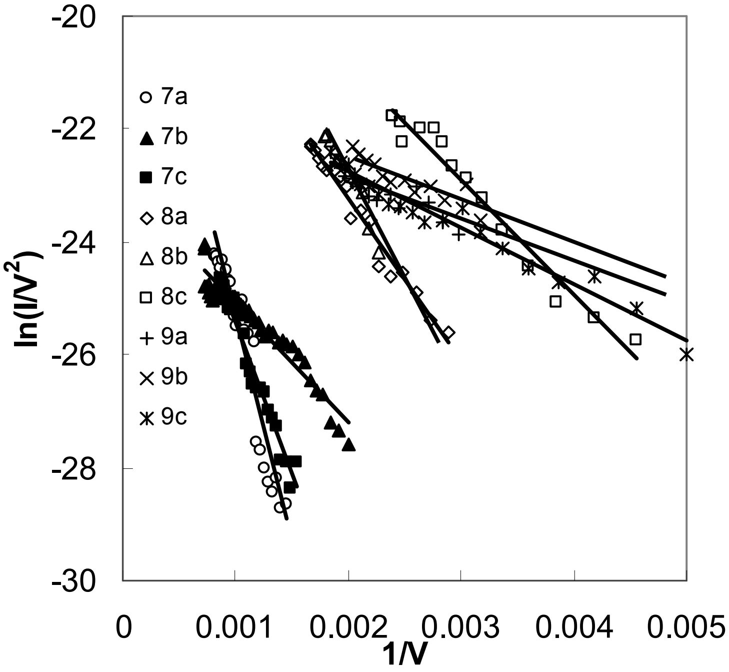

Fig. 4.6. Corresponding F-N plots of Fig. 4.5.

Table 4.2. Experimental results of the effects of Pd catalyst thickness and NH_3 pretreatment time on the density and diameter of as grown CNTs and turn-on field and field enhancement factor (β) of the CNT cathodes.

Sample #	Pd thickness, nm	NH3 pretreatment time, min	Average CNT diameter, nm	Number of CNTs per um^2	Turn-on field, V/um	Calculated β
7a	10	0	40-60	20-25	6.5	800
7b	20	0	80-100	10-12	6.5	2900
7c	30	0	100-120	1-2	6.5	1000
8a	10	1	30-50	20-25	4.0	1900
8b	20	1	40-60	12-15	4.0	1500
8c	30	1	45-65	9-12	2.7	3600
9a	10	10	20-40[a]	40-50	2.5	7800
9b	20	10	30-50[a]	20-30	2.5	7100
9c	30	10	40-60[a]	30-40	2.5	6200

[a] The as grown CNTs also contain some very small nanotubes with diameter less than 20 nm.

CNT Field Emitters by Thermal CVD at Atmospheric Pressure with Nickel as Catalyst

The effects of Ni catalyst thickness and ammonia flow rate on the catalyst particle size distribution are shown in the SEM photographs in Fig. 4.7. For all four sets of samples, Ni particle density, defined as number of particles per square micrometer, decreases as the thickness of initially deposited Ni film increases. Meanwhile, the average diameter of Ni particles increases. The incorporation of NH_3, on the other hand, has very little effect on the size distribution of Ni particles (different from the data on Pd catalyst), which is similar to the results reported elsewhere [121]. A summary of the statistical counts of Ni catalyst particles in different diameter ranges per square micrometer, for sample sets 1-4, is listed in Table 4.3. In fact, annealing in ammonia at 750°C has almost negligible influence on the average particle size and density, especially for Ni films with thicknesses of 6 and 9nm.

The CNT growth experimental results are shown in Fig. 4.8. As shown in the figure, there are almost no CNTs grown on samples 5a-5c, which are synthesized without the incorporation of NH_3 during synthesis phase. More interestingly, for all the 6nm Ni film samples (5a, 6a, 7a, and 8a), there are no CNTs grown when NH_3 flow rate was increased in the synthesis process. Considering the high density of small Ni particles (diameter <20nm) that form on these samples (Fig. 4.7 and Table 4.3), growth of denser CNT arrays than 9 and 11nm Ni film samples was expected. The reason for the adverse effect is due to poisoning of the Ni particles by impurities [63] contained in the gases and amorphous carbon during synthesis phase. Ni particle matrix with diameter <20nm has a smaller volume to surface area ratio than the larger particle matrices, therefore is more vulnerable to poisoning. As a result, no CNTs grew on Ni particles smaller than 20nm.

However, as the Ni particle size falls into favorable domains for CNTs growth, where the average particle diameter is in the range of 20-50nm (corresponding to 9nm and 11nm Ni film thicknesses), the effect of NH_3 on CNTs synthesis begins to be apparent. It can be seen from Fig. 4.8 that for samples 5(b,c), 6(b,c), 7(b,c), and 8(b,c) as the NH_3 flow rate increases from 0, 24, 32, and 43 sccm, respectively, resulted in none to sparing to spaghetti-like to vertically-aligned CNTs growth morphologies. This can be explained by the fact that NH_3 helps to reduce the interactions between amorphous carbon and catalyst sites thereby keeping more catalyst particles from being passivated [122-125]. This in turn results in significant increase in CNTs density as observed for these samples as the NH_3 flow rate is increased. While it is believed that ammonia keeps catalyst nanoparticles active for nucleation of graphite, the details of interactions between ammonia molecules/ions and catalyst particles remain unclear. We believe that ammonia acts as a moderate oxidizer which oxidizes (removes) amorphous carbon but leaves CNTs intact because CNTs have lower oxidation rate than the former.

Continuing, for samples 8(b,c), corresponding to the highest NH_3 flow rate, high density arrays of vertically aligned CNTs were formed. The mechanism of forming vertical alignment arises from van der Waals interaction between neighboring CNTs [63]. In other words, the limited spacing between closest nanotubes allows only one degree of freedom, they only grow straight upward. The higher the density of CNTs, the better the alignment results. As shown in Fig. 4.9, sample 8b has a higher density of nanotubes bundles than 8c, and they are much straighter than the latter. The diameter of CNTs on 8b and 8c ranges from 30 to 50nm and 40 to 60, respectively. Both the diameter and density of CNTs on these samples match the data of Ni particle experiments (Fig. 4.7, samples 4(b,c), and Table 4.4, 9 and 11nm at 43 sccm of NH_3) well.

By comparing sample sets 7 and 8 it is suggested that there exists a critical ammonia flow rate, or a threshold NH_3 / C_2H_2 flow rate ratio above which arrays of well aligned CNTs can be synthesized. Otherwise, randomly-oriented nanotubes of lower density are obtained. In this case, the critical NH_3 flow rate is ~ 43 sccm.

The Raman spectra of the Ni-catalyzed CNTs are shown in Figure 4.10. In fact, all the nanotube samples which are suitable for Raman spectroscopic measurements, namely, 6(b,c), 7(b,c), and 8(b,c), have demonstrated virtually the same spectroscopic characteristics, regardless of the density, diameters, and morphologies, i.e. whether vertically aligned or randomly oriented. The strong signal at about 1590 cm^{-1} is attributed to the G-band of tangential mode of the graphitic structure while the peak around 1330 cm^{-1} is the D-band corresponding to the defects or limited dimensions of CNT crystal structure [21]. The D-band signal intensity is stronger than that of the G-band indicating the CNTs synthesized by CVD at atmospheric pressure have some considerable lattice defects. In addition, the absence of any noticeable second-order peaks indicates the low crystallinity of the CNT structures [113]. The radial breathing mode (RBM) peaks were not observed because no single-walled nanotubes were produced by this CVD method with Ni as the catalyst. The smallest MWCNT obtained was about 30nm in diameter. The Raman spectrometer used to characterize the CNTs in this work is equipped with a notch filter [122] so the peaks with wave numbers less than 50cm^{-1} can not be detected. In other words, the radial breathing modes of CNTs with diameter more than 4-5nm are undetectable in this case.

The intensity ratio of D-band to G-band varies between 1.1 to 1.2 among different samples, the difference being negligible, which indicates that all the CNTs grown in this work have similar defects. The defect profile is common to CVD synthesized CNTs, most likely attributed to the relatively low growth temperature, which does not offer thermal energy sufficient for annealing CNTs into perfect crystalline structures [63], as compared to other methods such as arc discharge and laser ablation.

Six CNT cathodes with metal contact have been fabricated and tested for field emission, as depicted in Fig. 4.11. The CNTs were grown under the same process conditions as of samples 6(b,c), 7(b,c), and 8(b,c), respectively. The distance between anode and cathode was maintained at about 110 microns with a mica spacer. The tests were conducted at room temperature in a vacuum chamber of ~10^{-6} torr. The emission current versus applied electrical field measured for each cathode is shown in Fig. 4.12. The turn-on field in this work is defined as the applied field resulting in an emission current density of 10μA/cm^2.

A summary of CNTs critical processes and field emission parameters is shown in Table 4.4. Vertically aligned CNTs (8b and 8c) demonstrate lower turn-on field (3~3.5V/um) than their randomly oriented counterparts (6b, 6c, 7b, and 7c, 5~7V/um). This is attributed to the higher density of emission sources corresponding to the higher density of CNTs, and the higher aspect ratio resulted from the smaller CNT diameters. Sample 8b has the highest density and smallest diameters of CNTs among all six samples, and the CNTs are very well aligned (Fig. 4.9), which result in the highest field enhancement among the samples tested. The low turn-on field (3~3.5 V/um) of aligned CNTs is comparable to the results reported by other researchers [126-131].

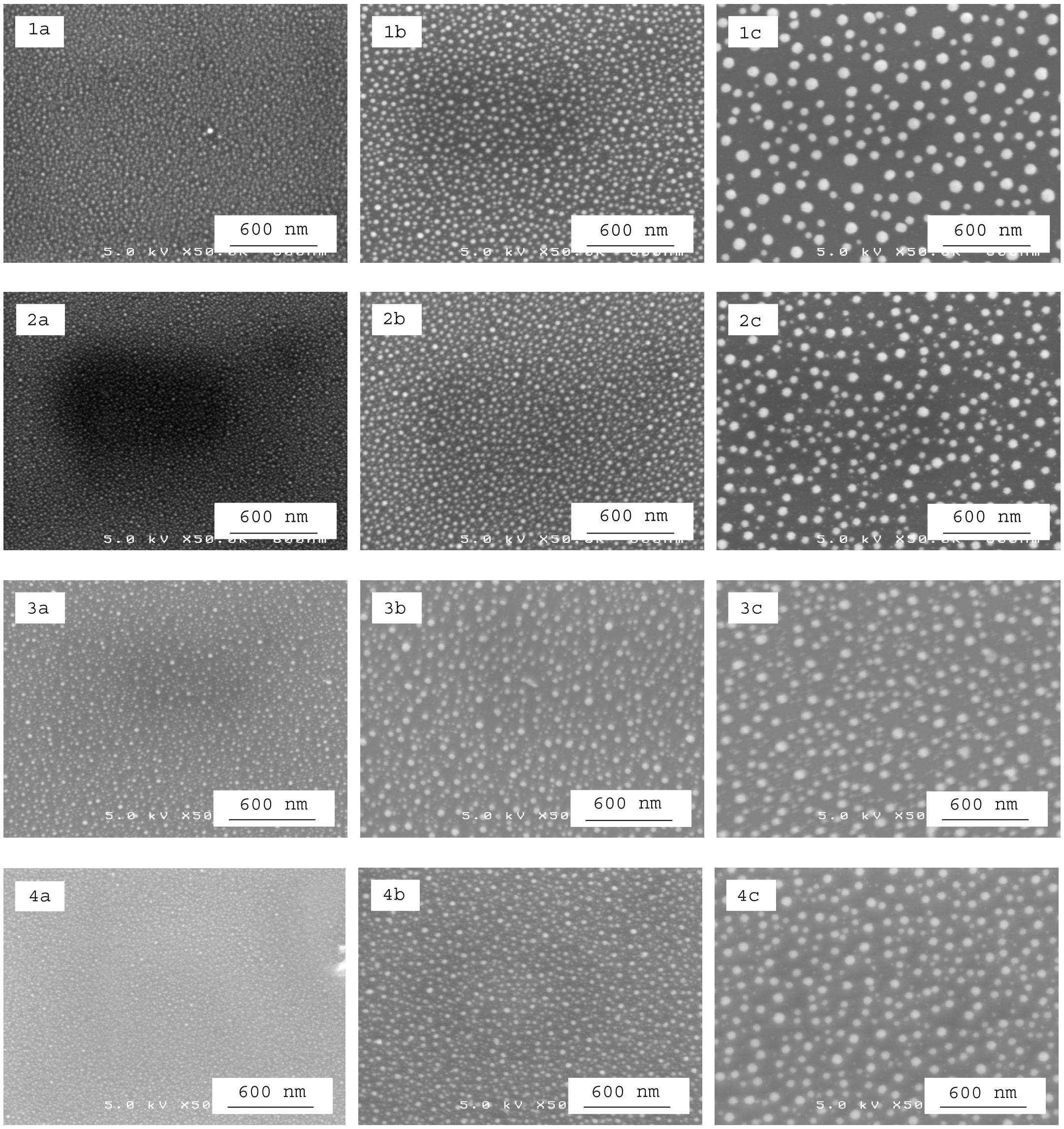

Fig. 4.7. Effects of initial catalyst film thickness and ammonia flow rate on the Ni particle size and density distribution. Four sets (1-4) of samples have undergone the tests. a, b, and c in each set denotes the Ni film thickness of 6, 9, and 11 nm, respectively. Samples 1a-1c were annealed in Ar/H_2 (4:1, 75sccm) for 30min, 2a-2c were annealed in Ar/H_2 (4:1, 75sccm) + NH_3 / N_2 (1:4, 24sccm) for 30min. 3a-3c and 4a-4c were tested under similar conditions as of 2a-2c, except that the NH_3 / N_2 flow rates were 32 and 43, respectively.

Table 4.3. Ni particle density and size distribution corresponding to Ni film thickness and ammonia flow rate.

	Ammonia flow rate, sccm											
	0			24			32			43		
Ni particle diameter, nm	Ni film thickness, nm											
	6	9	11	6	9	11	6	9	11	6	9	11
<20	~1000	~270		~1200	~300		~1200	~320		~1300	~350	6
20-40		~210			~100	6		~110	35		~150	30
40-60			15		90	60		80	27		21	26
60-80			20			14			27			28
80-100			12			3			9			
Ni particle density, um^{-2}	~1000	~480	47	~1200	~490	83	~1200	~510	98	~1300	~521	90
Average particle size, nm	<20	~20	~70	<20	~20	~50	<20	~20	~50	<20	~20	~50

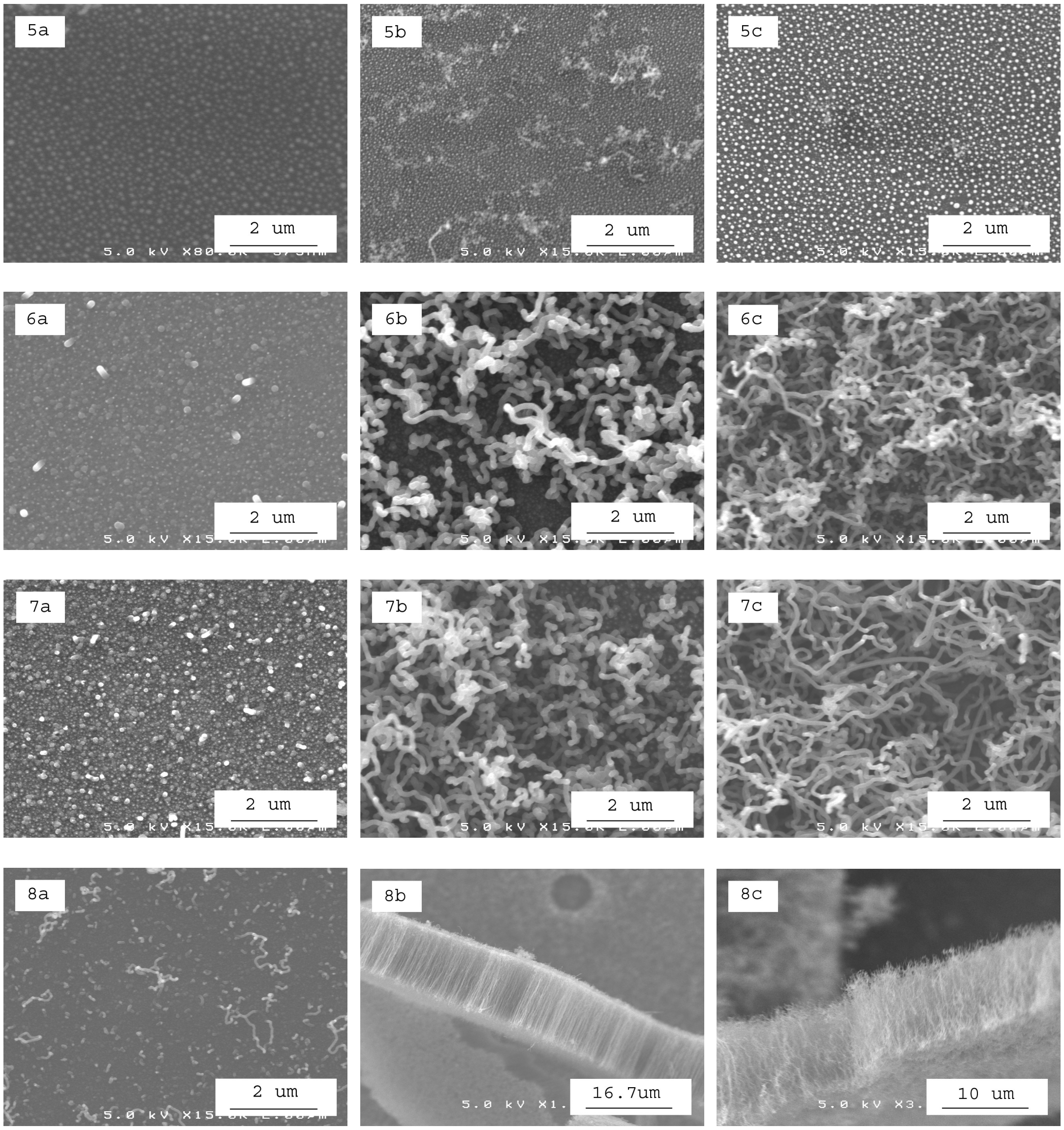

Fig. 4.8. Effects of catalyst film thickness and ammonia flow rate on the density, size, and morphology of as-grown CNTs. Samples 5a-5c were not exposed to ammonia and no significant CNT growth was observed because of the catalyst particle passivation caused by amorphous carbon coating. Ni particles size on samples 5a-8a was less than 20nm in diameter, which were easily poisoned and contaminated by impurities, as a result, CNT growth was not noticeable. Samples 6b, 6c, 7b, and 7c were tested under the critical ammonia to hydrocarbon flow rate ratio, therefore the as–grown CNTs were randomly oriented. At above the threshold NH_3/C_2H_2 ratio, arrays of vertically aligned CNTs were produced (samples 8b and 8c).

Table 4.4. Summary of CNTs critical processes and field emission parameters.

Sample number	Ni film thickness, nm	NH_3 flow rate, sccm	CNT diameter range, nm	CNT cathode turn-on field, V/um
6b	6	24	120-150	~7
6c	6	24	100-120	~6
7b	9	32	110-130	~7
7c	9	32	100-120	~5
8b	11	43	30-50	~3.2
8c	11	43	40-60	~3.5

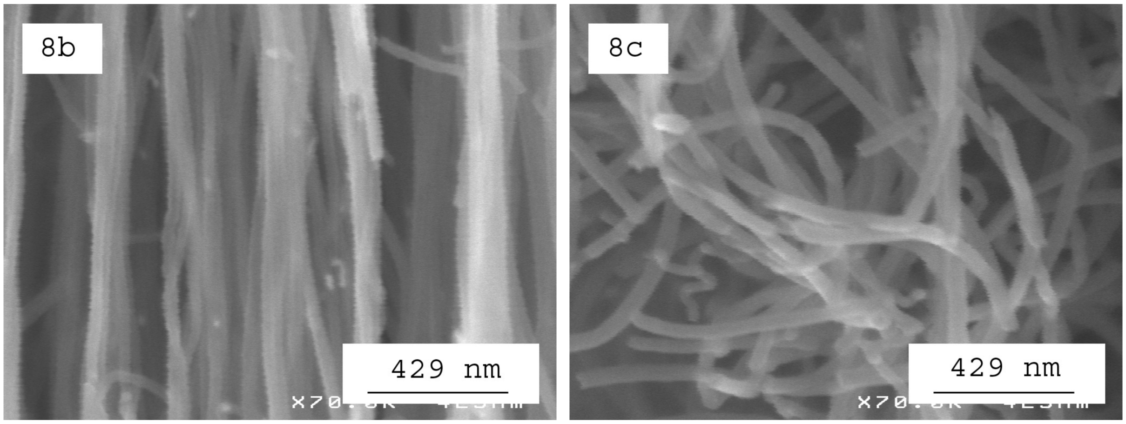

Fig. 4.9. High magnification SEM pictures of as-grown CNTs on samples 8b and 8c indicates the different degree of alignment between the two. Higher density of CNTs leads to a better alignment (8b) as the strong van der Waals interactions allow only one degree of freedom for CNT growth.

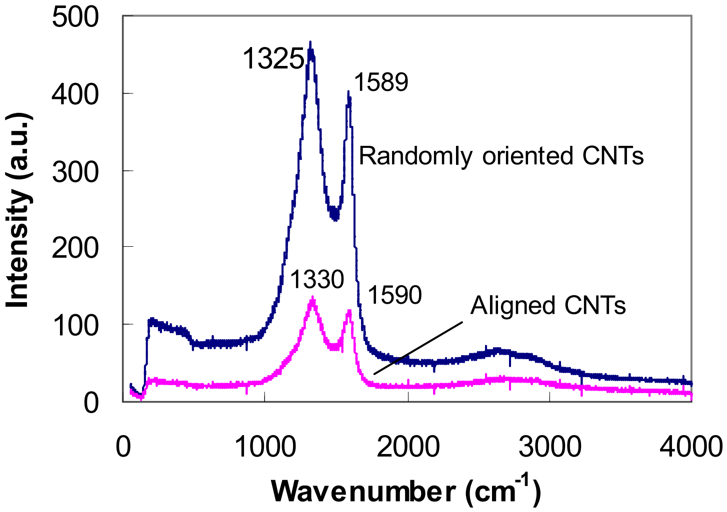

Fig. 4.10. Both randomly oriented and vertically aligned CNTs have virtually the same Raman spectra. The strong signal at about 1590 cm^{-1} is attributed to the G-band of tangential mode of the graphitic structure while the peak around 1330 cm^{-1} is the D-band corresponding to the defects or limited dimensions of CNT crystal structure. The D-band signal intensity is stronger than that of the G-band indicating the CNTs synthesized by CVD at atmospheric pressure have some considerable lattice defects.

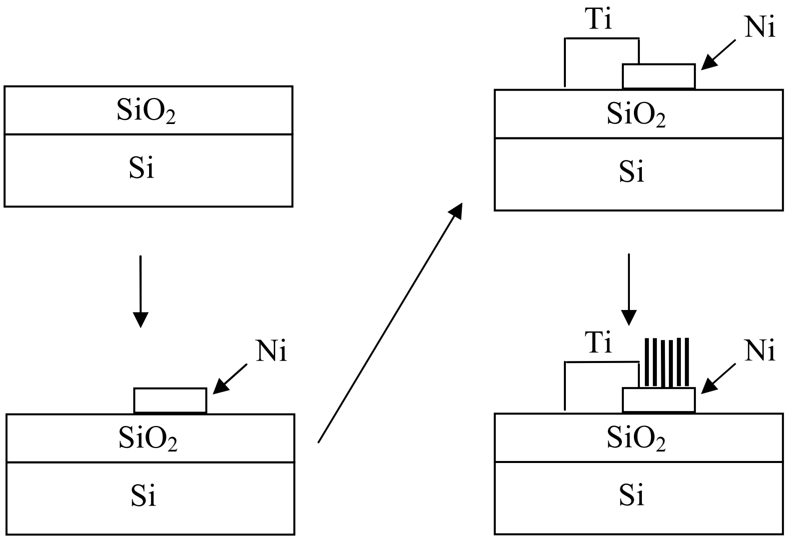

Fig. 4.11. Fabrication and field emission test of CNT cathodes. Ti was sputtered using a shadow mask as the cathode extension.

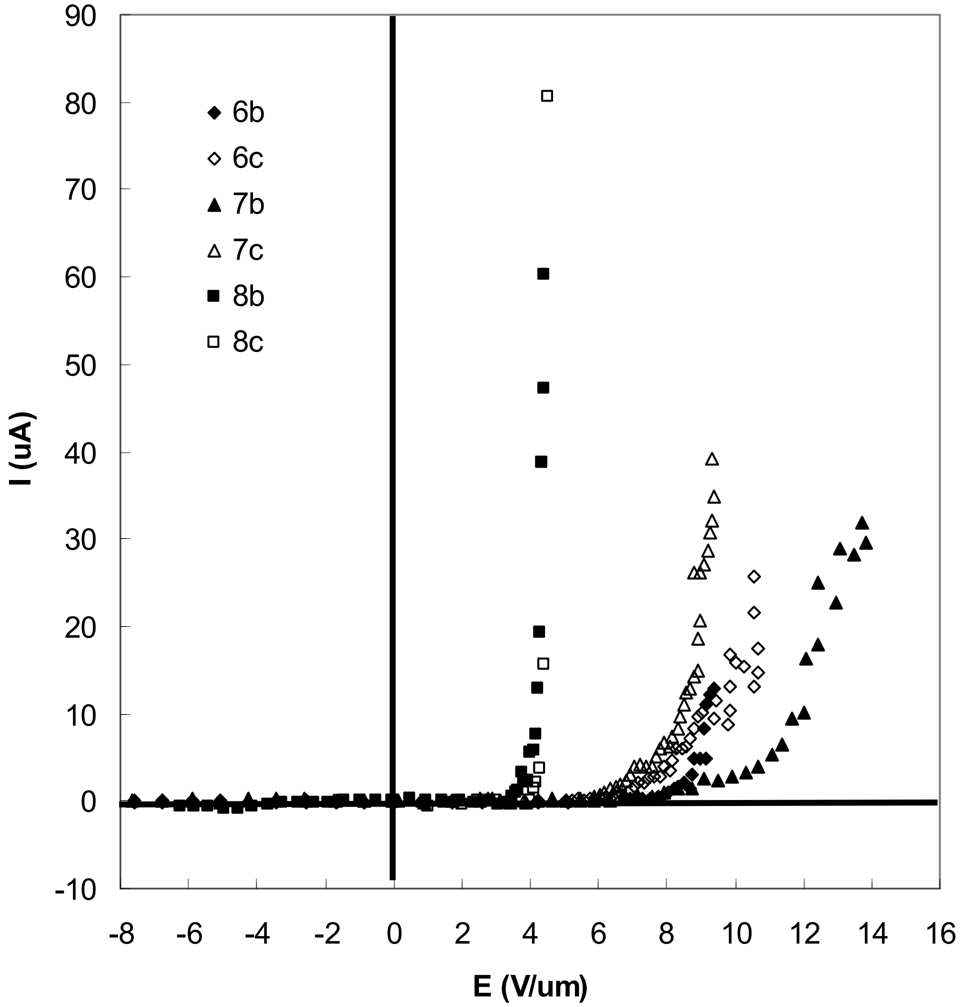

Fig. 4.12. I-E characteristics of as-grown CNT cathodes. Vertically aligned CNTs (8b and 8c) have lower turn-on fields (3.2 and 3.5 V/um, respectively) than the randomly oriented CNTs (5-7 V/um).

CNT Field Emitters by Thermal CVD at Atmospheric Pressure with Cobalt as Catalyst

The experimental procedure is described in Chapter III. Six sets of samples were prepared, three samples per set. These samples were labeled 1a-1c, 2a-2c, 3a-3c, 4a-4c, 5a-5c, and 6a-6c, where a, b, and c correspond to Co film thickness of 19, 28, and 31nm, respectively. Samples 1a-1c were annealed in argon and hydrogen, while 2a-2c were annealed in nitrogen-diluted ammonia at 16sccm. 3a-3c were annealed in the similar gas environment as 2a-2c but under a higher ammonia flow rate of 24sccm. These three sets of samples were used for Co particle test. Sample sets 4-6 were used for CNT synthesis test. For samples 4a-4c, no ammonia was involved before and during CNT growth, while 5a-5c and 6a-6c were both under ammonia treatment before and during CNT synthesis. The only difference was the flow rate of diluted ammonia gas, 16 and 24sccm respectively.

The SEM images of Co particle test samples (Fig. 4.13) suggest that for each group, Co particle density, defined as number of particles per unit area, decreases as the thickness of initially deposited Co film increases. In parallel, their average diameter increases. It is also noted that the flow rate of ammonia has significant influence on Co particle size and density. Samples in Group 1 have the lowest density and largest average diameters of particles among the three groups. While Group 3 with highest ammonia flow rate has the highest density and smallest size of Co particles.

According to the results of CNT growth experiments (Fig. 4.14), there are no CNTs grown on samples 4a-4c, which were processed without the incorporation of NH_3 during synthesis period. Samples 5a and 5b have randomly oriented CNTs while 5c and 6a-6c are vertically aligned CNTs with the incorporation of NH_3 during synthesis. It is also obvious that the densities of CNTs on samples 5a and 5b are lower than the rest. When growing vertically aligned CNTs by thermal CVD, high density of catalyst particles and incorporation of NH_3 reaction gas are determining factors. The results can be considered from that perspective.

Without the addition of NH_3 in the synthesis process, poisoning of the Co particles by processing gases impurities [63] and/or excess amorphous carbon deposition during the synthesis hamper the growth of CNTs as evidenced in samples 4a-4c, regardless of the Co particle size/density. Moreover it has been noted from Fig. 4.13 that the flow rate of ammonia has significant influence on Co particle size and density. As the Co particle size falls into the range of 30-60nm, i.e. the favorable domain for CNT growth, the effect of NH_3 on CNTs synthesis begins to be apparent. It can be seen from Fig. 4.14 that for samples 4a-4c, 5a-5c, and 6a-6c as the flow rate of NH_3/N_2 increased from 0, 16, to 24 sccm, respectively, resulted in none to spaghetti-like to vertically-aligned CNTs growth morphologies. This can be explained by the fact that NH_3 helps to reduce the interactions between amorphous carbon and Co catalyst sites thereby keeping more catalyst particles from being passivated [109-111, 122-124]. This in turn results in significant increase in CNTs density and better alignment as observed for these samples as the NH_3 flow rate is increased. While it is believed that ammonia keeps catalyst nanoparticles active for CNT nucleation, the details of interaction between ammonia molecules/ions and catalyst particles remain unclear. Perhaps ammonia acts as a moderate oxidizer, which oxidizes (removes) amorphous carbon at a much higher rate than it oxidizes CNTs.

By comparing sample groups 4, 5 and 6, it is suggested that there exists a critical ammonia flow rate, or a threshold NH_3/C_2H_2 flow rate ratio above which well aligned CNTs can be synthesized. Otherwise, randomly-oriented nanotubes of lower density are obtained. Based on the results in Fig. 4.14, this threshold NH_3/C_2H_2 flow rate ratio is 1.3~2, influence also by Co particle size/density.

The high magnification SEM images in Fig. 4.15 help compare the CNT density among samples with aligned nanotubes. It is clear that sample 6c has the highest density of CNTs in set 6. In addition, the CNT average diameter of 6c is slightly larger than 6a and 6b. In result, CNTs on sample 6c have better alignment than 6b, while 6b is better aligned than 6a. Sample 5c has slightly lower density and degree of alignment than 6c.

The CNTs structure is examined using Philips CM-20 TEM. The tubular multi-walled structure can be clearly seen from the TEM images in Fig. 4.16. The inter-wall spacing can be estimated at about 0.34 nm.

The Raman spectra of the Co-catalyzed CNTs are shown in Figure 4.17. In fact, all the nanotube samples have demonstrated virtually the same spectroscopic characteristics, regardless of the density, diameters, and morphologies, i.e. whether vertically aligned or randomly oriented. The strong signal at about 1590 cm^{-1} is attributed to the G-band of tangential mode of the graphitic structure while the peak around 1330 cm^{-1} is the D-band corresponding to the defects or limited dimensions of CNT crystal structure [113]. The D-band signal intensity is stronger than that of the G-band indicating the CNTs synthesized by CVD at atmospheric pressure have some considerable lattice defects. In addition, the absence of any noticeable second-order peaks indicates the low crystallinity of the CNT structures [113]. The radial breathing mode (RBM) peaks were not observed because no single-walled nanotubes were produced by this CVD method with Co as the catalyst. The smallest MWCNT obtained was about 30nm in diameter. The Raman spectrometer used to characterize the CNTs in this work is equipped with a notch filter [122] so the peaks with wave numbers less than $50cm^{-1}$ can not be detected. In other words, the radial breathing modes of CNTs with diameter more than 4-5nm [122] are undetectable in this case.

The intensity ratio of D-band to G-band varies between 1.1 to 1.2 among different samples, the difference being negligible. This indicates that all the CNTs grown in this work have similar defects. The defect profile is common to CVD synthesized CNTs, most likely attributed to the relatively low growth temperature, which does not offer thermal energy sufficient for annealing CNTs into more perfect crystalline structures [63], as compared to other methods such as arc discharge and laser ablation. A very weak second order peak corresponding to 2D is also observed at 2660 cm^{-1}.

Six CNT cathodes with metal (Ti) contact were fabricated and tested for field emission, as depicted in Fig. 4.18. The CNTs were grown under the same process conditions as samples 5a-5c, and 6a-6c, respectively. The distance between anode and cathode was maintained at about 110 microns with mica spacers. The tests were conducted at room temperature in a vacuum ($\sim 10^{-6}$ torr). The emission current versus electric field measured for each cathode is shown in Fig. 4.19. The turn-on field in this work is defined as the applied field resulting in an emission current density of $10 \mu A/cm^2$.

A summary of the CNTs field emission parameters as per their processing is shown in Table 4.5. The vertically aligned CNTs (6b and 6c) demonstrate low turn-on field (1.2~1.8V/um) and stable high emission current. This is attributed to the higher density of emission sources corresponding to the higher density of CNTs, and the higher aspect ratio resulting from the longer CNTs. It is noticed that sample 5b demonstrates low turn-on field comparable to the aligned CNT arrays. This is attributed to the relatively low CNT density of sample 5b, which is advantageous in terms of lowering the field screening effect. Its low CNT density, on the other hand, leads to limited emission current. The low turn-on field (<2V/um) of aligned CNTs is comparable to the results reported by other researchers [126-130].

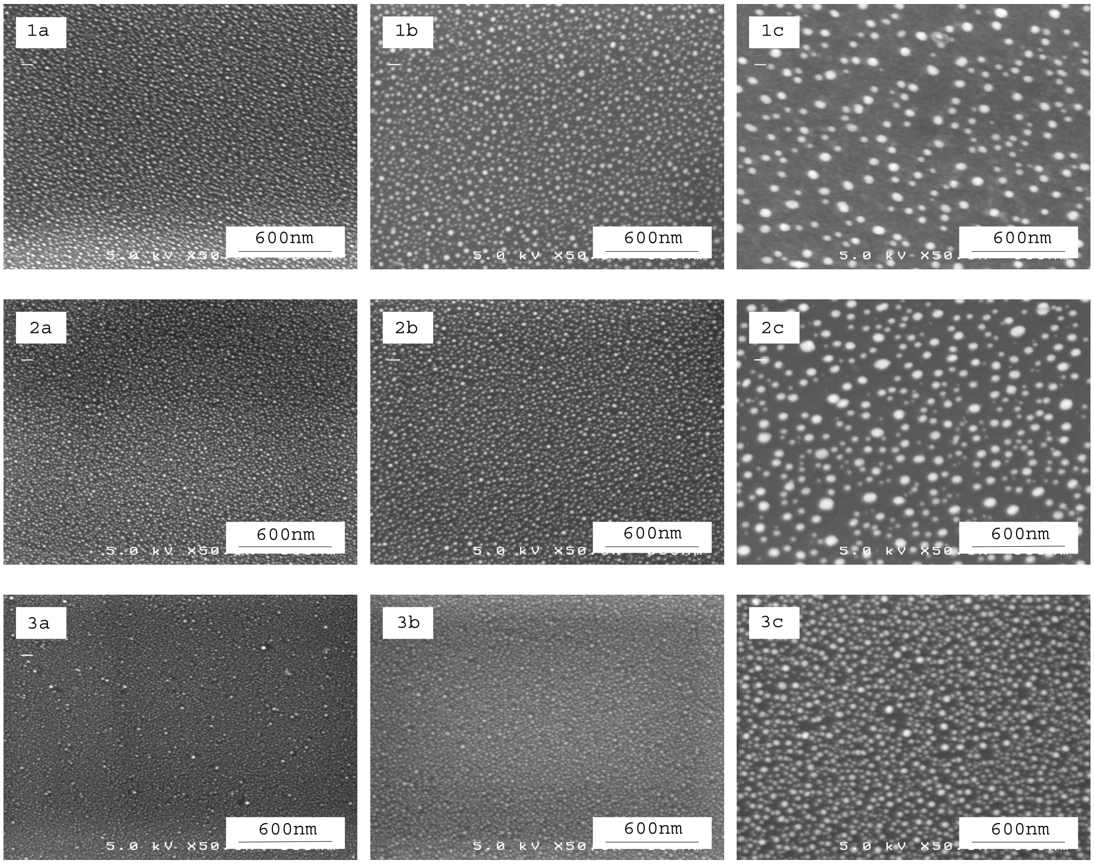

Fig. 4.13. Effects of initial catalyst film thickness and ammonia flow rate on the Co particle size and density distribution. Three sets (1-3) of samples have undergone the tests. The label a, b, and c in each set denotes the Co film thickness of 19, 28, and 31 nm, respectively. Samples 1a-1c were annealed in Ar/H_2 (4:1, 75sccm) for 30min, 2a-2c were annealed in Ar/H_2 (4:1, 75sccm) + NH_3 / N_2 (1:4, 16sccm) for 30min. 3a-3c were tested under similar conditions as of 2a-2c, except that the NH_3/N_2 flow rate was 24 sccm.

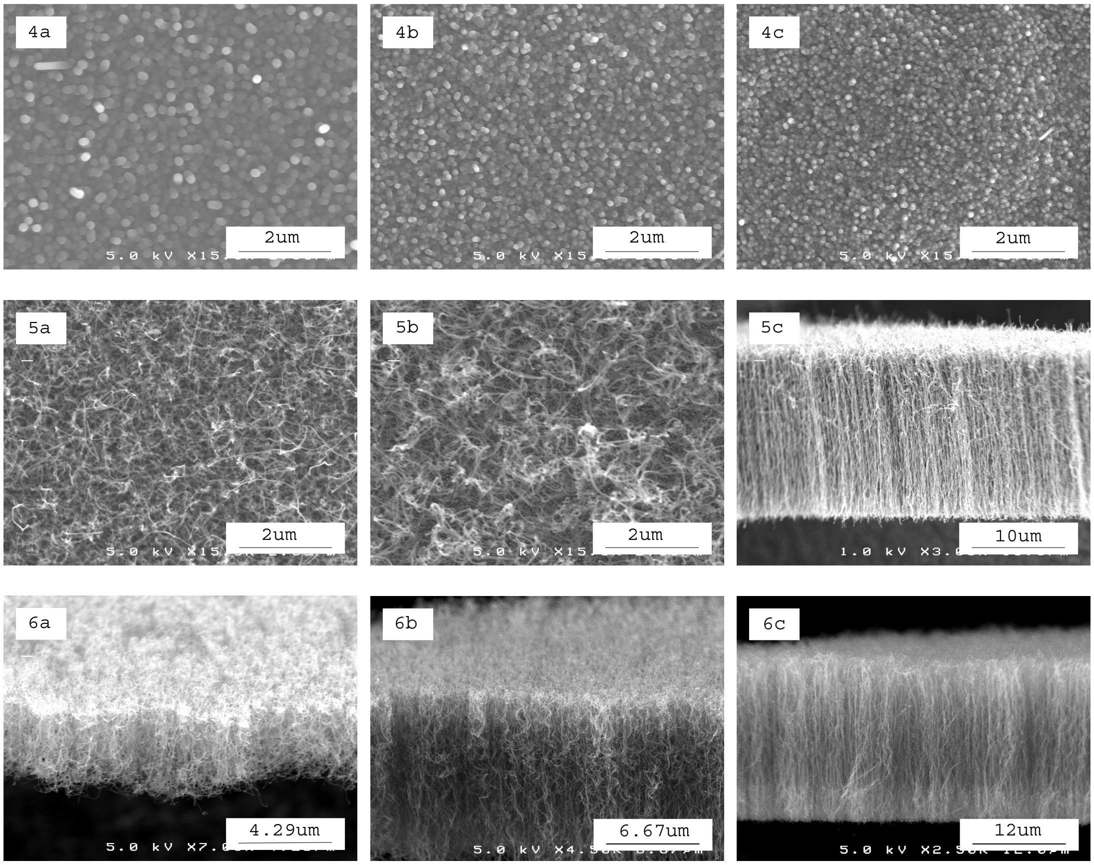

Fig. 4.14. Effects of catalyst film thickness and ammonia flow rate on the density, size, and morphology of as-grown CNTs. Samples 4a-4c were not exposed to ammonia and no CNT growth was observed. Samples 5a-5c and 6a-6c were processed with ammonia and the growth of CNTs was successful on these samples. The density of as-grown nanotubes increases with ammonia flow rate.

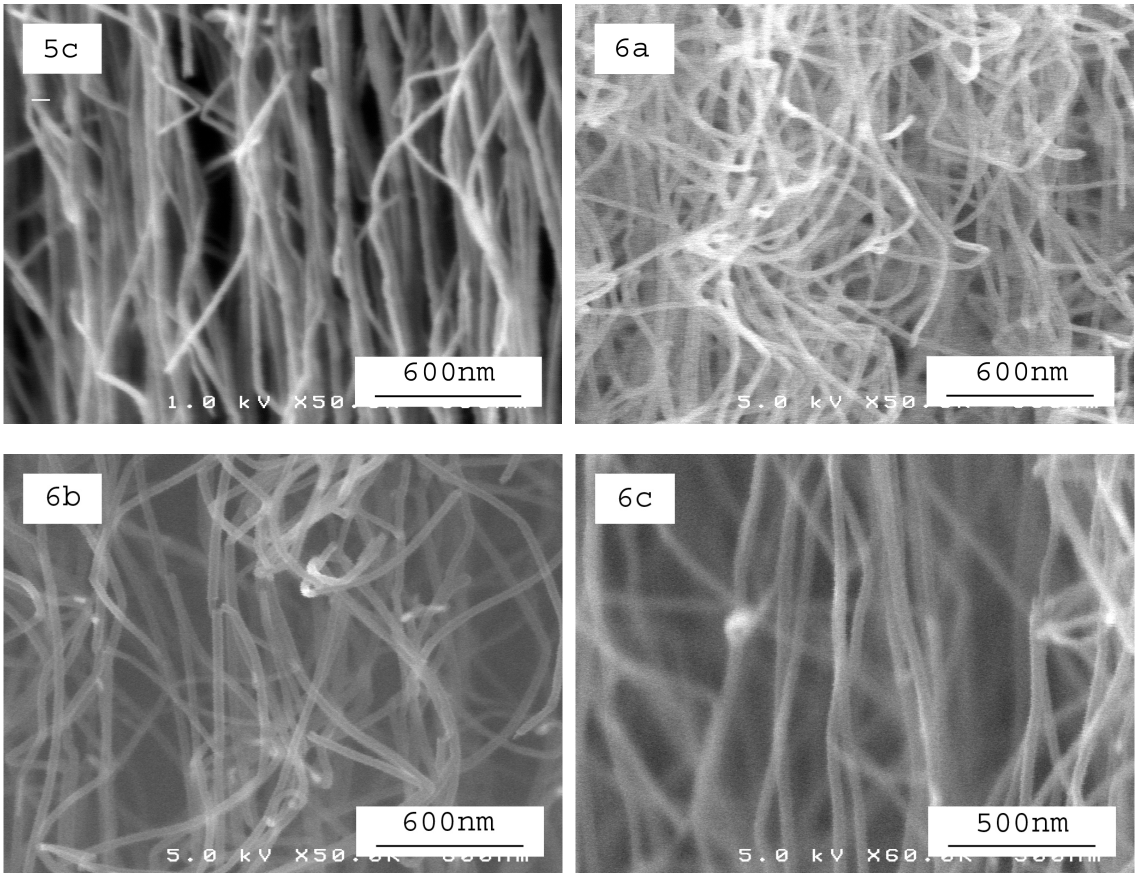

Fig. 4.15. High magnification SEM pictures of vertically aligned CNTs on samples 5c, 6a-6c indicating the different degree of tube alignment. Higher density of CNTs leads to a better alignment as the strong van der Waals interactions allow only one degree of freedom for CNT growth.

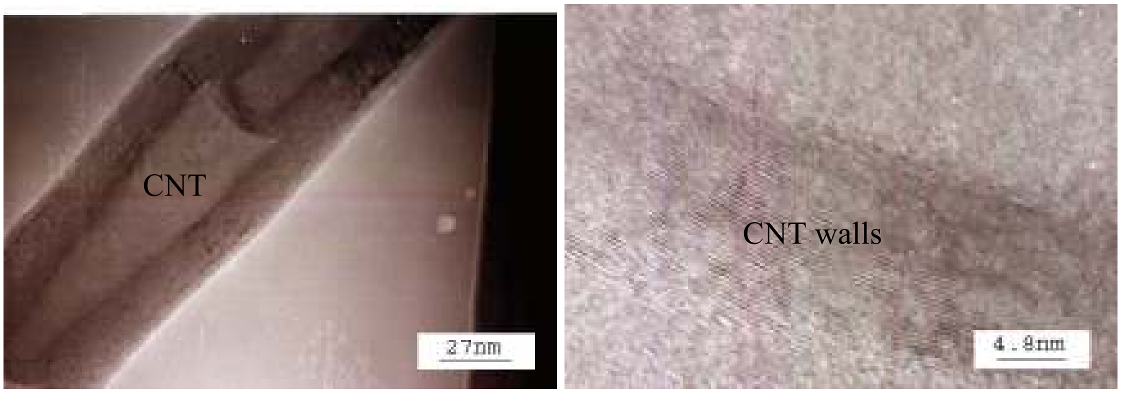

Fig. 4.16. TEM images confirm the tubular (left) multi-walled (right) structure of as-grown CNTs.

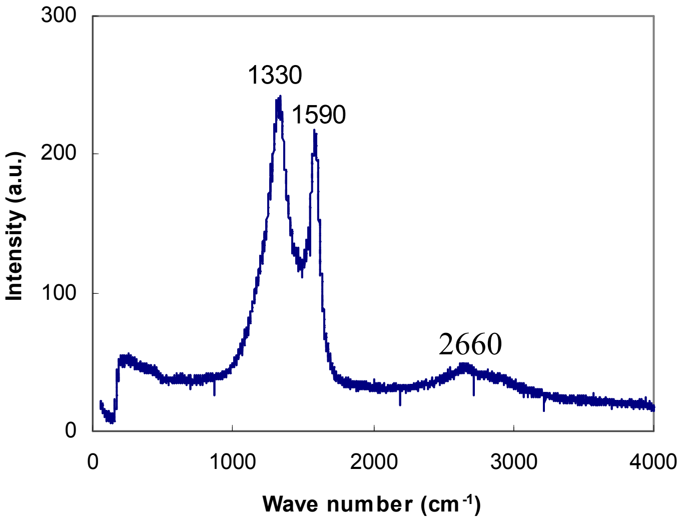

Fig. 4.17. Typical Raman spectra of the as grown CNTs. Both randomly oriented and vertically aligned CNTs have virtually the same Raman spectra. The strong signal at about 1590 cm^{-1} is attributed to the G-band of tangential mode of the graphitic structure while the peak around 1330 cm^{-1} is the D-band corresponding to the defects or limited dimensions of CNT crystal structure. The D-band signal intensity is stronger than that of the G-band indicating the CNTs synthesized by CVD at atmospheric pressure have some considerable lattice defects. A weak second order peak corresponding to 2D is observed at 2660 cm^{-1}.

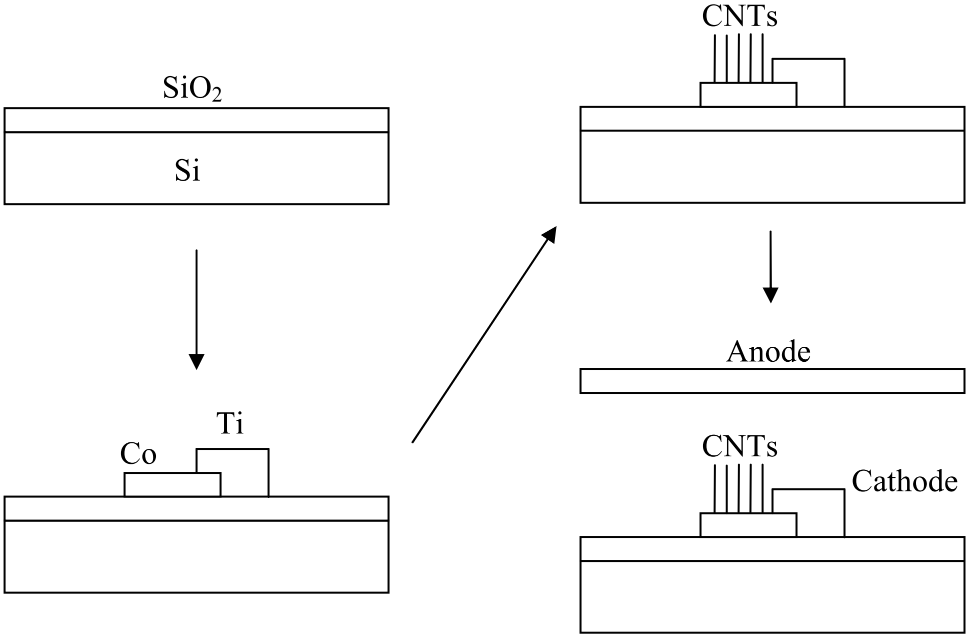

Fig. 4.18. Schematics of CNTs cathode fabrication and field emission test. Ti was sputtered using a shadow mask as the cathode extension prior to Co deposition.

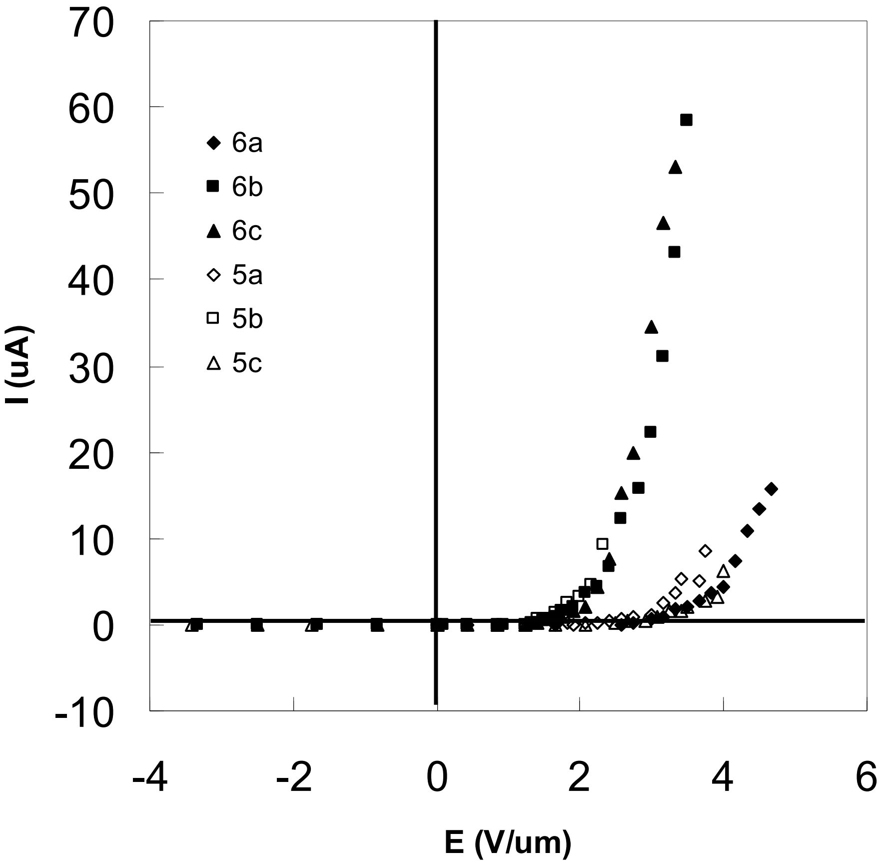

Fig. 4.19. Field Emission (I-E) characteristics of as-grown CNT cathodes. Vertically aligned CNTs (6b and 6c) show low turn-on fields (about 1.2-1.8V/um) and high current yield.

Table 4.5. Summary of CNTs process parameters and field emission characteristics.

Sample number	Co film thickness, nm	NH_3 flow rate, sccm	CNT diameter range, nm	CNT cathode turn-on field, V/um
5a	19	16	30-50	~2.2
5b	28	16	30-50	~1.3
5c	31	16	40-60	~2.8
6a	19	24	30-50	~2.5
6b	28	24	40-60	~1.2
6c	31	24	40-60	~1.8

Summary of Catalytic Performance of Palladium, Nickel, and Cobalt for Thermal CVD

The effect of Ar/H_2 annealing on catalyst is to form discrete catalyst particles from its original thin film morphology. This effect is similar among all three catalysts. The density of particles decreases with increased catalyst film thickness, while the average particle size increases at the same time. At comparable conditions, particle density of cobalt is higher than nickel and palladium.

Ammonia pretreatment increases catalyst particle density of Pd and Co, but has no effect on Ni particle density.

Ammonia is critical to CNT growth with all three catalysts. The main function of ammonia is to prevent the passivation of catalyst particles by etching away the amorphous carbon coating. With longer pretreatment time and/or higher flow rate of ammonia, higher density of CNTs is observed, which is necessary to form vertically-aligned CNT arrays. Well aligned CNT arrays were produced with Ni and Co but not with Pd, due to the low catalyst particle density and the corresponding low CNT density.

Although the morphology and size are different among CNTs produced by three different catalysts, their Raman spectra are very similar. This is attributed to the same method and temperature of synthesis. Pd-catalyzed CNTs have higher average diameter than the others because of the larger size of Pd particles. All three CNTs have amorphous carbon coating on them.

During thermal CVD processes, CNTs are synthesized by formation of graphitic structures at surfaces of catalyst particles through decomposition of carbon precursors. The form of produced graphitic structure also depends on the size of the catalyst particles. These catalyst particles are able to decompose hydrocarbons and to form metastable carbides. Also, carbon can diffuse through the catalyst particles and emerge from their surfaces at a fast rate, which is an essential property allowing ordered carbon structure to be formed through diffusion and precipitation. This property also determines that graphitic structures can only be formed near the catalyst surfaces.

If a bulk catalyst metal is used, carbon is dissolved in it and a solid solution is formed [131]. When the system is cooled down, carbon precipitates along the metal surface to form a continuous film of highly crystalline graphite where the basal planes of graphite are parallel to the substrate. This is why CNTs can not be produced on surfaces of thick pieces of catalyst metal. But if a thin film of catalyst is heated on a substrate, it will be dewetted into particles usually in the size smaller than tenths of a micrometer, and CNTs will be formed. Their diameters are about the same as the particles [131].

CNTs can form either through extrusion where nanotubes grow upward from catalyst particles which remain adhered to the substrate (referred to as base growth mode) or the catalyst particles may detach from the substrate and move at the top of the growing nanotubes (referred to as tip growth mode). Both modes are illustrated in Fig. 4.20. For the CNTs synthesized in this work with Pd, Ni, and Co, no catalyst particles were observed at the tips of CNTs, suggesting that base growth mode is dominant. In some cases, small fragments of catalyst particles may turn loose and detach from the substrate in the middle of CNT growth process. When this happens, tiny catalyst particles can be found trapped inside CNTs, as observed in Fig. 4.3.

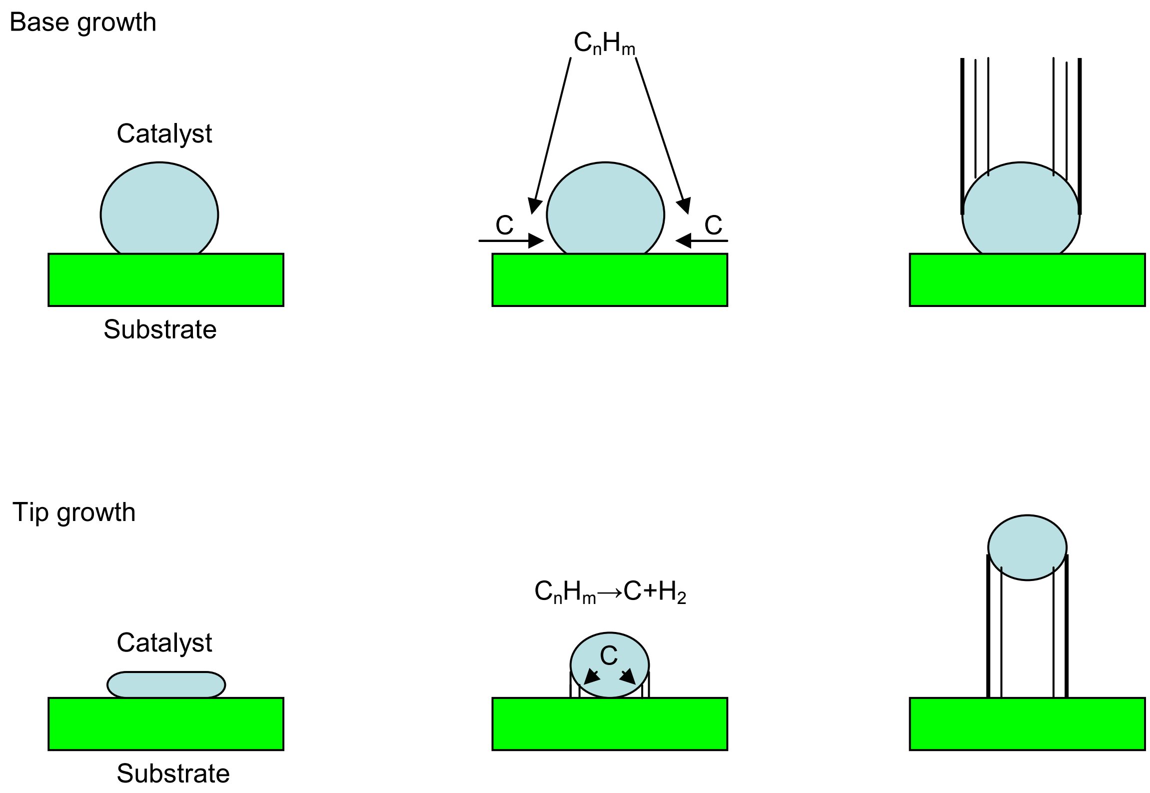

Fig. 4.20. Base and tip growth modes of CNTs [131].

CNT-Based Supercapacitors Fabricated by MPECVD

The performance of CNT-based supercapacitor depends on its morphology. The morphology of CNTs is influenced by the catalyst particle size and density [122, 132-134], which can be controlled by adjusting the Ni film thickness and the hydrogen plasma pretreatment as follows. Samples with nickel film thicknesses of 2, 3, 4, and 5 nm are separately heated in hydrogen ambient (~120 sccm) from room temperature to 650 °C at the ramp rate of ~ 50 °C/min. After the temperature is stabilized at 650 °C, they are treated with hydrogen plasma at 400 W for 1, 3, 5, and 7 minutes before cooling down to room temperature. Typical Ni particle size and density distribution are shown in Fig. 4.21. According to SEM images, the 3, 4, and 5 nm thick nickel films separate into well defined discrete catalyst particles, while the 2 nm thick catalyst film appears to have a carpet-like, semi-continuous morphology without noticeable particle formation, which is less favorable for CNT growth [108]. The catalyst particle density, defined as number of Ni particles per unit area of substrate, is estimated to be ~2200, 1700, and 1000 per square micrometer for 3, 4, and 5 nm samples, respectively. Table 4.6 is a summary of estimated particle diameters and densities.

For CNT synthesis, sixteen samples were prepared and allocated to a four by four test matrix per the as-deposited Ni catalyst thickness and hydrogen plasma pretreatment dwell time. The SEM images of these samples after CNT growth are shown in Fig. 4.22. Rows 1 through 4 (from top to bottom) correspond to the nickel catalyst film thickness of 2, 3, 4, and 5 nm, respectively, while columns one to four (from left to right)x correspond to hydrogen plasma pretreatment time of 1, 3, 5, and 7 minutes, accordingly. It is clear that samples with 2 nm catalyst film have significantly thinner carbon films than the rest and most of them are randomly oriented, diffuse nano-carbon structures, not vertically aligned CNTs, an exception being the three minute hydrogen plasma pretreated sample.

By comparing rows 2 through 4 in Fig. 4.22, it is obvious that samples with thinner nickel film have grown more vertically aligned CNTs. The driving force of CNT vertical growth is purported to come principally from strong Van Der Waals interactions between neighboring nanotubes [122, 132-134]. In general, decreased inter-tube spacing causes stronger Van Der Waals repelling forces that result in lower degree of freedom and higher degree of alignment [122, 132-134]. Thus a higher density of catalyst particles leads to shorter inter-tube spacing, therefore better alignment of CNTs for the 3 nm Ni catalyst samples.

Another interesting trend observed is that samples pretreated with hydrogen plasma for 3 minutes have more aligned CNTs than the others. As mentioned previously, a sequence of treatments was performed to control the catalyst particle size and density as demonstrated in Fig. 4.21 for the one-minute plasma pretreatment. Three, five, and seven minutes of hydrogen pretreatment was also performed. However, the size and distribution pattern of catalyst particles (not shown here) seem to be unchanged regardless of hydrogen plasma pretreatment time. This suggests that some other factor is responsible for the difference in CNT morphology between samples with the same Ni thickness but various pretreatment times. In a plasma ambient, as the bombardment by ions breaks the catalyst film into spherical particles, it also increases the temperature of such particles, i. e. the substrate temperature during plasma pretreatment may be higher than 650 °C. Therefore, prolonged exposure of nickel particles to higher temperature leads to higher risk of catalyst poisoning by impurities from hydrogen feedstock and CVD chamber walls [135]. As the result, catalyst particles after five and seven minute pretreatment become less active and the density/alignment of CNT arrays is relatively reduced.

From higher magnification SEM images of the as-grown CNTs, diameter, density (defined as number of CNTs per unit area of substrate), and height have been estimated for CNT films synthesized on 3, 4, and 5 nm Ni films. For example, Fig. 4.23 shows the CNT arrays of sample 4nm_3min, where the average number of nanotubes within 1um span is about 24-25. Therefore the average number of nanotubes in an area of 1um^2 is estimated as $(24.5)^2 \approx 600$. In addition, the total surface area of CNTs per square micrometer substrate area is estimated as:

$$A = \pi * d * h * n$$

where A is the total surface area of CNTs on one square micrometer of substrate area, d is the average diameter of nanotubes, h is the average height of CNT arrays, and n is the average number of CNTs per square micrometer of substrate area. For the sample of 4nm_3min, A is estimated as ~83um^2. This data is summarized in Table 4.7. CNT films grown on 2 nm Ni films are not included in the table because of the extremely random orientation of the nanotubes and the resulting difficulty in estimating the geometry.

The hollow tube structure of a typical as-grown CNT is readily seen even in low magnification TEM image (Fig. 4.24(a)) indicating the nanotubes are free of amorphous carbon coating as compared to thermal CVD-grown CNTs. Some catalyst particles are trapped at the ends of nanotubes, suggesting tip growth mode. The nanotube shown in high magnification TEM picture (Fig. 4.24(b)) has about 10 walls (shells) and the inter-wall spacing is ~ 0.34 nm.

The Raman spectrum (Fig. 4.25) of the as-grown CNT films shows two first-order bands and two second-order bands of significant intensity peaks. The strongest peak at 1327 cm^{-1} is obviously assigned to the D-band, indicating the presence of disorder or defects in the nanotube structures [136]. The second strongest band at 1587 cm^{-1} corresponds to G-band graphite mode [136]. The other bands located at 2654 and 2915 cm^{-1} are due to the second-order combinations of 2D and D + G, respectively [136]. In contrast, CNTs grown by thermal CVD do not have these additional peaks in their Raman spectra due to the amorphous carbon coating, as demonstrated in previous sections.

Cyclic voltammograms (Fig. 4.26) have been obtained from as-grown CNT films. The electrode active test area for each sample, as defined by the O-ring in the test setup, is about 38.5 mm^2. The four samples based on 2 nm nickel film (first row in Fig. 4.22) have poor quality CNT films and have been excluded from this test. The curves in Fig. 4.26A are measured at the same scan rate of 200mV/s to make meaningful comparison for four sets of hydrogen plasma pretreatment times on various catalyst thicknesses prior to CNT synthesis. The capacitance of each sample (see Fig. 4.26B) can be estimated from the cyclic voltammograms per [137]:

$$C=I/[(dv/dt)A]$$

where C is the electrode capacitance, I is the measured capacitive current, dv/dt is the scan rate, and A is the electrode area defined by the O-ring in the experimental setup.

As seen in Fig. 4.26B, it is apparent that for the given set of pretreatment times (1, 3, 5, and 7 min), the 3 nm samples consistently demonstrated the highest capacitance and the 5 nm samples the lowest. It is well known that the electrode capacitance is determined by the total effective surface area of the carbon nanotubes [138]. As previously discussed in Fig. 4.22 and table 4.7, better alignment yielded a higher density of nanotubes, i. e. more nanotubes per unit area. The 3 nm samples show better CNTs alignment for all pretreatment times compared to the other thicknesses; therefore the higher quantity of CNTs per unit area, which in turn generates higher capacitance. The 5 nm samples have the least aligned CNTs thus the lowest capacitance for the given set of catalyst pretreatment times, accordingly. Figure 4.27 shows capacitance-voltage curves for 3 sets of catalyst thicknesses subjected to different pretreatment times. It can be seen that the 3 min pretreated samples appear to have the highest capacitance for all the catalyst thicknesses investigated again due to better aligned CNT arrays as supported by Fig. 4.22 and Table 4.7. It is generally agreed that an ideal supercapacitor should be able to maintain a rectangular shaped I-V curve over a wide range of scan rate [139]. The CNT synthesized using a 3 nm thick and 3 min pretreated nickel catalyst has shown the highest capacitance in the test matrix thus was chosen for further testing. The results in Fig. 4.28 indicate that a nearly rectangular shaped I-V curve is maintained while the scan rate is varied from 10 to 1000mV/s. Moreover, the square loop I-V curves infer that fast charging-discharging behavior can be expected from this system. The uniform and dense distribution of the vertical aligned CNTs provides optimum surface morphology for near ideal capacitive behavior over a wide scan rate. The direct synthesis of CNTs on silicon substrates allows dense dispersion of vertically aligned CNTs and also minimizes the internal resistance during the charge transport.

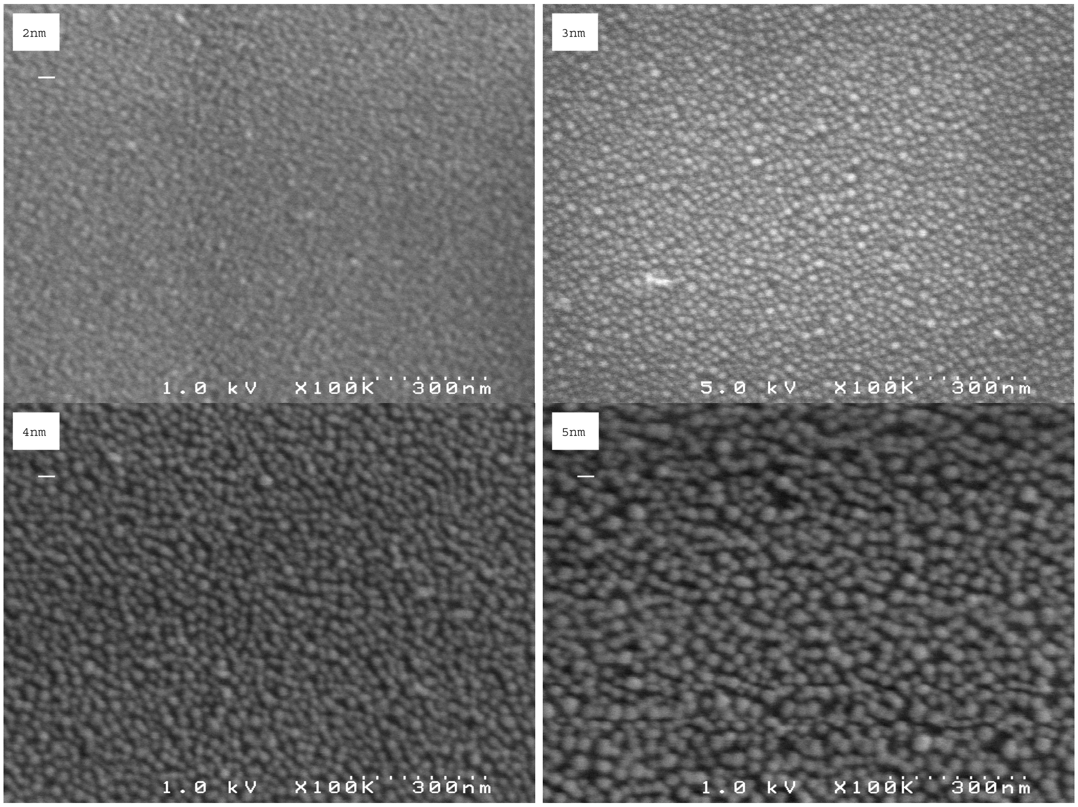

Fig. 4.21. SEM images of Ni particle size and density. Three-, four-, and five-nanometer nickel films separate into well defined discrete catalyst particles by hydrogen plasma, while two-nanometer catalyst film appears to have a carpet-like, semi-continuous morphology.

Table 4.6. Catalyst particle size and density of 3, 4, and 5 nm Ni films after 1 min pretreatment.

	Initial Ni film thickness		
	3 nm	4 nm	5 nm
Ni particle diameter, nm	10-25	15-35	20-45
Ni particle density, um^{-2}	~2200	~1700	~1000

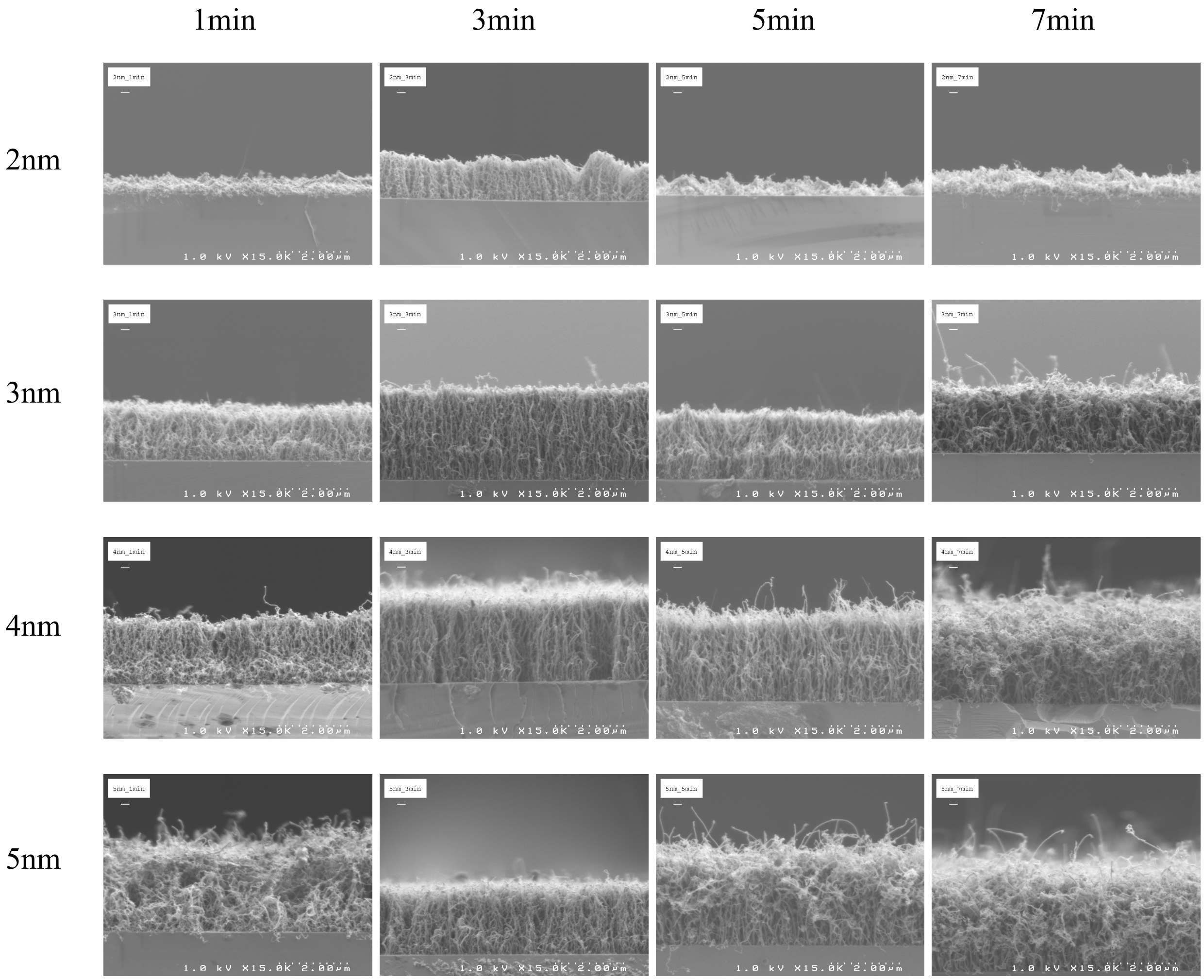

Fig. 4.22. SEM summary of CNT growth. Rows 1 through 4 from top to bottom correspond to the nickel catalyst film thickness of 2, 3, 4, and 5 nm, respectively, while columns one to four from left to right correspond to hydrogen plasma pretreatment time of 1, 3, 5, and 7 minutes.

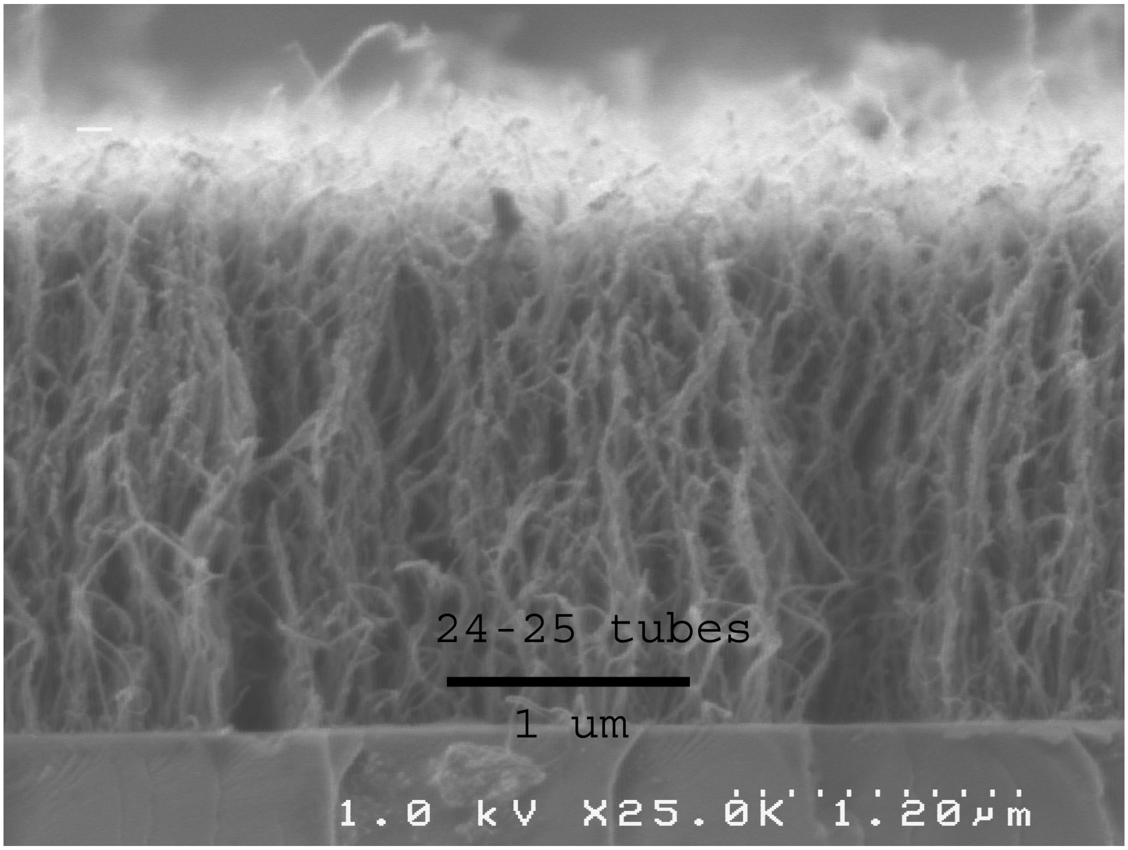

Fig. 4.23. The average number of nanotubes in 1um span is estimated at 24-25 for sample 4nm_3min.

Table 4.7. Diameter, density, height, and total surface area of CNT arrays.

Sample	CNT diameter, nm	CNT density, um^{-2}	Height of CNT arrays, um	Total surface area of CNTs per unit area of substrate, um^2
3nm_1min	10-30	780	1.6	78
3nm_3min	10-30	780	2.9	146
3nm_5min	10-30	780	2	98
3nm_7min	15-30	500	2	63
4nm_1min	15-30	600	1.8	68
4nm_3min	15-30	600	2.2	83
4nm_5min	15-35	530	2.4	80
4nm_7min	15-35	400	2	63
5nm_1min	20-30	300	2.4	57
5nm_3min	20-30	500	2	79
5nm_5min	20-40	250	2.7	64
5nm_7min	20-40	330	2	62

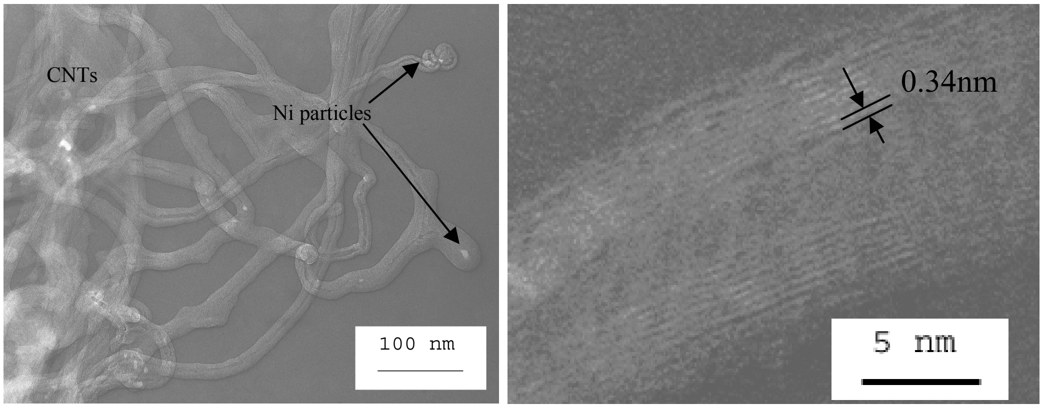

Fig. 4.24. The hollow tube structure of as-grown CNTs is readily seen even in low magnification TEM image (a). Some catalyst particles are trapped at the ends of nanotubes, suggesting tip growth mode. The nanotube shown in high magnification TEM picture (b) has about 10 walls and the inter-wall spacing is ~ 0.34 nm.

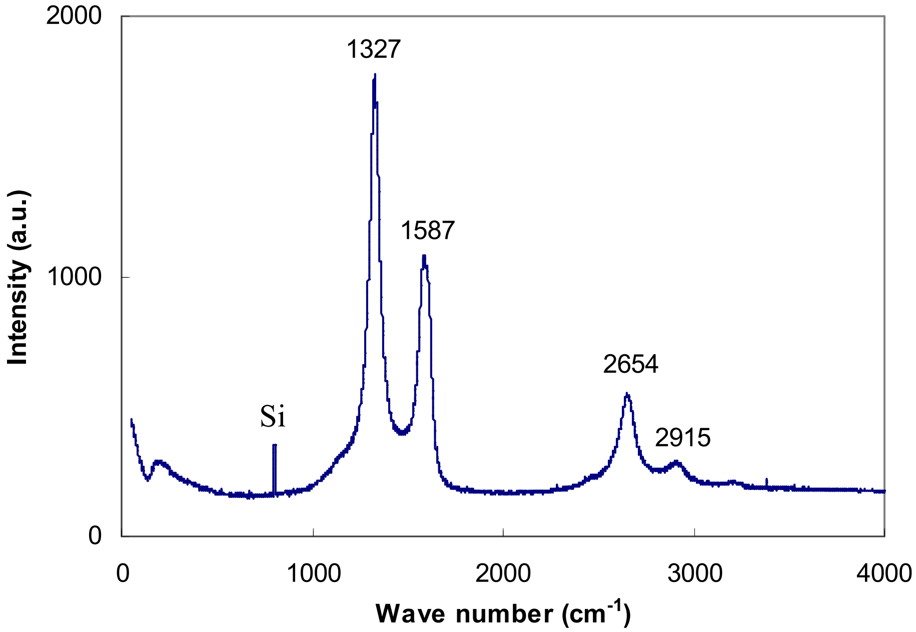

Fig. 4.25. Raman spectrum of as-grown CNT thin films. The strongest peak at 1327 cm^{-1} is obviously assigned to the D-band indicating the presence of disorder or defects in the nanotube structures. The second strongest band at 1587 cm^{-1} corresponds to G-band graphite mode. The other bands located at 2654 and 2915 cm^{-1} are due to the second-order combinations of 2D and D + G, respectively.

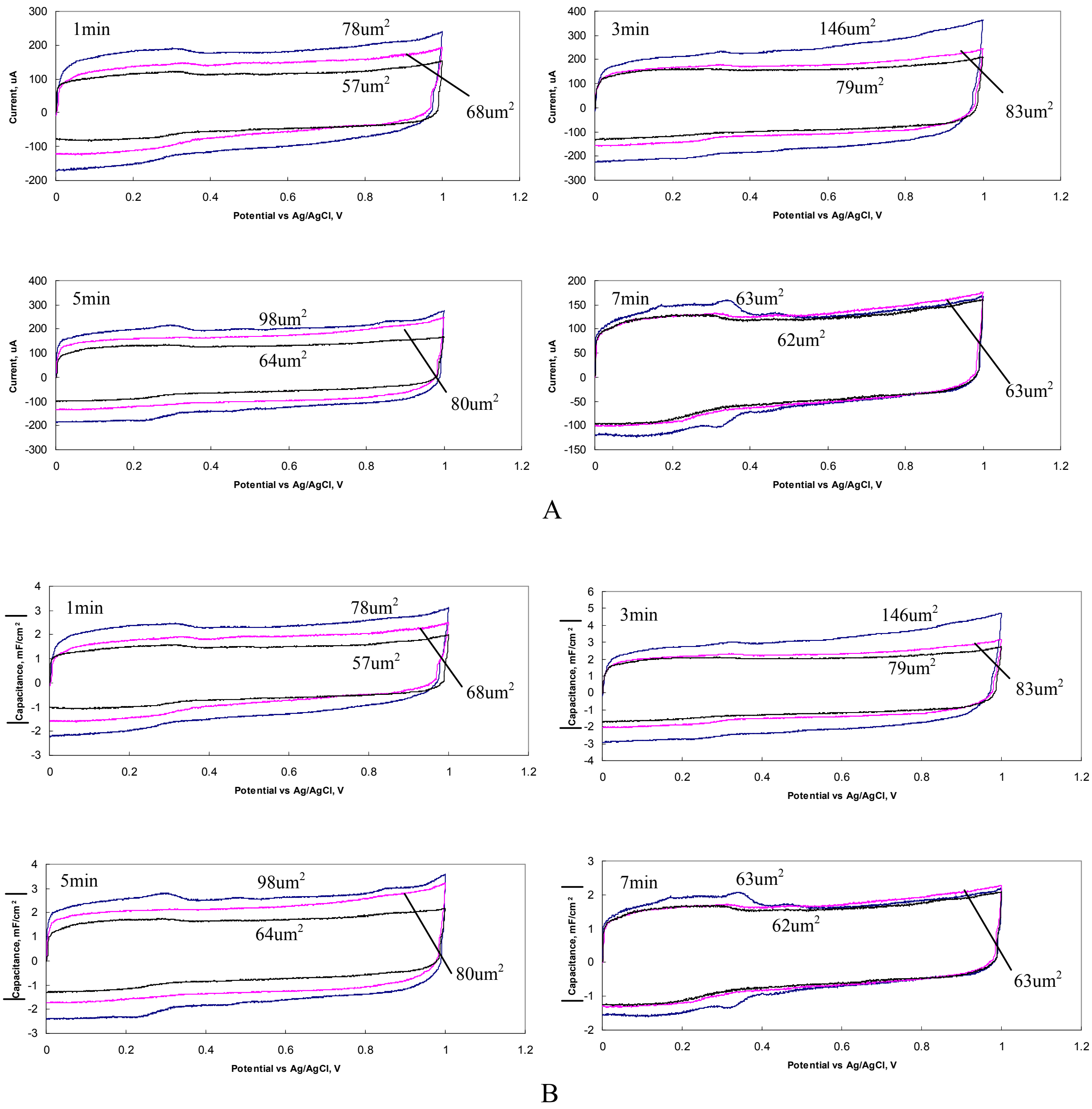

Fig. 4.26. (A) Cyclic voltammograms of as-grown CNT electrodes for four sets of hydrogen plasma pretreatment times on various catalyst thicknesses prior to CNT synthesis. For the same pretreatment time, 3 nm samples consistently demonstrate the highest capacitance and 5 nm samples the lowest. Capacitance value is higher on sample with higher surface area of CNTs, and the estimated surface area per square micron substrate is marked to each corresponding curve. (B) Same data with current converted to capacitance per unit area (mF/cm^2).

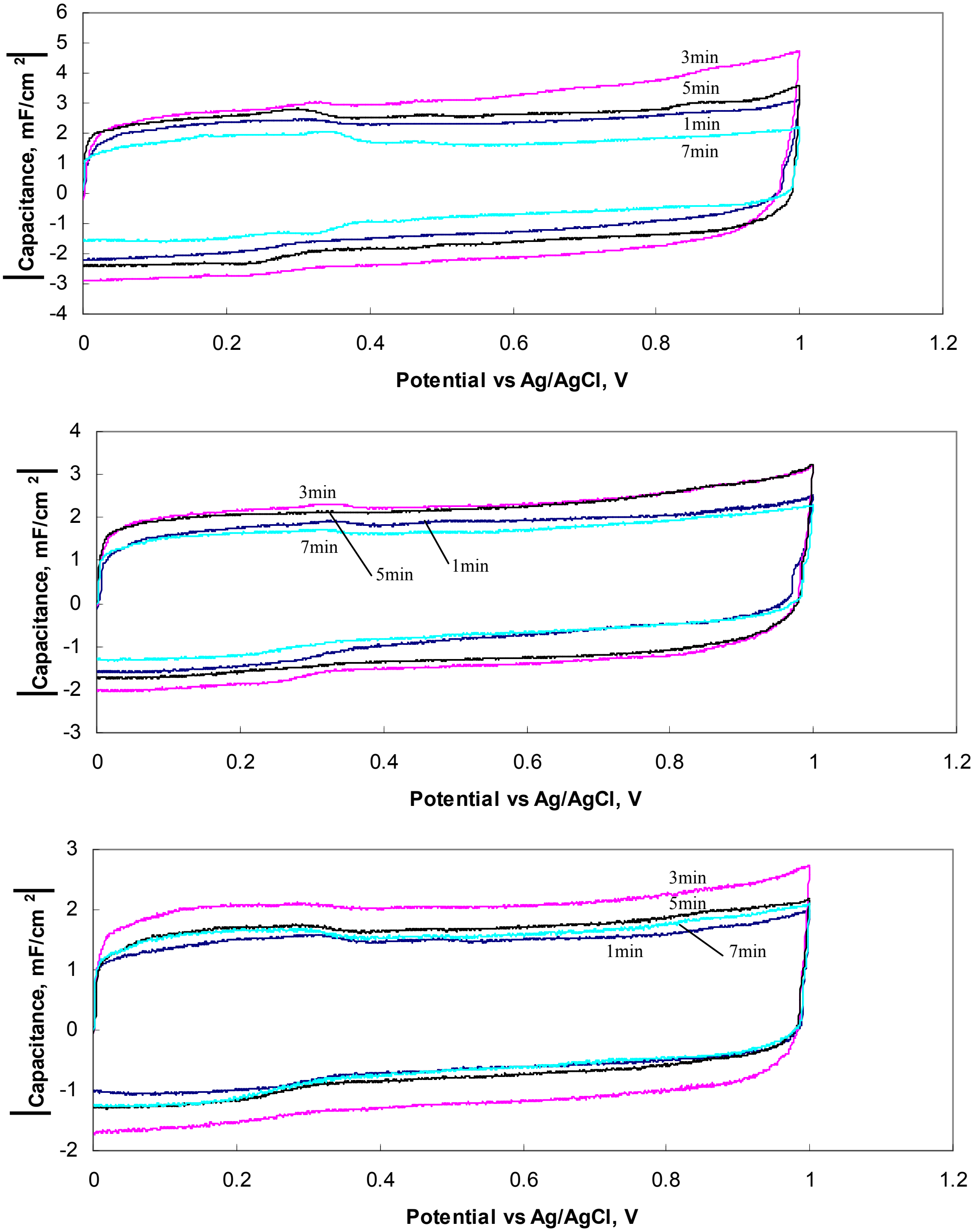

Fig. 4.27. Capacitance-voltammograms of as-grown CNT electrodes for 3 sets of catalyst thicknesses subjected to different pretreatment times. The three minute pretreatment samples have the highest capacitance for all the catalyst thicknesses investigated.

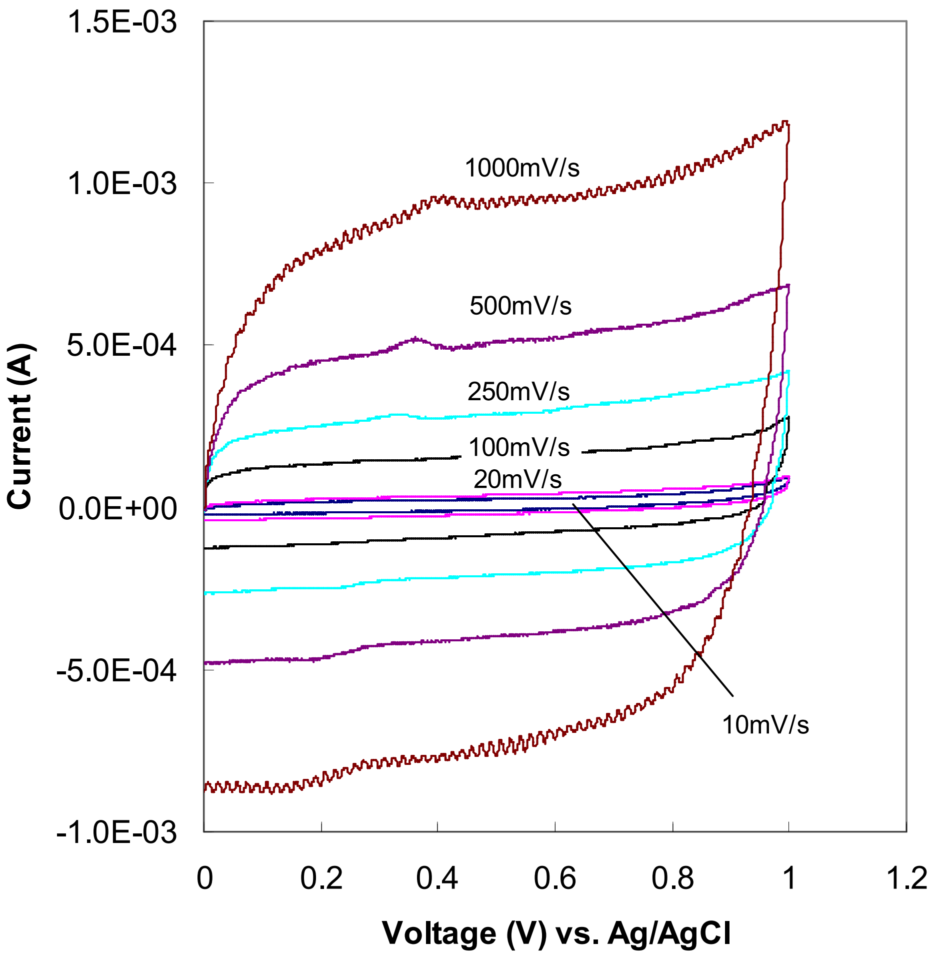

Fig. 4.28. Cyclic voltammograms of CNT electrode based on 3 nm Ni film with three minutes of pretreatment. Nearly rectangular shaped I-V curve is maintained while the scan rate is varied from 10 to 1000mV/s.

Supercapacitor Electrodes Based on Manganese Dioxide Coated CNT Thin Film

Supercapacitors based on well-aligned CNT arrays demonstrated consistent capacitive behavior as discussed in previous section. However, electric charges in this case are stored only in the double layers located at electrolyte-electrode interfaces and the maximum specific capacitance can only reach 10-40F/g or 10-30uF/cm^2 [78].

Recently, there has been strong interest in utilizing transition metal oxides (TMOs) as electrode materials for supercapacitors. TMOs demonstrate capacitive behavior, referred to as pseudocapacitance, through faradaic redox reactions with electrolyte.

Contrary to electrochemical double layer capacitors where capacitance depends upon the material surface only, pseudocapacitance is generated by Faradaic charge transfer between electrolyte and bulk electrode. Therefore the specific capacitance can be much higher than that of double layer electrodes. In fact, pseudocapacitance of 100-400uF/cm^2 has been reported [78].

Ruthenium dioxide (RuO_2) has specific capacitance in the range of 720-780F/g and is considered the best pseudocapacitor known so far [78]. It also has high electronic conductivity which is critical for supercapacitor applications. The major drawbacks of this material are the extremely high cost and low availability which limit it to mostly military applications.

Manganese dioxide (MnO_2) on the other hand, is a very inexpensive material and readily available in large quantity. It has a theoretically estimated specific capacitance of about 1000F/g [78]. But in practice, the measured value can only reach 150 to 250F/g, mainly due to its poor electric conductivity. In other words, if an electrode is made of a bulk piece of MnO_2 then only its surface part is effective because of the difficulties in electric charge transfer between its core and surface.

The major motivation of this work is to combine the high pseudocapacitance of MnO_2 nanoparticles with the exceptional electric conductivity and huge surface area-to-mass-ratio of CNT arrays to achieve extraordinary capacitor performance.

In this work, a larger piece of silicon wafer (2.5cm by 2.5cm square) is cleaned in diluted HF/de-ionized water solution to remove the native silicon dioxide. Then the wafer is sputter-coated with a thin titanium buffer layer followed by a thin layer of nickel as catalyst. The wafer is then placed into the MPECVD machine to grow CNTs on it. The procedure of CNT growth is similar to the one described in previous sections. When CNT synthesis is done, the wafer is cut into four square pieces, roughly 1cm by 1cm each. Three of these samples are dripped with 5, 15, and 30 acetone/MnO_2 droplets, and then dried at room temperature.

The weight of MnO_2 contained in each acetone/MnO_2 droplet is determined using a quartz crystal microbalance as follows: The volume of 30 droplets of the liquid was measured and divided by 30 to calculate the volume of each droplet. To measure the volume of 30 droplets rather than only one droplet is to reduce the systematic error of measurement. So the volume of each droplet was determined to be 39.13uL. Then, a micropipette of analytical chemistry grade was used to extract 2uL of the suspension and put it on the center of the quartz crystal. When acetone dried out, only MnO_2 is left. The weight (Δm) of MnO_2 is then reflected by the difference in the vibration frequency (Δf) of the quartz crystal before and after the addition of MnO_2 as follows (Sauerbrey Equation):

$$\Delta m = \frac{\Delta f \bullet A}{-C_f}$$

where $C_f = 0.056$ Hz/ng/cm^2 is a constant, and $A = 0.3419$cm^2 is piezoelectrically active crystal area. Therefore the weight of MnO_2 in each droplet is calculated as 7.389ug for measured $\Delta f = -61.86$Hz.

The SEM pictures in Figure 4.29 demonstrate the morphology change of CNT/ MnO_2 composite with increased quantity of MnO_2 nanoparticles. Manganese dioxide nanoparticles of lower quantity can be fully absorbed into CNT arrays forming a rather unicorm composite (Figure 4.29B). With more drops of MnO_2/acetone suspension added, surplus MnO_2 nanoparticles are built up on top of CNT arrays (Figure 4.29C-D). The

TEM pictures (Figure 4.30) show a fragment of CNT/MnO_2 composite that is removed from the substrate with a razor blade. The high magnification TEM image shows the attachment of MnO_2 nanoparticles on or around a CNT surface. During TEM sample preparation, the removed CNT/MnO_2 composite is added into a vial filled with acetone and the vial is placed into an ultrasonic cleaner for a few minutes to ensure that large bundles of CNTs are separated into smaller ones for better TEM observation. Before ultrasonication, the CNT/MnO_2 composite appeared as precipitates at the bottom of the vial. After sonication the precipitates turned into smaller grains suspended in acetone. This CNT/MnO_2/acetone suspension is then dripped on to a TEM grid, dried, and observed on TEM. It must be pointed out that the TEM specimen preparation process involving ultrasonication inevitably results in the detaching of some of the MnO_2 nanoparticles from the CNTs.

To examine the effect of MnO_2 coating on the capacitance of CNT electrode, the 5, 15, and 30 droplet samples along with the MnO_2-free CNT sample are tested one by one, as working electrode in a standard three-electrode configuration with Ag/AgCl reference electrode and a platinum wire as counter electrode. The active area of working electrode confined by an O-ring in the test cell is ~50 mm^2. A 0.1M KCl aqueous solution is utilized as the electrolyte. For comparison of the four samples, the scan rate for cyclic voltammetry is set to 100mV/sec. Figure 4.31A indicates that all three MnO_2/CNT composite electrodes have significantly enhanced capacitance compared to the same CNT sample without MnO_2 while the overall capacitance is increased with the quantity of MnO_2 added. The corresponding capacitance values are also estimated as specific capacitance per unit area of substrate (F/cm^2) as $C=I/[(dv/dt)A]$ where I is the current, (dv/dt) is the scan rate and A is the active area of the electrode defined by the O-ring. And the converted capacitance curves are drawn in Figure 4.31B. Figure 4.31C shows that the prepared MnO_2/CNT composite electrode demonstrates high stability through a wide scanning rate range of 10-500mV/sec. Also, the nearly perfect symmetry of the curves proves the high reversibility of the capacitor.

Fig. 4.31A-B indicate a huge difference in capacitance between CNTs and CNT/MnO_2 composite. To investigate the capacitance contributed by MnO_2 only, an additional experiment is performed. Three pieces of n++ Si wafers, $1cm^2$ each, same as the ones used for CNT film deposition described above, are cleaned in diluted HF, rinsed and dried. 5, 15, and 30 droplets of MnO_2/acetone suspension are then added drop-wise on top of the wafers, respectively. After the acetone dries out, these samples are tested with cyclic voltammetry. The results are shown in Figure 4.32 along with the MnO_2-free CNT sample for comparison. Apparently, MnO_2 nanoparticles without CNT support do not show any pseudocapacitance behavior, regardless of the quantity applied. Their current is in the noise level, even far below that of as-grown CNT thin film. This is attributed to the poor electric conductivity of MnO_2. It is well-known and recognized that pure MnO_2, regardless of its form, has never shown good pseudocapacitance without the addition of conductive carbon material [140-141] because of the high resistivity of MnO_2.

Hence, we propose the following model to explain the observed capacitance enhancement in the CNT/MnO_2 electrode. In MnO_2/CNT composite (Fig. 4.33), the network structure formed by CNT arrays serves as a supporting matrix for MnO_2 nanoparticles. Each MnO_2 nanoparticle can be considered a tiny pseudocapacitor electrode and each individual nanotube acts as a current collector for MnO_2 nanoparticles surrounding it. In this system, the charge transfer occurs between CNTs and MnO_2 nanoparticles therefore is very efficient due to the exceptional electronic conductivity of CNTs. Vertical alignment of CNTs also improves the attachment of MnO_2 nanoparticles to CNT arrays. The direct growth of CNTs on conductive substrate helps to reduce contact resistance and ESR is significantly reduced and power is enhanced.

To examine the cyclic stability and further quantify the capacitance, galvanostatic charging-discharging tests have been performed on the above samples and the results are shown in Figure 4.34. Based on the charging-discharging cycle and current, the capacitace can be estimated for each sample as C = I*t/V where I is the charging current, t is the charging time for each cycle, and V is the cell voltage (set at 0.85V for all samples in this case). In Figure 4.34, A, B, and C correspond to MnO_2-free CNT, 5-droplets-MnO_2-on-CNT, and 15-droplets-MnO_2-on-CNT samples, respectively, under the same charging-discharging current of 30uA. The charging time of each cycle for the above samples is 2.67s, 97.22s, and 156.25s, respectively. And the calculated capacitance is 94.13uF, 3431.4uF, and 5514.71uF, accordingly. The 5-droplets-MnO_2-on-CNT and 15-droplets-MnO_2-on-CNT samples have capacitances 36 and 58 times the MnO_2-free CNT sample. Figure 4.34D and 4.34E correspond to 15-droplets-MnO_2-on-CNT and 30-droplets-MnO_2-on-CNT samples under the charging-discharging current of 120uA. By comparing these two in the same way described above, it can be estimated that 30-droplets-MnO_2-on-CNT sample has a capacitance of 30000uF (270F/g) which is 8.5 times higher than 15-droplets-MnO_2-on-CNT sample, or over 400 times that of MnO_2-free CNT sample. Figure 4.34F is the charging-discharging behavior of 30-droplets-

MnO_2-on-CNT sample at charging/discharging current of 1.92mA, or 17.32 A/g, which is a high current compared to the results reported elsewhere [142].

Figure 4.35A and B are the XPS surveys obtained from MnO_2-free CNT and 5-droplets-MnO_2-on-CNT samples, respectively. It is obvious that the sample with MnO_2 has an enhanced O1s peak and two extra Mn2p peaks compared to the MnO_2-free CNT sample. Figure 4.35C is an enlarged view of the two Mn2p peaks. Their positions are located at 654.0eV and 642.3eV, corresponding to Mn 2p1/2 and Mn 2p3/2 of β-MnO_2, respectively [143], see Table 4.8. The same MnO_2/CNT composite sample was then tested on 100 cycles of cyclic voltammetry in 0.1M KCl solution at the scan rate of 100mV/sec. And the XPS binding energies of Mn 2p1/2 and Mn 2p3/2 were found unchanged (Figure 4.35D). XPS data confirms the β-MnO_2 structure and suggests that the MnO_2 nanoparticles are chemically stable.

In summary, a novel procedure has been utilized to fabricate MnO_2/CNT composite electrode. The electrodes demonstrate outstanding capacitance behavior with power density more than 400 times of as-grown CNT thin film and excellent long-term chemical stability. High specific capacitance of 270F/g and charging curent of 17A/g have been observed. In addition, both manganese dioxide nanoparticles and potassium cloride electrolyte utilized in this work are inexpensive materials and very environmentally friendly therefore are very promising for massive industrial applications.

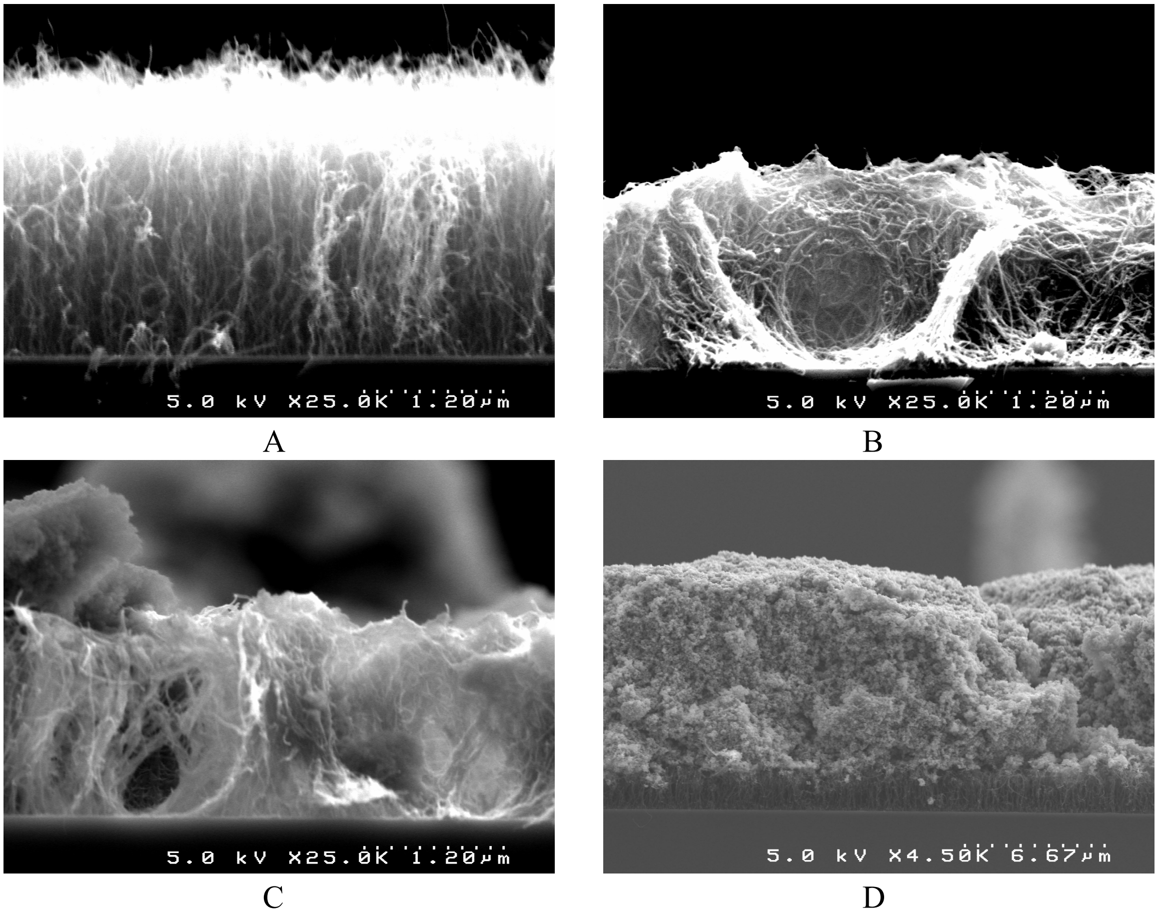

Fig. 4.29. SEM pictures of (A) as grown CNT thin film, (B) 5, (C) 15, and (D) 30 droplets of MnO_2 suspension on CNT film after drying at room temperature.

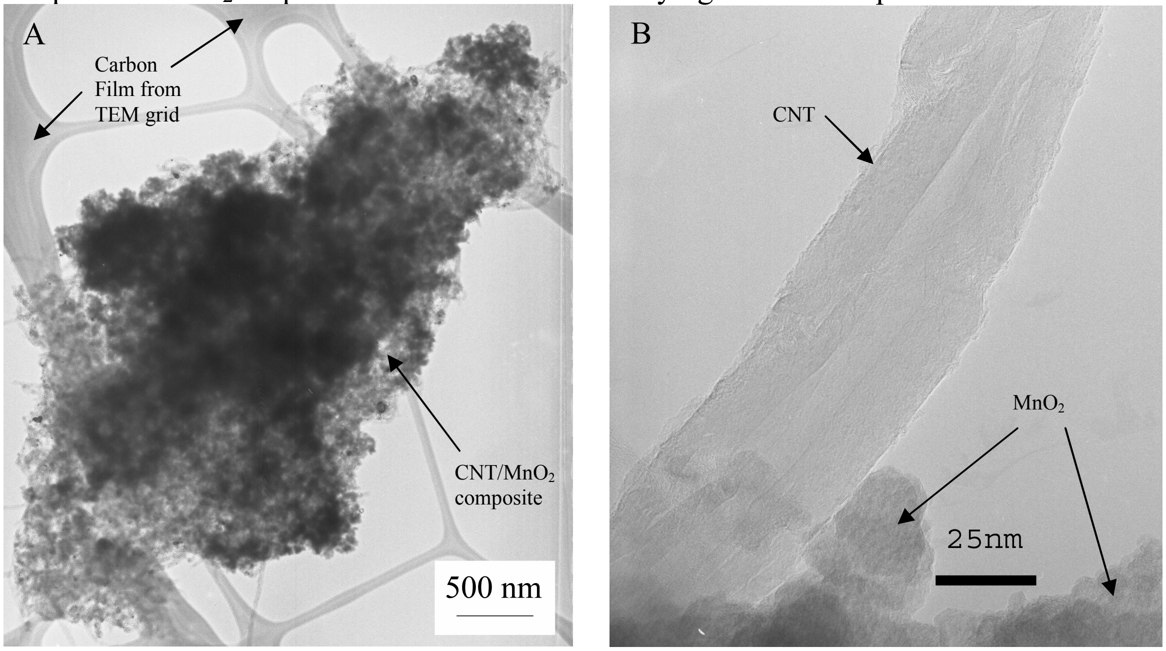

Fig. 4.30. Low (A) and high magnification (B) TEM images showing MnO_2 particles attached to CNTs.

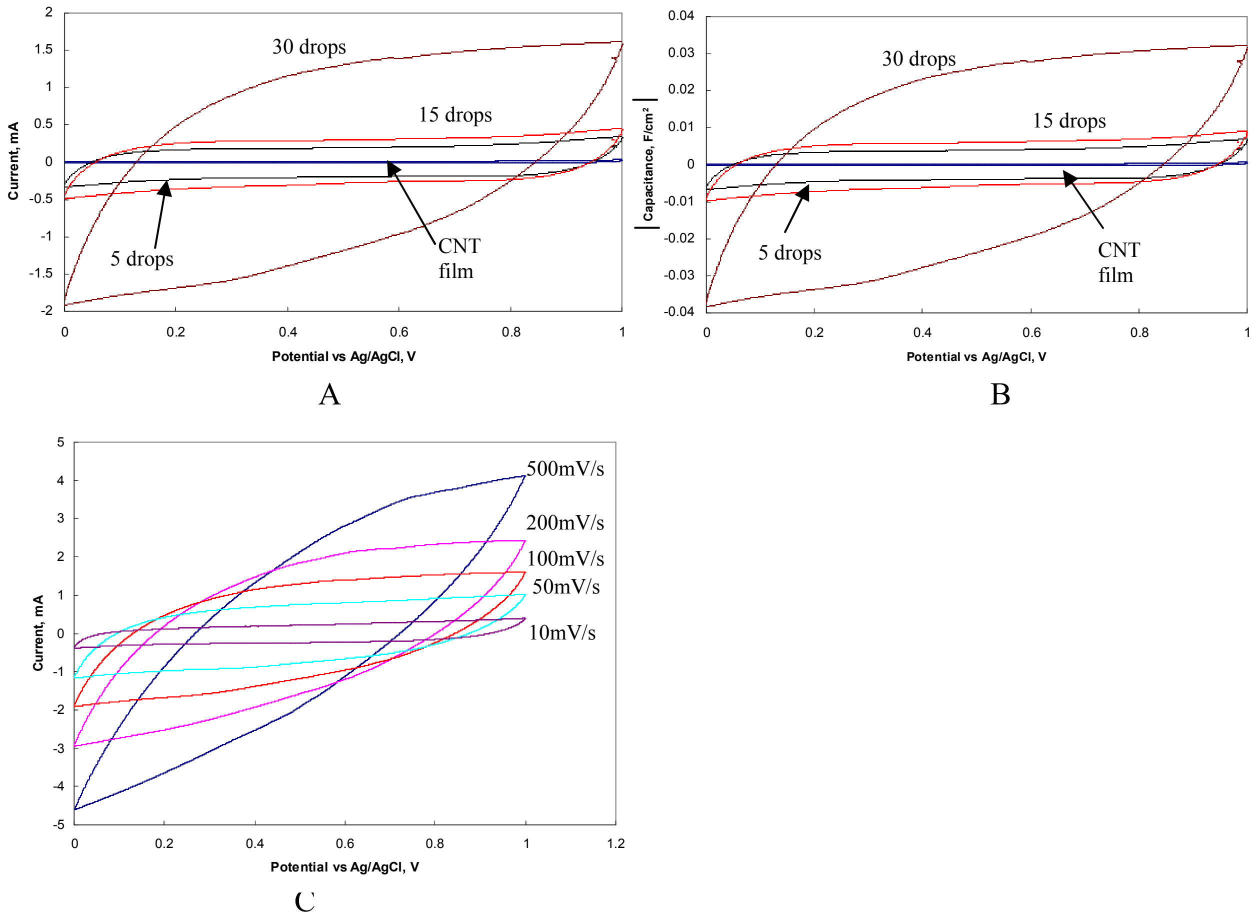

Fig. 4.31. Cyclic voltammograms of MnO_2/CNT composite samples compared with as-grown CNT film at 100mV/s (A); corresponding specific capacitance curves (B); voltammograms of 30-droplet sample at different scan rates (C).

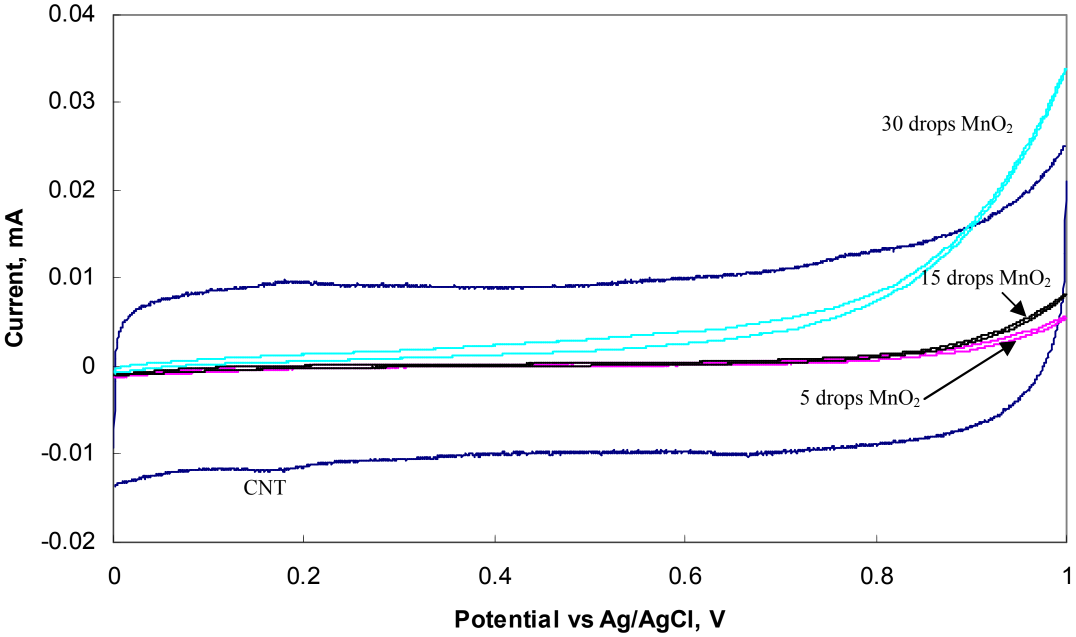

Fig. 4.32. Cyclic voltammograms of CNT-free MnO_2 samples compared with as-grown CNT. Scan rate is 100mV/s.

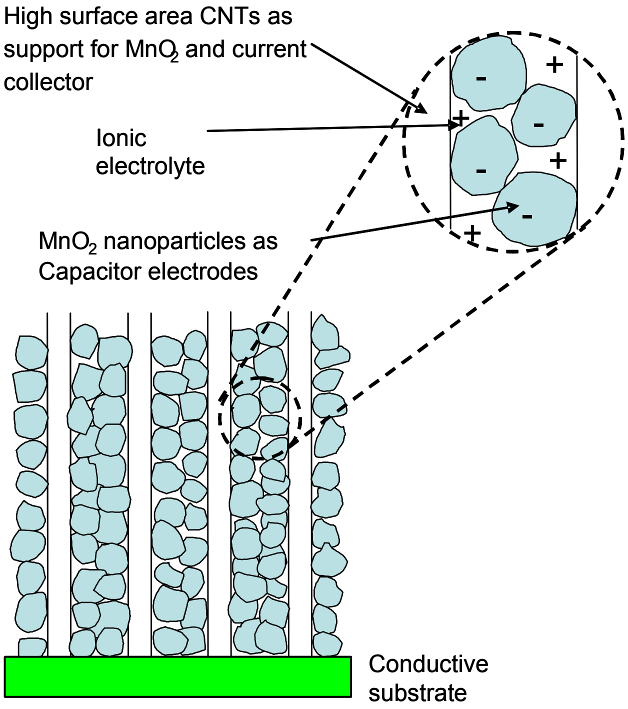

Fig. 4.33. Schematic of supercapacitor based on CNT/MnO2 composite electrode.

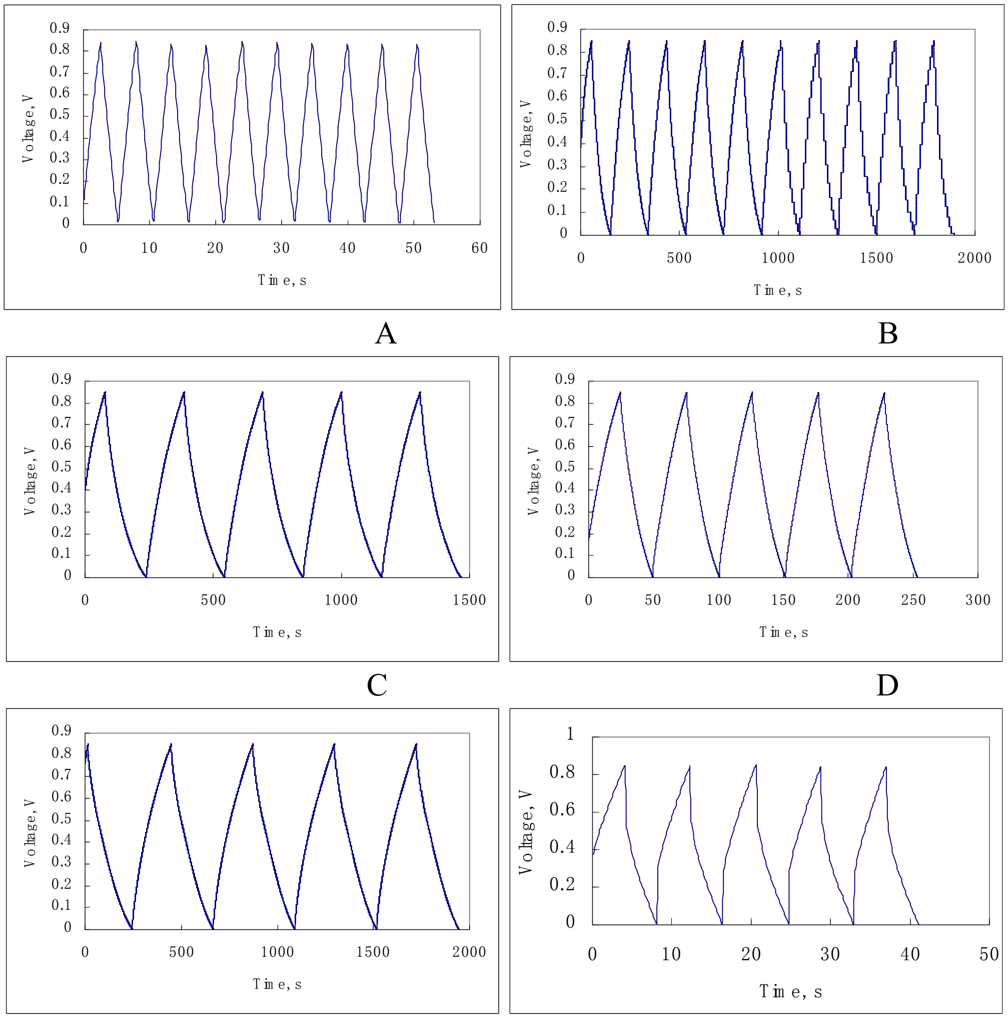

A B

C D

E F

Fig. 4.34. Galvano-static charging and discharging behavior of (A) as-grown CNT film at 30uA, (B) 5-droplet sample at 30uA, (C) 15-droplet sample at 30uA, (D) 15-droplet sample at 120uA, (E) 30-droplet sample at 120uA, and (F) 30-droplet sample at 1920uA, respectively.

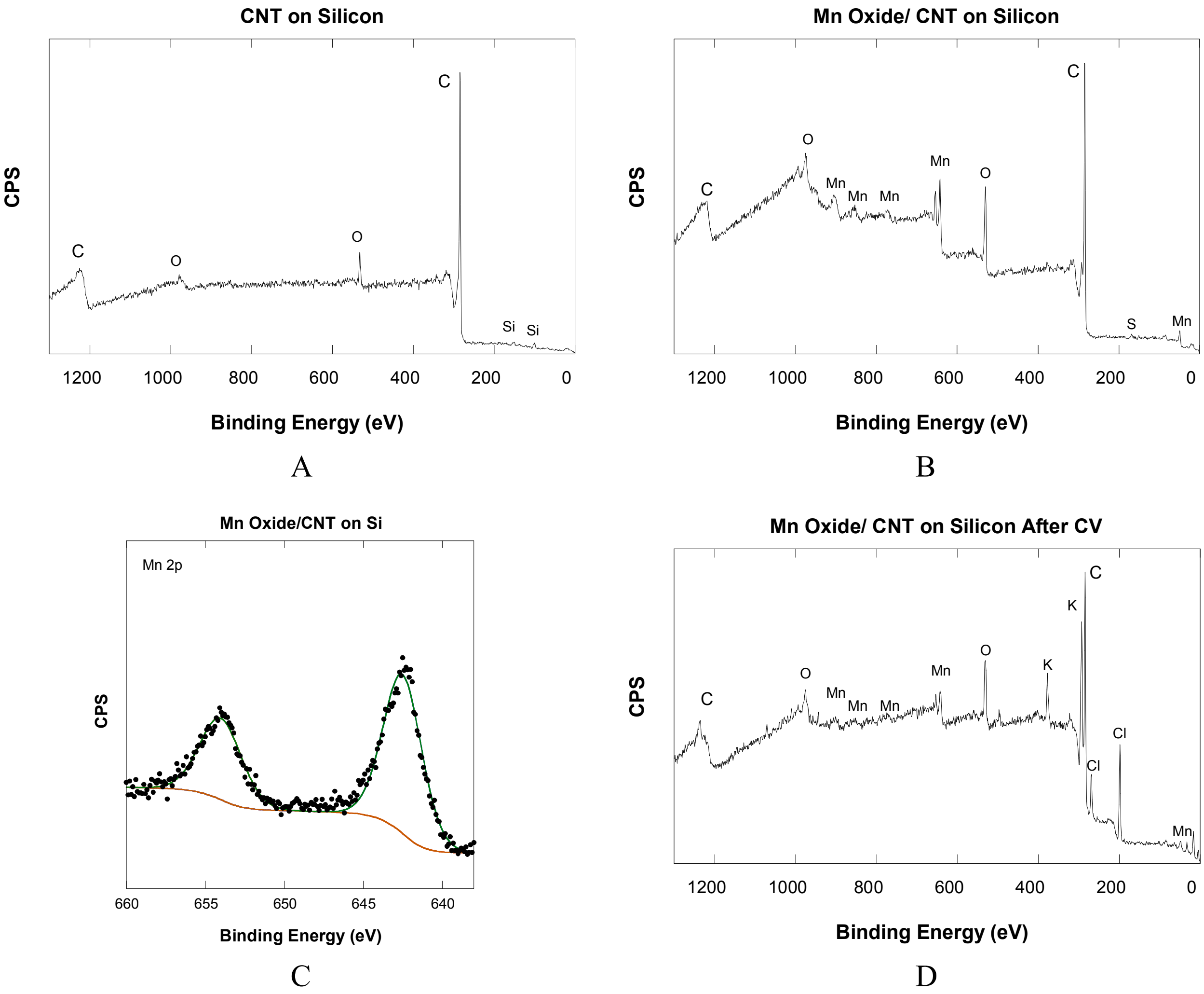

A B

C D

Fig. 4.35. XPS surveys of (A) as-grown CNT thin film, and (B) 5-droplet sample; (C) shows the details of Mn2p peaks corresponding to (B); (D) is the survey of the 5-droplet sample after 100 cyclic voltammetry scans at 100mV/s in 0.1M/L KCl aqueous solution.

Table 4.8. XPS binding energies of manganese oxides at room temperature [143].

	Mn 2p1/2 (±0.2eV)	Mn 2p3/2 (±0.2eV)
MnO	652.2	640.6
Mn_3O_4	653.0	641.4
α-Mn_2O_3	653.5	641.9
β-MnO_2	653.8	642.2
γ-Mn_2O_3	653.4	641.7
γ-MnOOH	653.5	641.7

CHAPTER V

CONCLUSIONS

This chapter summarizes the main findings in CNT synthesis (utilizing thermal CVD and MPECVD), fabrication and characterization of CNT-based field emitters and the novel CNT/MnO_2 capacitor electrodes.

CNT Field Emitters by thermal CVD at atmospheric pressure with Pd as Catalyst:

(1) Pd particle size increases while particle density decreases with thicker catalyst film.

(2) Both hydrogen and ammonia have an annealing effect on Pd particles by rounding off the angles and facets of the particles to make them suitable for CNT synthesis.

(3) Ammonia prohibits amorphous carbon formation and its deposition on Pd catalyst particles thus increases the density of as-grown CNTs.

(4) With synthesis temperature unchanged (~750°C), the Raman spectra of as-grown CNTs are not affected by other process parameters.

(5) CNTs synthesized with ammonia pretreatment demonstrate lower turn-on field and higher field enhancement factor.

(6) Pd is a catalyst as effective as conventional catalysts including Fe, Ni, and Co, for CNT synthesis.

(7) This study was a pioneering work on catalytic properties of Pd for CNT synthesis and has been cited by researchers world-wide for nearly 30 times since 2005.

CNT Field Emitters by thermal CVD at atmospheric pressure with Ni and Co as Catalyst:

(8) Higher flow rate of ammonia reduces amorphous carbon deposition on catalyst particles thus keeps the catalyst sites more active for CNT synthesis.

(9) Catalyst particles of extremely small size are more prone to the poisoning by impurities existing in the gas supply than larger particles. As the result, small particles can be passivated and are unable to produce CNTs.

(10) Ammonia-to-hydrocarbon flow rate ratio is critical as it determines the morphology of as-grown CNTs. CNTs tend to be randomly oriented below the "threshold" ratio and vertically aligned above the ratio.

(11) Vertically aligned CNT arrays demonstrate lower turn-on field and higher field enhancement factor than randomly-oriented CNTs.

(12) The low-cost thermal CVD process at atmospheric pressure is promising for scale-up production of CNT-based field emission devices and other CNT-based electronic devices as well.

CNT-based supercapacitors fabricated by MWPECVD:

(13) Higher density of well-aligned CNT arrays provides larger total accessible surface area therefore yields higher specific capacitance.

(14) Supercapacitor electrodes based on high density vertically aligned CNTs can be easily and cost-effectively fabricated by MPECVD.

(15) This fabrication process does not utilize bulk quantity of CNTs so the cost is significantly reduced.

(16) High capacitance measured from these electrodes, in a lower-concentration and lesser corrosive KCl aqueous electrolyte, with comparable values reported for the

more complicated processes would lead to more stable and longer life-time supercapacitors.

MnO_2 coated CNT electrodes for high performance electrochemical capacitors:

(17) Direct growth of vertically aligned CNTs on conductive Si substrates provides a great platform for attachment of pseudocapacitor material.

(18) A new, efficient, and low-cost process has been developed for fabrication of MnO_2/CNT composite electrode. The resulted structure demonstrates outstanding capacitance behavior with power density more than 400 times of as-grown CNT thin film and excellent long-term chemical stability.

(19) High specific capacitance of 270F/g and high charging-discharging current of 17A/g have been achieved.

(20) Both electrode materials and electrolyte utilized in the newly developed electrochemical capacitor system do not present hazard to environment.

CHAPTER VI

FUTURE WORK

Current studies on CNT field emitters can be advanced in the following directions:

(1) Optimize the height, diameter, and inter-tube spacing of well-aligned CNT arrays for higher field emission current density.

(2) Explore the electron emission behavior and stability of CNT cathodes at high temperatures for potential energy conversion applications.

(3) Test CNT emitters in harsh environment, e.g. under radiation, to examine the possible changes in their field emission behavior and the suitability for aerospace applications.

The following works are recommended to further study supercapacitors:

(4) Grow well-aligned CNT arrays directly on thin, flexible, highly conductive substrates, such as metals and metallic alloys, then incorporate them with manganese dioxide nanoparticles to fabricate highly flexible electrodes.

(5) Construct multi-layer CNT/MnO_2 electrodes for ultra-high capacitance.

(6) Optimize capacitor configurations to further enhance performance.

(7) Optimize the recipes of electrolytes for capacitance enhancement while minimizing their negative impact on the environment.

(8) Explore the combinations of dissimilar electrode materials for negative and positive electrodes.

(9) Further understand the underlying physical and chemical processes at electrode-electrolyte interfaces using molecular simulations.

(10) Utilize the theoretical findings and experimental results to optimize existing devices or design new ones.

PUBLICATIONS

Major findings of this study have been published in peer-reviewed journals and/or presented at refereed conferences.

Peer-Reviewed Journal Publications

S. Wei, W.P. Kang, J.L. Davidson and J.H. Huang, "Supercapacitive behavior of CVD carbon nanotubes grown on Ti coated Si wafer", Diamond and Related Materials 17, 906 (2008).

S. Wei, W. P. Kang, J. L. Davidson et al., "Aligned carbon nanotubes fabricated by thermal CVD at atmospheric pressure using Co as catalyst with NH3 as reactive gas", Diamond and Related Materials 15, 1828 (2006).

S. Wei, W. P. Kang, J. L. Davidson et al., "Vertically aligned carbon nanotube field emission devices fabricated by furnace thermal chemical vapor deposition at atmospheric pressure", Journal of Vacuum Science and Technology B 24, 1190 (2006).

S. Wei, W. P. Kang, W. H. Hofmeister, J. L. Davidson et al., "Effects of deposition and synthesis parameters on size, density, structure, and field emission properties of Pd-catalyzed carbon nanotubes synthesized by thermal chemical vapor deposition", Journal of Vacuum Science and Technology B 23, 793 (2005).

Y. M. Wong, W. P. Kang, J. L. Davidson, W. Hofmeister, S. Wei, and J. H. Huang, "Device characterization of carbon nanotubes field emitters in diode and triode configurations", Diamond and Related Materials 14, 697 (2005).

Y. M. Wong, W. P. Kang, J. L. Davidson, W. Hofmeister, S. Wei, and J. H. Huang, "Transistor characteristics of thermal chemical vapor deposition carbon nanotubes field emission triode", Journal of Vacuum Science and Technology B 23, 868 (2005).

Y. M. Wong, S. Wei, W. P. Kang, J. L. Davidson et al., "Carbon nanotubes field emission devices grown by thermal CVD with palladium as catalysts", Diamond and Related Materials 13, 2105 (2004).

Refereed Conference Presentations/Abstracts

S. Wei, W.P. Kang, J.L. Davidson, B.R. Rogers, and J.H. Huang, "Enhanced supercapacitor behavior of CNT with MnO_2 coating", the 20th European Conference on Diamond, Diamond-Like Materials, Carbon Nanotubes, and Nitrides, Athens, Greece, September 6-10, 2009.

S. Wei, W.P. Kang, J.L. Davidson and B. Rogers, "Supercapacitor Behavior of MnO_2/Aligned CNT Thin Film", the 215th ECS Meeting, San Francisco, CA, May 24-29, 2009.

S. Wei, W.P. Kang, and J.L. Davidson, "MWPECVD Carbon Nanotubes for Supercapacitor Applications", New Diamond and Nano Carbons Conference 2007, Osaka, Japan, May 28-31, 2007.

S. Wei, W.P. Kang, J.L. Davidson, B.K. Choi, and J.H. Huang, "CVD Synthesis of Well Aligned CNTs at Atmospheric Pressure", the joint 11th International Conference on New Diamond Science and Technology (ICNDST) and 9th Applied Diamond Conference (ADC), Research Triangle Park, NC, May 15-18, 2006.

S. Wei, W.P. Kang, J.L. Davidson, W.H. Hofmeister, B.K. Choi, and J.H. Huang, "Vertically aligned carbon nanotubes field emission devices fabricated by furnace thermal CVD at atmospheric pressure", the 18th International Nanoelectronics Conference (IVNC), Oxford, UK, July 10-14, 2005.

Y.M. Wong, W.P. Kang, J.L. Davidson, W. Hofmeister, and S. Wei, "Thermal CVD carbon nanotubes triode", the 15th European Conference on Diamond, Diamond-Like Materials, Carbon Nanotubes, Nitrides & Silicon Carbide, Riva del Garda, Italy, September 12-17, 2004.

Y.M. Wong, W.P. Kang, J.L. Davidson, W. Hofmeister, and S. Wei, "Transistor Characteristics of Thermal CVD Carbon Nanotubes Field Emission Triode", the 17th International Nanoelectronics Conference (IVNC), Cambridge, MA, July 11-16, 2004.

S. Wei, W. P. Kang, W. H. Hofmeister, J.L. Davidson, Y. M. Wong, and J.H. Huang, "The effects of process parameters on size, density, structure, and field emission properties of Pd-catalyzed carbon nanotubes synthesized by thermal chemical vapor deposition", the 17th International Nanoelectronics Conference (IVNC), Cambridge, MA, July 11-16, 2004.

Y.M. Wong, S. Wei, W.P. Kang, J.L. Davidson, W. Hofmeister, J.H. Huang, and Y. Cui, "Carbon Nanotubes Field Emission Devices Grown by Thermal CVD with Palladium as Catalysts", the 9th International Conference on New Diamond Science and Technology (ICNDST), Tokyo, Japan, March 26-29, 2004.

REFERENCES

[1] S. Iijima, Nature 354, 56 (1991).

[2] S. Iijima and T. Ichibashi, Nature 363, 603 (1993).

[3] D. S. Bethune et al., Nature, 363, 605 (1993).

[4] T. W. Odom et al., J. Phys. Chem. B 104, 2794 (2000).

[5] M. Meyyappan, Carbon Nanotubes Science and Applications, CRC Press, 2005.

[6] A. Loiseau et al., Understanding Carbon Nanotubes, Springer, 2006.

[7] T. W. Ebbesen, P. M. Ajayan, Nature 358, 220 (1992).

[8] A. Thess et al., Science 273, 483 (1996).

[9] T. Guo et al., J. Phys. Chem. 99, 10694 (1985).

[10] V. Ivanov et al., Chem. Phys. Lett. 223, 329 (1994).

[11] M. Yudasaka et al., Appl. Phys. Lett. 67, 2477 (1995).

[12] P. E. Nolan, M. J. Schabel, D. C. Lynch, and A. H. Cutler, Carbon 33, 79 (1995).

[13] J. Jiao et al., J. Electrochem. Soc. 143, 932 (1996).

[14] M. Yudasaka et al., Appl. Phys. Lett. 70, 1817 (1997).

[15] P. Chen et al., Carbon 35, 1495 (1997).

[16] H. Dai et al., Chem. Phys. Lett. 260, 471 (1996).

[17] J. H. Hafner et al., Chem. Phys. Lett. 296, 195 (1998).

[18] J. Kong et al., Nature 395, 878 (1998).

[19] A. M. Cassell et al., J. Am. Chem. Soc. 121, 7975 (1999).

[20] A. M. Cassell et al., J. Phys. Chem. B 103, 6484 (1999).

[21] B. Cruden et al., J. Appl. Phys. 94, 4070 (2003).

[22] V. I. Merkulov et al., Appl. Phys. Lett. 76, 3555 (2000).

[23] V. I. Merkulov et al., Appl. Phys. Lett. 79, 1178 (2001).

[24] V. I. Merkulov et al., Appl. Phys. Lett. 79, 2970 (2001).

[25] K. B. K. Teo et al., Appl. Phys. Lett. 79, 1534 (2001).

[26] M. Chhowalla et al., J. Appl. Phys. 90, 5308 (2001).

[27] K. B. K. Teo et al., J. Vac. Sci. Technol. B 20, 116 (2002).

[28] M. Tanemura et al., J. Appl. Phys. 90, 1529 (2001).

[29] J. Han et al., Thin Solid Films 409, 120 (2002).

[30] J. Han et al., J. Appl. Phys. 91, 483 (2002).

[31] Y. Y. Wei et al., Appl. Phys. Lett. 76, 3555 (2001).

[32] L. C. Qin et al., Appl. Phys. Lett. 72, 3437 (1998).

[33] O. Kuttel et al., Appl. Phys. Lett. 73, 2113 (1998).

[34] S. H. Tsai et al., Appl. Phys. Lett. 74, 3462 (1999).

[35] Q. Zhang et al., J. Phys. Chem. Solids 61, 1179 (2000).

[36] Y. C. Choi et al., J. Vac. Sci. Technol. A 18, 1864 (2000).

[37] Y. C. Choi et al., J. Appl. Phys. 88, 4898 (2000).

[38] M. Okai et al., Appl. Phys. Lett. 77, 3468 (2000).

[39] C. Bower et al., Appl. Phys. Lett. 77, 830 (2000).

[40] H. Cui et al., J. Appl. Phys. 88, 6072 (2000).

[41] Y. Chen et al., Chem. Phys. Lett. 272, 178 (1997).

[42] Y. Chen et al., J. Cryst. Growth 193, 342 (1998).

[43] Z. F. Ren et al., Science 282, 1105 (1998).

[44] J. Han et al., J. Appl. Phys. 88, 7363 (2000).

[45] Y. Hayashi et al., J. Vac. Sci. Technol. A 18, 1864 (2000).

[46] Z. P. Huang et al., Appl. Phys. A 74, 387 (2002).

[47] G. W. Ho et al., Thin Solid Films 388, 73 (2001).

[48] H. Ishida et al., Thin Solid Films 407, 26 (2002).

[49] N. Satake et al., Physica B 323, 290 (2002).

[50] Y. H. Wang et al., Appl. Phys. Lett. 79, 680 (2001).

[51] L. Valentini et al., J. Appl. Phys. 92, 6188 (2002).

[52] B. O. Boskovic et al., Nat. Mater. 1, 165 (2002).

[53] C. H. Lin et al., Diamond. Relat. Mater. 11, 922 (2002).

[54] C. M. Hsu et al., Thin Solid Films 420, 225 (2002).

[55] P. L. Chen et al., Diamond. Relat. Mater. 13, 1949 (2004).

[56] Z. Wang et al., Vacuum 77, 139 (2005).

[57] S. K. Patra et al., Appl. Phys. A 80, 1113 (2005).

[58] C. C. Lin et al., Diamond. Relat. Mater. 14, 778 (2005).

[59] W. H. Wang et al., Diamond. Relat. Mater. 14, 753 (2005).

[60] S. H. Lee et al., Diamond. Relat. Mater. 15, 854 (2006).

[61] Z. Wang et al., J. Inorganic. Mater. 21, 1244 (2006).

[62] Z. Wang et al., Vacuum 81, 579 (2007).

[63] M. S. Dresselhaus et al., Carbon Nanotubes Synthesis, Structure, Properties, and Applications, Springer, 2001.

[64] R. Saito et al., Phys. Rev. B 46, 1804 (1992).

[65] N. Hamada et al., Phys. Rev. Lett. 68, 1579 (1992).

[66] J. M. Mintmire et al., Phys. Rev. Lett. 68, 631 (1992).

[67] M. Bockrath et al., Science 275, 1922 (1997).

[68] S. J. Tans et al., Nature 386, 474 (1997).

[69] S. Frank et al., Science 280, 1744 (1998).

[70] J. W. G. Wildoer et al., Nature 391, 59 (1998).

[71] T. W. Odom et al., Nature 391, 62 (1998).

[72] Z. Yao et al., Nature 402, 274 (1999).

[73] P. Delaney et al., Nature 391, 466 (1998).

[74] P. Lambin et al., Comp. Mat. Sci. 2, 350 (1994).

[75] W. Zhu, Vacuum Microelectronics, John Wiley & Sons, 2001.

[76] R. H. Fowler and L. W. Nordheim, Proc. R. Soc. London, 119, 173 (1928).

[77] R. G. Forbes, J. Vac. Sci. Technol. B 17, 526 (1999).

[78] E. Frackowiak, Phys. Chem. Chem. Phys. 9, 1774 (2007).

[79] H. E. Becker, U. S. Patent 2 800 616 (to General Electric) (1957).

[80] D. I. Boos, U. S. Patent 3 536 963 (to Standard Oil, SOHIO) (1970).

[81] R. Kotz et al., Electrochimica Acta 45, 2483 (2000).

[82] B. E. Conway et al., Trans. Faraday Soc. 143, 3791 (1996).

[83] R. Kotz et al., Electrochim. Acta 45, 2483 (2000).

[84] E. Frackowiak et al., Carbon 39, 937 (2001).

[85] R. Ryoo et al., J. Phys. Chem. B 103, 7743 (1999).

[86] T. Kyotani et al., Carbon 41, 1451 (2003).

[87] K. Jurewicz et al., Fuel Process Technol. 77-78, 191 (2002).

[88] G. Lota et al., Chem. Phys. Lett. 404, 53 (2005).

[89] E. Frackowiak et al., Electrochim. Acta 51, 2209 (2005).

[90] J. Dupont et al., Phys. Chem. Chem. Phys. 8, 2441 (2006).

[91] G. Salitra et al., J. Electrochem. Soc. 147, 2486 (2000).

[92] L. Eliad et al., J. Phys. Chem. B 105, 6880 (2001).

[93] A. Laforgue et al., J. Power Sources 80, 142 (1999).

[94] N. L. Wu, Mater. Chem. Phys. 75, 6 (2002).

[95] E. Frackowiak et al., Pol. J. Chem. 78, 1345 (2004).

[96] K. H. An et al., J. Electrochem. Soc., 149, A1058 (2002).

[97] Q. Xiao et al., Electrochim. Acta 48, 575 (2003).

[98] G. Z. Chen et al., Adv. Mater. 12, 522 (2000).

[99] J. P. Zhang et al., J. Electrochem. Soc. 142, 2699 (1995).

[100] L. Delzeit et al., Chem. Phys. Lett. 348, 368 (2001).

[101] H. Kind et al., Langmuir 16, 6877 (2000).

[102] D. Hash et al., J. Appl. Phys. 93, 750 (2003).

[103] N. R. Franklin et al., Adv. Mater. 12, 890 (2002).

[104] S. Hofmann et al., Appl. Phys. Lett. 83, 135 (2003).

[105] D. B. Hash et al., J. Appl. Phys. 90, 2148 (2001).

[106] Z. F. Ren et al., Science 282, 1105 (1998).

[107] S. B. Sinnott et al., Chem. Phys. Lett. 315, 25 (1999).

[108] Y. T. Jang et al., Chem. Phys. Lett. 372, 745 (2003).

[109] C. J. Lee et al., Chem. Phys. Lett. 323, 554 (2000).

[110] C. J. Lee et al., Chem. Phys. Lett. 312, 461 (1999).

[111] K. H. Jung et al., Diamond. Relat. Mater. 13, 299 (2004).

[112] Z. Y. Juang et al., Diamond. Relat. Mater. 13, 1203 (2004).

[113] W. Li et al., Appl. Phys. Lett. 70, 2684 (1997).

[114] Bandow et al., Phys. Rev. Lett. 80, 3779 (1998).

[115] J. M. Bonard et al., Carbon 40, 1715 (2002).

[116] S. G. Wang et al., Diamond. Relat. Mater. 12, 8 (2003).

[117] E. Kowalska et al., Diamond. Relat. Mater. 13, 1008 (2004).

[118] J. M. Bonard et al., Solid-State Electron. 45, 893 (2001).

[119] K. S. Yeong et al., Appl. Surf. Sci. 233, 20 (2004).

[120] F. H. Kaatz et al., Mater. Sci. Eng. C 23, 141 (2003).

[121] K. S. Choi et al., J. Eur. Ceram. Soc. 21, 2095 (2001).

[122] S. Wei et al., J. Vac. Sci. Technol. B 23, 793 (2005).

[123] W. A. de Heer et al., Science 268, 845 (1995).

[124] M. Terrones et al., Nature 388, 52 (1997).

[125] K. H. Jung et al., Diamond. Relat. Mater. 13, 299 (2004).

[126] J. M. Bonard et al., Carbon 40, 1715 (2002).

[127] S. G. Wang et al., Diamond. Relat. Mater. 12, 8 (2003).

[128] K. S. Yeong et al., Appl. Surf. Sci. 233, 20 (2004).

[129] E. Kowalska et al., Diamond. Relat. Mater. 13, 1008 (2004).

[130] J. M. Bonard et al., Solid-State Electron. 45, 893 (2001).

[131] S. B. Sinnott et al., Chem. Phys. Lett. 315, 25 (1999).

[132] S. Wei et al., Diamond. Relat. Mater. 15, 1828 (2006).

[133] S. Wei et al., J. Vac. Sci. Technol. B 24, 1190 (2006).

[134] Y. M. Wong et al., Diamond. Relat. Mater. 13, 2105 (2004).

[135] R. Saito et al., Physical Properties of Carbon Nanotubes, Imperial College Press, 1998.

[136] Hong-Bin Zhang et al., Carbon 40, 2429 (2002).

[137] Rudiger Memmming, Semiconductor Electrochemistry, Wiley-VCH, 2001.

[138] F. Pico et al., J. Electrochem. Soc. 151, A831 (2004).

[139] J. H. Chen et al., Carbon 40, 1193 (2002).

[140] E. Frackowiak, Phys. Chem. Chem. Phys. 9, 1774 (2007).

[141] H. Kim et al., I. Electrochem. Soc. 150, D56 (2003).

[142] V. Subramanian et al., Electrochem. Comm. 8, 827 (2006).

[143] Masaoki Oku et al., J. Electron Spectroscopy Rel. Phen., 7, 465 (1975).